25. ACCELERATOR PHYSICS OF COLLIDERS

Revised August 2003 by K. Desler and D.A. Edwards (DESY).

25.1. Introduction

This article is intended to be a mini-introduction to accelerator physics, with emphasis on colliders. Essential data are summarized in the "Tables of Collider Parameters" (Sec. 26). Luminosity is the quantity of most immediate interest for HEP, and so we begin with its definition and a discussion of the various factors involved. Then we talk about some of the underlying beam dynamics. Finally, we comment on present limitations and possible future directions.

The focus is on colliders because they provide the highest c.m. energy, and therefore, the longest potential discovery reach. All present-day colliders are synchrotrons with the exception of the SLAC Linear Collider. In the pursuit of higher c.m. energy with electrons, synchrotron radiation presents a formidable barrier to energy beyond LEP. The LHC will be the first proton collider in which synchrotron radiation has significant design impact.

25.2. Luminosity

The event rate R in a collider is proportional to the interaction cross section $\sigma_{\rm int}$, and the factor of proportionality is called the *luminosity*:

$$R = \mathscr{L}\sigma_{\rm int} \ . \tag{25.1}$$

If two bunches containing n_1 and n_2 particles collide with frequency f, then the luminosity is approximately

$$\mathscr{L} = f\frac{n_1 n_2}{4\pi\sigma_x\sigma_y}, \tag{25.2}$$

where σ_x and σ_y characterize the Gaussian transverse beam profiles in the horizontal (bend) and vertical directions. Though the initial particle distribution at the source may be far from Gaussian, by the time the beam reaches high energy, the normal form is a very good approximation, thanks to the central limit theorem of probability and diminished importance of space charge effects. The qualifier "approximately" appears because this generic expression requires adaptation to particular cases. Discussion may be found in the article of Furman and Zisman in Sec. 3.1.1 of Ref. 1.

Luminosity is often expressed in units of $\mathrm{cm}^{-2}\mathrm{s}^{-1}$, and tends to be a large number. For example, KEK recently announced that its B factory had reached a peak luminosity in excess of 10^{34} cm^{-2} s^{-1}. The highest luminosity for protons achieved so far is 1.3×10^{32} $\mathrm{cm}^{-2}\mathrm{s}^{-1}$ at the now decommissioned ISR; a goal of the Tevatron run just getting underway as this is written is to challenge that record. The relevant quantity for HEP is the luminosity integrated over time, usually stated in the units normally used for cross sections, such as pb^{-1} or fb^{-1}. B-factory integrated luminosities are moving into the hundreds of fb^{-1} range.

The beam size can be expressed in terms of two quantities, one termed the *transverse emittance*, ϵ, and the other, the *amplitude function*, β. The transverse emittance is a beam quality concept reflecting the process of bunch preparation, extending all the way back to the source for hadrons and, in the case of electrons, mostly dependent on synchrotron radiation. The amplitude function is a beam optics quantity, and is determined by the accelerator magnet configuration.

The transverse emittance is a measure of the phase space area associated with either of the two transverse degrees of freedom, x and y. These coordinates represent the position of a particle with reference to some ideal design trajectory. Think of x as the "horizontal" displacement (in the bend plane for the case of a synchrotron), and y as the "vertical" displacement. The conjugate coordinates are the transverse momenta, which at constant energy are proportional to the angles of particle motion with respect to the design trajectory, x' and y'. Various conventions are in use to characterize the boundary of phase space. Beam sizes are usually given as the standard deviations characterizing Gaussian beam profiles in the two transverse degrees of freedom. In each degree of freedom, the one-σ contour in displacement and angle is frequently used, and we will follow this choice.

Suppose that at some location in the collider, the phase space boundary appears as an upright ellipse, where the coordinates are the displacement x (using the horizontal plane for instance), and the angle x' with respect to the beam axis. The choice of an elliptical contour will be justified under Beam Dynamics below. If σ and σ' are the ellipse semi-axes in the x and x' directions respectively, then the emittance may be defined by $\epsilon \equiv \pi\sigma\sigma'$. Transverse emittance is often stated in units of mm-mrad.

At either a minimum or maximum of the beam size of a beam circulating in equilibrium, the *amplitude function* β at those points is the aspect ratio σ/σ'. When expressed in terms of σ and β, the transverse emittance becomes

$$\epsilon = \pi\sigma^2/\beta \ . \tag{25.3}$$

Of particular significance is the value of the amplitude function at the interaction point, β^*. To achieve high luminosity, one wants β^* to be as small as possible; how small depends on the capability of the hardware to make a near-focus at the interaction point. For example, in the HERA proton ring, β^* at one of the major detectors is 1 m while elsewhere in the synchrotron, typical values of the amplitude function lie in the range 30–100 m. For e^+e^- colliders, $\beta_y^* \sim 1$ cm.

Eq. (25.2) can now be recast in terms of emittances and amplitude functions as

$$\mathscr{L} = f\frac{n_1 n_2}{4\sqrt{\epsilon_x\,\beta_x^*\,\epsilon_y\,\beta_y^*}} \ . \tag{25.4}$$

Thus, to achieve high luminosity, all one has to do is make high population bunches of low emittance collide at high frequency at locations where the beam optics provides as low values of the amplitude functions as possible.

Depending on the particular facility, there are other ways of stating the expression for the luminosity. In a multibunch collider, the various bunch populations will differ; in a facility such as HERA, the electron and proton bunches may differ in emittance, the variation of the beam size in the neighborhood of the interaction point may be significant, and so on.

25.3. Beam dynamics

A major concern of beam dynamics is stability: conservation of adequate beam properties over a sufficiently long time scale. Several time scales are involved, and the approximations used in writing the equations of motion reflect the time scale under consideration. For example, when, in Sec. 25.3.1 below, we write the equations for transverse stability, no terms associated with phase stability or synchrotron radiation appear; the time scale associated with the last two processes is much longer than that demanded by the need for transverse stability.

25.3.1. *Betatron oscillations*:

Present-day high-energy accelerators employ alternating gradient focussing provided by quadrupole magnetic fields [2]. The equations of motion of a particle undergoing oscillations with respect to the design trajectory are

$$x'' + K_x(s)\,x = 0 \ , \quad y'' + K_y(s)\,y = 0 \ , \tag{25.5}$$

with

$$x' \equiv dx/ds \ , \quad y' \equiv dy/ds \tag{25.6}$$

$$K_x \equiv B'/(B\rho) + \rho^{-2} \ , \quad K_y \equiv -B'/(B\rho) \tag{25.7}$$

$$B' \equiv \partial B_y/\partial x \ . \tag{25.8}$$

The independent variable s is path length along the design trajectory. This motion is called a *betatron* oscillation because it was initially studied in the context of that type of accelerator. The functions K_x and K_y reflect the transverse focussing—primarily due to quadrupole fields except for the radius of curvature, ρ, term in K_x for a synchrotron—so each equation of motion resembles that for a harmonic oscillator, but with spring constants that are a function of position. No terms relating to synchrotron oscillations appear,

because their time scale is much longer and, in this approximation, play no role.

These equations have the form of Hill's equation, and so the solution in one plane may be written as

$$x(s) = A\sqrt{\beta(s)}\,\cos(\psi(s)+\delta), \tag{25.9}$$

where A and δ are constants of integration and the phase advances according to $d\psi/ds = 1/\beta$. The dimension of A is the square root of length, reflecting the fact that the oscillation amplitude is modulated by the square root of the amplitude function. In addition to describing the envelope of the oscillation, β also plays the role of an 'instantaneous' λ. The wavelength of a betatron oscillation may be some tens of meters, and so typically values of the amplitude function are of the order of meters, rather than on the order of the beam size. The beam optics arrangement generally has some periodicity, and the amplitude function is chosen to reflect that periodicity. As noted above, a small value of the amplitude function is desired at the interaction point, and so the focussing optics is tailored in its neighborhood to provide a suitable β^*.

The number of betatron oscillations per turn in a synchrotron is called the *tune* and is given by

$$\nu = \frac{1}{2\pi}\oint\frac{ds}{\beta}\ . \tag{25.10}$$

Expressing the integration constant A in the solution above in terms of x, x' yields the *Courant-Snyder invariant*

$$A^2 = \gamma(s)\,x(s)^2 + 2\alpha(s)\,x(s)\,x'(s) + \beta(s)\,x'(s)^2$$

where

$$\alpha \equiv -\beta'/2,\ \ \gamma \equiv \frac{1+\alpha^2}{\beta}\ . \tag{25.11}$$

(The Courant-Snyder parameters α, β, and γ employ three Greek letters which have other meanings, and the significance at hand must often be recognized from context.) Because β is a function of position in the focussing structure, this ellipse changes orientation and aspect ratio from location to location, but the area πA^2 remains the same.

As noted above, the transverse emittance is a measure of the area in x, x' (or y, y') phase space occupied by an ensemble of particles. The definition used in Eq. (25.3) is the area that encloses 39% of a Gaussian beam.

For electron synchrotrons, the equilibrium emittance results from the balance between synchrotron radiation damping and excitation from quantum fluctuations in the radiation rate. The equilibrium is reached in a time which is small compared with the storage time.

For present-day hadron synchrotrons, synchrotron radiation does not play a similar role in determining the transverse emittance. Rather, the emittance during storage reflects the source properties and the abuse suffered by the particles throughout acceleration and storage. Nevertheless, it is useful to argue as follows: Though x' and x can serve as canonically conjugate variables at constant energy, this definition of the emittance would not be an adiabatic invariant when the energy changes during the acceleration cycle. However, $\gamma(v/c)x'$, where here γ is the Lorentz factor, is proportional to the transverse momentum, and so qualifies as a variable conjugate to x. So often one sees a normalized emittance defined according to

$$\epsilon_N = \gamma\,\frac{v}{c}\,\epsilon, \tag{25.12}$$

which is an approximate adiabatic invariant, *e.g.* during acceleration.

25.3.2. ***Phase stability***: The particles in a circular collider also undergo synchrotron oscillations. This is usually referred to as motion in the *longitudinal* degree-of-freedom because particles arrive at a particular position along the accelerator earlier or later than an ideal reference particle. This circumstance results in a finite bunch length, which is related to an energy spread.

For dynamical variables in longitudinal phase space, let us take ΔE and Δt, where these are the energy and time differences from that of the ideal particle. A positive Δt means a particle is behind the ideal particle. The equation of motion is the same as that for a physical pendulum, and therefore is nonlinear. But for small oscillations, it reduces to a simple harmonic oscillator:

$$\frac{d^2\Delta t}{dn^2} = -(2\pi\nu_s)^2\,\Delta t \tag{25.13}$$

where the independent variable n is the turn number, and ν_s is the number of synchrotron oscillations per turn, analogous to the betatron oscillation tune defined earlier. Implicit in this equation is the approximation that n is a continuous variable. This approximation is valid provided $\nu_s \ll 1$, which is usually well satisfied in practice.

In the high-energy limit, where $v/c \approx 1$,

$$\nu_s = \left[\frac{h\eta\,eV\,\cos\phi_s}{2\pi E}\right]^{1/2}\ . \tag{25.14}$$

There are four as yet undefined quantities in this expression: the harmonic number h, the slip factor η, the maximum energy eV gain per turn from the acceleration system, and the synchronous phase ϕ_s. The frequency of the RF system is normally a relatively high multiple, h, of the orbit frequency. The slip factor relates the fractional change in the orbit period τ to changes in energy according to

$$\frac{\Delta\tau}{\tau} = \eta\frac{\Delta E}{E}\ . \tag{25.15}$$

At sufficiently high energy, the slip factor just reflects the relationship between path length and energy, since the speed is a constant; η is positive for all the synchrotrons in the "Tables of Collider Parameters" (Sec. 26).

The synchronous phase is a measure of how far up on the RF wave the average particle must ride in order to maintain constant energy to counteract synchrotron radiation. That is, $\sin\phi_s$ is the ratio of the energy loss per turn to the maximum energy per turn that can be provided by the acceleration system. For hadron colliders built to date, $\sin\phi_s$ is effectively zero. This is not the case for electron storage rings; for example, the electron ring of HERA runs at a synchronous phase of 45°.

Now if one has a synchrotron oscillation with amplitudes $\widehat{\Delta t}$ and $\widehat{\Delta E}$,

$$\Delta t = \widehat{\Delta t}\,\sin(2\pi\nu_s n)\ , \qquad \Delta E = \widehat{\Delta E}\,\cos(2\pi\nu_s n), \tag{25.16}$$

then the amplitudes are related according to

$$\widehat{\Delta E} = \frac{2\pi\nu_s E}{\eta\tau}\widehat{\Delta t}\ . \tag{25.17}$$

The longitudinal emittance ϵ_ℓ may be defined as the phase space area bounded by particles with amplitudes $\widehat{\Delta t}$ and $\widehat{\Delta E}$. In general, the longitudinal emittance for a given amplitude is found by numerical integration. For $\sin\phi_s = 0$, an analytical expression is:

$$\epsilon_\ell = \left[\frac{2\pi^3 EeVh}{\tau^2\eta}\right]^{1/2}(\widehat{\Delta t})^2. \tag{25.18}$$

Again, a Gaussian is a reasonable representation of the longitudinal profile of a well-behaved beam bunch; if $\sigma_{\Delta t}$ is the standard deviation of the time distribution, then the bunch length can be characterized by

$$\ell = c\,\sigma_{\Delta t}\ . \tag{25.19}$$

In the electron case, the longitudinal emittance is determined by the synchrotron radiation process just, as in the transverse degrees of freedom. For the hadron case, the history of acceleration plays a role, and because energy and time are conjugate coordinates, the longitudinal emittance is a quasi-invariant.

For HEP, bunch length is a significant quantity, because if the bunch length becomes larger than β^*, the luminosity is adversely affected. This is because β grows parabolically as one proceeds away from the IP, and so the beam size increases, thus lowering the contribution to the luminosity from such locations.

25.3.3. ***Synchrotron radiation*** [3]: A relativistic particle undergoing centripetal acceleration radiates at a rate given by the Larmor formula multiplied by the 4th power of the Lorentz factor:

$$P = \frac{1}{6\pi\epsilon_0}\frac{e^2a^2}{c^3}\gamma^4. \qquad (25.20)$$

Here, $a = v^2/\rho$ is the centripetal acceleration of a particle with speed v undergoing deflection with radius of curvature ρ. In a synchrotron that has a constant radius of curvature within bending magnets, the energy lost due to synchrotron radiation per turn is the above multiplied by the time spent in bending magnets, $2\pi\rho/v$. Expressed in familiar units, this result may be written

$$W = 8.85 \times 10^{-5} E^4/\rho \ \text{ MeV per turn} \qquad (25.21)$$

for electrons at sufficiently high energy that $v \approx c$. The energy E is in GeV and ρ is in kilometers. The radiation has a broad energy spectrum which falls off rapidly above the *critical energy*, $E_c = (3c/2\rho)\hbar\gamma^3$. Typically, E_c is in the hard x-ray region.

The characteristic time for synchrotron radiation processes is the time during which the energy must be replenished by the acceleration system. If f_0 is the orbit frequency, then the characteristic time is given by

$$\tau_0 = \frac{E}{f_0 W} \ . \qquad (25.22)$$

Oscillations in each of the three degrees of freedom either damp or antidamp depending on the design of the accelerator. For a simple separated-function alternating gradient synchrotron, all three modes damp. The damping time constants are related by Robinson's Theorem [4], which, expressed in terms of τ_0, is

$$\frac{1}{\tau_x} + \frac{1}{\tau_y} + \frac{1}{\tau_s} = 2\frac{1}{\tau_0} \ . \qquad (25.23)$$

Even though all three modes may damp, the emittances do not tend toward zero. Statistical fluctuations in the radiation rate excite synchrotron oscillations and radial betatron oscillations. Thus there is an equilibrium emittance at which the damping and excitation are in balance. The vertical emittance is non-zero due to horizontal-vertical coupling.

Polarization can develop from an initially unpolarized beam as a result of synchrotron radiation. A small fraction $\approx E_c/E$ of the radiated power flips the electron spin. Because the lower energy state is that in which the particle magnetic moment points in the same direction as the magnetic bend field, the transition rate toward this alignment is larger than the rate toward the reverse orientation. An equilibrium polarization of 92% is predicted, and despite a variety of depolarizing processes, polarization above 80% has been observed at a number of facilities.

The radiation rate for protons, is of, course down by a factor of the fourth power of the mass ratio, and is given by

$$W = 7.8 \times 10^{-3} E^4/\rho \ \text{ keV per turn} \qquad (25.24)$$

where E is now in TeV and ρ in km. For the LHC, synchrotron radiation presents a significant load to the cryogenic system, and impacts magnet design due to gas desorption and secondary electron emission from the wall of the cold beam tube. The critical energy for the LHC is 44 eV.

25.3.4. ***Beam-beam tune shift***: In a bunch-bunch collision, the particles of one bunch see the other bunch as a nonlinear lens. Therefore, the focussing properties of the ring are changed in a way that depends on the transverse oscillation amplitude. Hence, there is a spread in the frequency of betatron oscillations.

There is an extensive literature on the subject of how large this tune spread can be. In practice, the limiting value is hard to predict. It is consistently larger for electrons because of the beneficial effects of damping from synchrotron radiation.

In order that contributions to the total tune spread arise only at the detector locations, the beams in a multibunch collider are kept apart elsewhere in the collider by a variety of techniques. For equal energy particles of opposite charge circulating in the same vacuum chamber, electrostatic separators may be used assisted by a crossing angle if appropriate. For particles of equal energy and of the same charge, a crossing angle is needed not only for tune spread reasons, but also to steer the particles into two separate beam pipes. In HERA, because of the large ratio of proton to electron energy, separation can be achieved by bending magnets.

25.3.5. ***Luminosity lifetime***: In electron synchrotrons, the luminosity degrades during the store primarily due to particles leaving the phase stable region in longitudinal phase space, as a result of quantum fluctuations in the radiation rate and bremsstrahlung. For hadron colliders, the luminosity deteriorates due to emittance dilution resulting from a variety of processes. In practice, stores are intentionally terminated when the luminosity drops to the point where a refill will improve the integrated luminosity.

25.4. Status and prospects

Present facilities represent a balance among current technology, the desires of High Energy Physics, and public support. For a half century, beam optics has exploited the invention of alternating gradient focussing. This principle is employed in all colliders both linear and circular. Superconducting technology has grown dramatically in importance during the last two decades. Superconducting magnets are vital to the Tevatron, HERA, and to the future LHC. Superconducting accelerating structures are necessary to CESR, LEP, HERA, Jefferson Laboratory, the spallation neutron source, and other facilities requiring high-gradient long pulse length RF systems. Present room temperature accelerating structures produce very short pulses, but with gradients well in excess of the superconducting variety [1].

At present, the next facilities will include the LHC, and possibly an electron linear collider. The LHC is an approved project that will represent a major step forward in superconducting magnet technology. No linear collider project has been approved as yet, and the conventional and superconducting approaches compete for prominence.

In addition to the possibilities of the preceding paragraph, there are other synchrotron-based collider studies underway. Despite formidable R&D challenges, a muon-muon collider may become feasible. Proponents of a very large hadron collider at higher energy than the cancelled SSC project are exploring low-cost magnets and tunnels for a facility on the 100 TeV c.m. energy scale.

The approach to collider design sketched here—guidance and focussing provided by external magnetic fields, and acceleration produced by RF resonators—has led to ever larger and more costly facilities with increase of c.m. energy. Support for new HEP facilities has diminished as proposals have climbed into the multi-billion dollar range.

There is no shortage of ideas for departure from the current design paradigm. Wakefield accelerators, plasma-laser combinations, and related investigations may, if successful, deliver gradients far higher than any realized today in existing HEP facilities. However, staging and energy efficiency are major hurdles. These approaches are exceedingly challenging technologically, and require a strong R&D program if they are to succeed.

Other important references include Ref. [5–7], which are not cited in the text above.

References:

1. *Handbook of Accelerator Physics and Engineering*, eds. A.W. Chao and M. Tigner, World Scientific Publishing Co. (Singapore, 2nd printing, 2002).
2. E.D. Courant and H.S. Snyder, Ann. Phys. **3**, 1 (1958). This is the classic article on the alternating gradient synchrotron.
3. M. Sands, *The Physics of Electron Storage Rings—An Introduction*, SLAC Publication SLAC 121, UC-28 (ACC), 1970.
4. K. Robinson, Phys. Rev. **111**, 373 (1958).

5. D.A. Edwards and M.J. Syphers, *An Introduction to the Physics of High Energy Accelerators*, John Wiley & Sons, 1993. This is an elementary textbook on accelerator physics. The next two references are more advanced, and are cited here for readers who may wish to pursue beam physics in greater depth.

6. A. Wu Chao, *Physics of Collective Beam Instabilities in High Energy Accelerators*, John Wiley & Sons, 1993.

7. M. Reiser, *Theory and Design of Charged Particle Beams*, John Wiley & Sons, 1994.

HIGH-ENERGY COLLIDER PARAMETERS: e^+e^- Colliders (I)

The numbers here were received from representatives of the colliders in early 2004 (contact C.G. Wohl, LBNL). Many of the numbers of course change with time, and only the latest values (or estimates) are given here; those in brackets are for coming upgrades. Quantities are, where appropriate, r.m.s. H and V indicate horizontal and vertical directions. Parameters for the defunct SPEAR, DORIS, PETRA, PEP, SLC, TRISTAN, and VEPP-2M colliders may be found in our 1996 edition (Phys. Rev. **D54**, 1 July 1996, Part I).

	VEPP-2000 (Novosibirsk)	VEPP-4M (Novosibirsk)	BEPC (China)	BEPC-II (China)	DAΦNE (Frascati)
Physics start date	2005	1994	1989	2007	1999
Physics end date	—	—	—	—	∼2007
Maximum beam energy (GeV)	1.0	6	2.2	1.89 (2.1 max)	0.700
Luminosity (10^{30} cm^{-2}s^{-1})	100	20	10 at 1.843 GeV/beam 5 at 1.55 GeV/beam	1000	80 present 200 achievable
Time between collisions (μs)	0.04	0.6	0.8	0.008	0.0027
Crossing angle (μ rad)	0	0	0	1.1×10^4	$(2.5 \text{ to } 3.2)\times 10^4$
Energy spread (units 10^{-3})	0.64	1	0.58 at 2.2 GeV	0.52	0.40
Bunch length (cm)	4	5	≈ 5	1.3	1 low current 2 high current
Beam radius (10^{-6} m)	125 (round)	H: 1000 V: 30	H: 890 V: 37	H: 380 V: 5.7	H: 800 V: 4.8
Free space at interaction point (m)	±1	±2	±2.15	±1.009	±0.40
Luminosity lifetime (hr)	continuous	2	7–12	1.5	0.7
Filling time (min)	continuous	15	30	26	0.8 (topping up)
Acceleration period (s)	—	150	120	—	on energy
Injection energy (GeV)	0.2–1.0	1.8	1.55	1.89	on energy
Transverse emittance ($10^{-9}\pi$ rad-m)	H: 250 V: 250	H: 200 V: 20	H: 660 V: 28	H: 144 V: 3.1	H: 300 V: 1
β^*, amplitude function at interaction point (m)	H: 0.06 V: 0.06	H: 0.75 V: 0.05	H: 1.2 V: 0.05	H: 1.0 V: 0.015	H: 1.7 V: 0.025
Beam-beam tune shift per crossing (units 10^{-4})	H: 750 V: 750	500	350	400	250
RF frequency (MHz)	172	180	199.53	499.8	356
Particles per bunch (units 10^{10})	16	15	20 at 2 GeV 11 at 1.55 GeV	4.8	
Bunches per ring per species	1	2	1	93	110/120
Average beam current per species (mA)	300	80	40 at 2 GeV 22 at 1.55 GeV	910	1000 (goal 2000)
Circumference or length (km)	0.024	0.366	0.2404	0.23753	0.098
Interaction regions	2	1	2	1	2
Utility insertions	2	1	4	4	2
Magnetic length of dipole (m)	1.2	2	1.6	Outer ring 1.6 Inner ring 1.41	1
Length of standard cell (m)	12	7.2	6.6	Outer ring 6.6 Inner ring 6.2	12
Phase advance per cell (deg)	H: 738 V: 378	65	≈ 60	60–90 no standard cell	360
Dipoles in ring	8	78	40 + 4 weak	84 + 8 weak	8
Quadrupoles in ring	20	150	68	134+2 s.c.	48
Peak magnetic field (T)	2.4	0.6	0.9028 at 2.8 GeV	Outer ring 0.67712 Inner ring 0.76636	1.7

HIGH-ENERGY COLLIDER PARAMETERS: e^+e^- Colliders (II)

The numbers here were received from representatives of the colliders in early 2004. Many of the numbers of course change with time, and only the latest values (or estimates) are given here. Quantities are, where appropriate, r.m.s. H and V indicate horizontal and vertical directions; s.c. indicates superconducting.

	CESR (Cornell)	CESR-C (Cornell)	KEKB (KEK)	PEP-II (SLAC)	LEP (CERN)
Physics start date	1979	2002	1999	1999	1989
Physics end date	2002	—	—	—	2000
Maximum beam energy (GeV)	6	6	$e^- \times e^+$: 8 × 3.5	e^-: 7–12 (9.0 nominal) e^+: 2.5–4 (3.1 ") (nominal E_{cm} = 10.5 GeV)	101 in 1999 (105=max. foreseen
Luminosity (10^{30} cm^{-2}s^{-1})	1280 at 5.3 GeV/beam	35 at 1.9 GeV/beam	11305	6777	24 at Z^0 100 at > 90 GeV
Time between collisions (μs)	0.014 to 0.22	0.014 to 0.22	0.008	0.0042	22
Crossing angle (μ rad)	±2000	±4000	±11,000	0	0
Energy spread (units 10^{-3})	0.6 at 5.3 GeV/beam	0.8 at 1.9 GeV/beam	0.7	e^-/e^+: 0.61/0.77	0.7→1.5
Bunch length (cm)	1.8	1.2	0.65	e^-/e^+: 1.1/1.0	1.0
Beam radius (μm)	H: 460 V: 4	H: 300 V: 5.7	H: 110 V: 2.4	H: 157 V: 4.7	H: 200 → 300 V: 2.5 → 8
Free space at interaction point (m)	±2.2 (±0.6 to REC quads)	±2.2 (±0.3 to PM quads)	+0.75/−0.58 (+300/−500) mrad cone	±0.2, ±300 mrad cone	±3.5
Luminosity lifetime (hr)	2–3	2–3	continuous	3.5	20 at Z^0 10 at > 90 GeV
Filling time (min)	5 (topping up)	5 (topping up)	continuous	3 (topping up)	20 to setup 20 to accumulate
Acceleration period (s)	—	—	—	—	600
Injection energy (GeV)	1.8–6	1.5–6	e^-/e^+: 8/3.5	2.5–12	22
Transverse emittance (π rad-nm)	H: 210 V: 1	H: 150 V: 2.5	e^-: 24 (H), 0.82 (V) e^+: 18 (H), 1.0 (V)	e^-: 48 (H), 1.5 (V) e^+: 24 (H), 1.5 (V)	H: 20–45 V: 0.25 → 1
β^*, amplitude function at interaction point (m)	H: 1.0 V: 0.018	H: 0.60 V: 0.013	e^-: 0.63 (H), 0.0070 (V) e^+: 0.59 (H), 0.0058 (V)	e^-: 0.50 (H), 0.012 (V) e^+: 0.50 (H), 0.012 (V)	H: 1.5 V: 0.05
Beam-beam tune shift per crossing (units 10^{-4})	H: 250 V: 620	H: 175 V: 200	e^-: 710 (H), 510 (V) e^+: 1040 (H), 680 (V)	e^-: 400 (H), 400 (V) e^+: 990 (H), 800 (V)	830
RF frequency (MHz)	500	500	508.887	476	352.2
Particles per bunch (units 10^{10})	1.15	1.15	e^-/e^+: 5.5/7.3	e^-/e^+: 4.6/6.7	45 in collision 60 in single beam
Bunches per ring per species	9 trains of 5 bunches	8 trains of 5 bunches	1281	1230	4 trains of 1 or 2
Average beam current per species (mA)	340	55	e^-/e^+: 1130/1500	e^-/e^+: 1200/1800	4 at Z^0 4→6 at > 90 GeV
Beam polarization (%)	—	—	—	—	55 at 45 GeV 5 at 61 GeV
Circumference or length (km)	0.768	0.768	3.016	2.2	26.66
Interaction regions	1	1	1	1 (2 possible)	4
Utility insertions	3	3	3 per ring	5	4
Magnetic length of dipole (m)	1.6–6.6	1.6–6.6	e^-/e^+: 5.86/0.915	e^-/e^+: 5.4/0.45	11.66/pair
Length of standard cell (m)	16	16	e^-/e^+: 75.7/76.1	15.2	79
Phase advance per cell (deg)	45–90 (no standard cell)	45–90 (no standard cell)	450	e^-/e^+: 60/90	102/90
Dipoles in ring	86	84	e^-/e^+: 116/112	e^-/e^+: 192/192	3280+24 inj. + 64 weak
Quadrupoles in ring	101 + 4 s.c.	101 + 4 s.c.	e^-/e^+: 452/452	e^-/e^+: 290/326	520+288 + 8 s.c.
Peak magnetic field (T)	0.3 normal, 0.8 high field } at 8 GeV	0.3 normal, 0.8 high field } at 8 GeV 2.1 wigglers at 1.9 GeV	e^-/e^+: 0.25/0.72	e^-/e^+: 0.18/0.75	0.135

HIGH-ENERGY COLLIDER PARAMETERS: ep, $\overline{p}p$, and pp Colliders

The numbers here were received from representatives of the colliders in early 2004. Many of the numbers of course change with time, and only the latest values (or estimates) are given here. Quantities are, where appropriate, r.m.s. H, V, and, s.c. indicate horizontal and vertical directions, and superconducting. For existing colliders, the table shows achieved parameters.

	HERA (DESY)	TEVATRON (Fermilab)	RHIC (Brookhaven)			LHC (CERN)	
Physics start date	1992	1987	2000			2007	2008
Physics end date	—	—	—			—	
Particles collided	ep	$p\overline{p}$	pp (pol.)	Au Au	d Au	pp	Pb Pb
Maximum beam energy (TeV)	e: 0.030 p: 0.92	0.980	0.1 40% pol	0.1 TeV/u	0.1 TeV/u	7.0	2.76 TeV/u
Luminosity (10^{30} cm^{-2}s^{-1})	75	50	6	0.0004	0.07	1.0×10^4	0.001
Time between collisions (μs)	0.096	0.396	0.213			0.025	0.100
Crossing angle (μ rad)	0	0	0			300	≤ 100
Energy spread (units 10^{-3})	e: 0.91 p: 0.2	0.14	0.2	0.5	0.5	0.11	0.11
Bunch length (cm)	e: 0.83 p: 8.5	57	40	20	20	7.7	7.94
Beam radius (10^{-6} m)	e: 280(H), 50(V) p: 265(H), 50(V)	p: 39 $\bar{p}$: 31	175 (β^*=1 m)	150 (215 β^*=1 m)	(β^*=2 m)	16.7	15.9
Free space at interaction point (m)	± 2	± 6.5	16			38	38
Luminosity lifetime (hr)	10	11–13	10	3	6	14.9	7.3
Filling time (min)	e: 60 p: 120	30	15			7.5 (both beams)	20 (both beams)
Acceleration period (s)	e: 200 p: 1500	86	140	230	230	1200	
Injection energy (TeV)	e: 0.012 p: 0.040	0.15	0.023	0.011 TeV/u	0.012 TeV/u	0.450	0.1774 TeV/u
Transverse emittance ($10^{-9}\pi$ rad-m)	e: 20(H), 3.5(V) p: 5(H), 5(V)	p: 4.3 $\bar{p}$: 2.7	31	23	23	0.5	0.5
β^*, ampl. function at interaction point (m)	e: 0.6 (H), 0.26(V) p: 2.45(H), 0.18(V)	0.35	1–10	1–5	2–5	0.55	0.5
Beam-beam tune shift per crossing (units 10^{-4})	e: 190(H), 450(V) p: 12(H), 9(V)	p: 14 $\bar{p}$: 70	26	9	11	34	—
RF frequency (MHz)	e: 499.7 p: 208.2/52.05	53	accel: 28 store: 28	accel: 28 store: 197	accel: 28 store: 197	400.8	400.8
Particles per bunch (units 10^{10})	e: 3 p: 7	p: 24 $\bar{p}$: 3	7	0.06	d: 1.1 Au: 0.07	11.5	0.007
Bunches per ring per species	e: 189 p: 180	36	55			2808	592
Average beam current per species (mA)	e: 40 p: 90	p: 66 $\bar{p}$: 8.2	48	33	d: 7.7 Au: 38	584	6.12
Circumference (km)	6.336	6.28	3.834			26.659	
Interaction regions	2 collining beam 1 fixed target (e beam)	2 high $\mathscr{L}$	6			2 high $\mathscr{L}$ +1	1
Utility insertions	4	4	13/ring			4	
Magnetic length of dipole (m)	e: 9.185 p: 8.82	6.12	9.45			14.3	
Length of standard cell (m)	e: 23.5 p: 47	59.5	29.7			106.90	
Phase advance per cell (deg)	e: 60 p: 90	67.8	84			90	
Dipoles in ring	e: 396 p: 416	774	192 per ring + 12 common			1232 main dipoles	
Quadrupoles in ring	e: 580 p: 280	216	246 per ring			482 2-in-1 24 1-in-1	
Magnet type	e: C-shaped p: s.c., collared, cold iron	s.c. cosθ warm iron	s.c. cosθ cold iron			s.c. 2 in 1 cold iron	
Peak magnetic field (T)	e: 0.274 p: 5	4.4	3.5			8.3	
$\overline{p}$ source accum. rate (hr^{-1})	—	13.5×10^{10}	—			—	
Max. no. $\overline{p}$ in accum. ring	—	2.4×10^{12}	—			—	

27. PASSAGE OF PARTICLES THROUGH MATTER

Revised April 2002 by H. Bichsel (University of Washington), D.E. Groom (LBNL), and S.R. Klein (LBNL).

27.1. Notation

Table 27.1: Summary of variables used in this section. The kinematic variables β and γ have their usual meanings.

Symbol	Definition	Units or Value
α	Fine structure constant $(e^2/4\pi\epsilon_0\hbar c)$	1/137.035 999 11(46)
M	Incident particle mass	MeV/c^2
E	Incident particle energy γMc^2	MeV
T	Kinetic energy	MeV
$m_e c^2$	Electron mass $\times\ c^2$	0.510 998 918(44) MeV
r_e	Classical electron radius $e^2/4\pi\epsilon_0 m_e c^2$	2.817 940 325(28) fm
N_A	Avogadro's number	$6.022\,1415(10)\times10^{23}$ mol^{-1}
ze	Charge of incident particle	
Z	Atomic number of absorber	
A	Atomic mass of absorber	g mol^{-1}
K/A	$4\pi N_A r_e^2 m_e c^2/A$	0.307 075 MeV g^{-1} cm^2 for A = 1 g mol^{-1}
I	Mean excitation energy	eV (*Nota bene!*)
δ	Density effect correction to ionization energy loss	
$\hbar\omega_p$	Plasma energy $(\sqrt{4\pi N_e r_e^3}\ m_e c^2/\alpha)$	$28.816\sqrt{\rho\langle Z/A\rangle}$ eV[a]
N_c	Electron density	(units of r_e)$^{-3}$
w_j	Weight fraction of the jth element in a compound or mixture	
n_j	$\propto$ number of jth kind of atoms in a compound or mixture	
—	$4\alpha r_e^2 N_A/A$	(716.408 g cm^{-2})$^{-1}$ for $A = 1$ g mol^{-1}
X_0	Radiation length	g cm^{-2}
E_c	Critical energy for electrons	MeV
$E_{\mu c}$	Critical energy for muons	GeV
E_s	Scale energy $\sqrt{4\pi/\alpha}\ m_e c^2$	21.2052 MeV
R_M	Molière radius	g cm^{-2}

[a] For ρ in g cm^{-3}.

27.2. Electronic energy loss by heavy particles [1–5]

Moderately relativistic charged particles other than electrons lose energy in matter primarily by ionization and atomic excitation. The mean rate of energy loss (or stopping power) is given by the Bethe-Bloch equation,

$$-\frac{dE}{dx} = Kz^2\frac{Z}{A}\frac{1}{\beta^2}\left[\frac{1}{2}\ln\frac{2m_e c^2\beta^2\gamma^2 T_{\max}}{I^2} - \beta^2 - \frac{\delta}{2}\right] . \qquad (27.1)$$

Here $T_{\max}$ is the maximum kinetic energy which can be imparted to a free electron in a single collision, and the other variables are defined in Table 27.1. With K as defined in Table 27.1 and A in g mol^{-1}, the units are MeV g^{-1}cm^2.

In this form, the Bethe-Bloch equation describes the energy loss of pions in a material such as copper to about 1% accuracy for energies between about 6 MeV and 6 GeV (momenta between about 40 MeV/c and 6 GeV/c). At lower energies various corrections discussed in Sec. 27.2.1 must be made. At higher energies, radiative effects begin to be important. These limits of validity depend on both the effective atomic number of the absorber and the mass of the slowing particle.

The function as computed for muons on copper is shown by the solid curve in Fig. 27.1, and for pions on other materials in Fig. 27.3. A minor dependence on M at the highest energies is introduced through $T_{\max}$, but for all practical purposes in high-energy physics dE/dx in a given material is a function only of β. Except in hydrogen, particles of the same velocity have similar rates of energy loss in different materials; there is a slow decrease in the rate of energy loss with increasing Z. The qualitative difference in stopping power behavior at high energies between a gas (He) and the other materials shown in Fig. 27.3 is due to the density-effect correction, δ, discussed below. The stopping power functions are characterized by broad minima whose position drops from $\beta\gamma = 3.5$ to 3.0 as Z goes from 7 to 100. The values of minimum ionization as a function of atomic number are shown in Fig. 27.2.

In practical cases, most relativistic particles (*e.g.*, cosmic-ray muons) have mean energy loss rates close to the minimum, and are said to be minimum ionizing particles, or mip's.

As discussed below, the most probable energy loss in a detector is considerably below the mean given by the Bethe-Bloch equation.

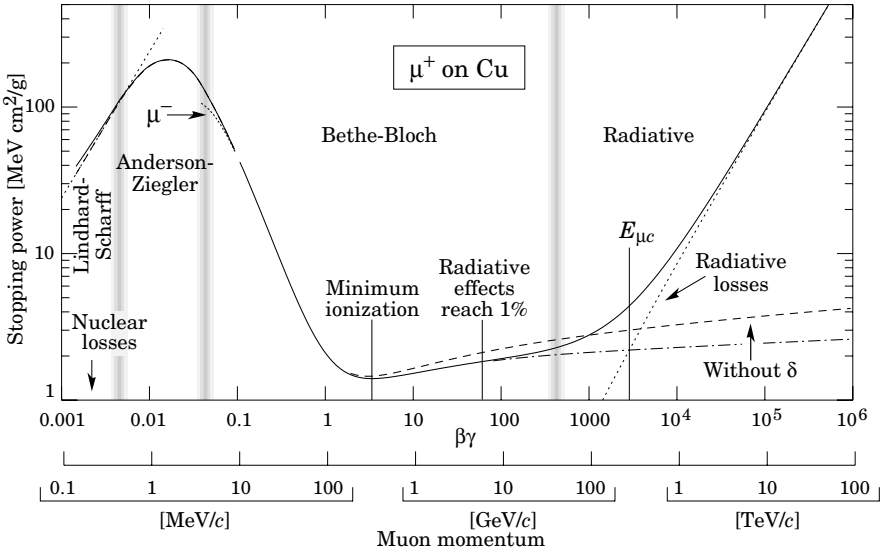

Fig. 27.1: Stopping power ($= \langle -dE/dx\rangle$) for positive muons in copper as a function of $\beta\gamma = p/Mc$ over nine orders of magnitude in momentum (12 orders of magnitude in kinetic energy). Solid curves indicate the total stopping power. Data below the break at $\beta\gamma \approx 0.1$ are taken from ICRU 49 [2], and data at higher energies are from Ref. 1. Vertical bands indicate boundaries between different approximations discussed in the text. The short dotted lines labeled "μ^-" illustrate the "Barkas effect," the dependence of stopping power on projectile charge at very low energies [6].

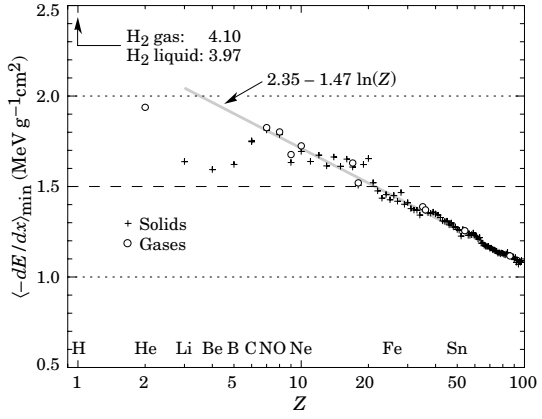

Figure 27.2: Stopping power at minimum ionization for the chemical elements. The straight line is fitted for $Z > 6$. A simple functional dependence on Z is not to be expected, since $\langle -dE/dx \rangle$ also depends on other variables.

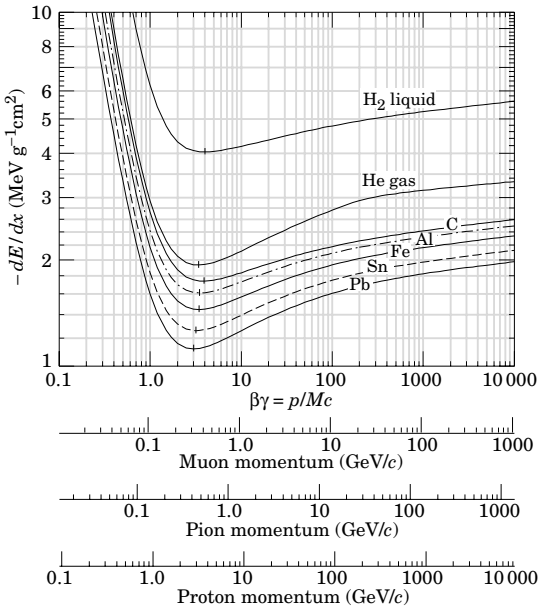

Figure 27.3: Mean energy loss rate in liquid (bubble chamber) hydrogen, gaseous helium, carbon, aluminum, iron, tin, and lead. Radiative effects, relevant for muons and pions, are not included. These become significant for muons in iron for $\beta\gamma \gtrsim 1000$, and at lower momenta for muons in higher-Z absorbers. See Fig. 27.20.

Eq. (27.1) may be integrated to find the total (or partial) "continuous slowing-down approximation" (CSDA) range R for a particle which loses energy only through ionization and atomic excitation. Since dE/dx depends only on β, R/M is a function of E/M or pc/M. In practice, range is a useful concept only for low-energy hadrons ($R \lesssim \lambda_I$, where λ_I is the nuclear interaction length), and for muons below a few hundred GeV (above which radiative effects dominate). R/M as a function of $\beta\gamma = p/Mc$ is shown for a variety of materials in Fig. 27.4.

The mass scaling of dE/dx and range is valid for the electronic losses described by the Bethe-Bloch equation, but not for radiative losses, relevant only for muons and pions.

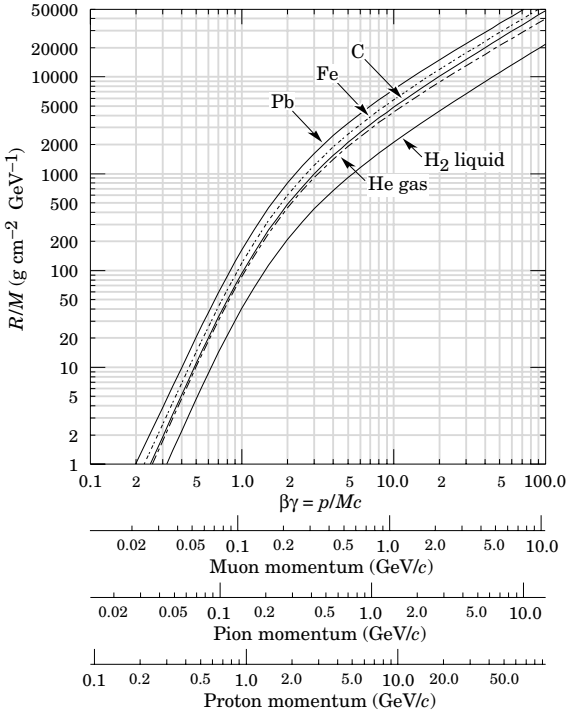

Figure 27.4: Range of heavy charged particles in liquid (bubble chamber) hydrogen, helium gas, carbon, iron, and lead. For example: For a K^+ whose momentum is 700 MeV/c, $\beta\gamma = 1.42$. For lead we read $R/M \approx 396$, and so the range is 195 g cm^{-2}.

For a particle with mass M and momentum $M\beta\gamma c$, $T_{\rm max}$ is given by

$$T_{\rm max} = \frac{2m_e c^2\,\beta^2\gamma^2}{1 + 2\gamma m_e/M + (m_e/M)^2}\ . \qquad (27.2)$$

In older references [3,4] the "low-energy" approximation $T_{\rm max} = 2m_e c^2\,\beta^2\gamma^2$, valid for $2\gamma m_e/M \ll 1$, is often implicit. For a pion in copper, the error thus introduced into dE/dx is greater than 6% at 100 GeV. The correct expression should be used.

At energies of order 100 GeV, the maximum 4-momentum transfer to the electron can exceed 1 GeV/c, where hadronic structure effects significantly modify the cross sections. This problem has been investigated by J.D. Jackson [7], who concluded that for hadrons (but not for large nuclei) corrections to dE/dx are negligible below energies where radiative effects dominate. While the cross section for rare hard collisions is modified, the average stopping power, dominated by many softer collisions, is almost unchanged.

"The determination of the mean excitation energy is the principal non-trivial task in the evaluation of the Bethe stopping-power formula" [8]. Recommended values have varied substantially with time. Estimates based on experimental stopping-power measurements for protons, deuterons, and alpha particles and on oscillator-strength distributions and dielectric-response functions were given in ICRU 37 [9]. These values, shown in Fig. 27.5, have since been widely used. Machine-readable versions can also be found [10]. These values are widely used.

27.2.1. ***Energy loss at low energies***: Shell corrections C/Z must be included in the square brackets of of Eq. (27.1) [2,9,11,12] to correct for atomic binding having been neglected in calculating some of the contributions to Eq. (27.1). The Barkas form [12] was used in generating Fig. 27.1. For copper it contributes about 1% at $\beta\gamma = 0.3$ (kinetic energy 6 MeV for a pion), and the correction decreases very rapidly with energy.

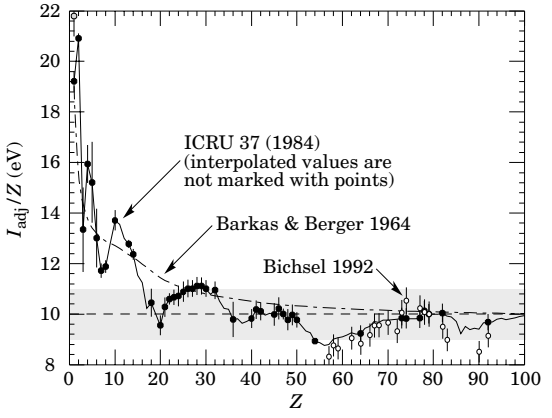

Figure 27.5: Mean excitation energies (divided by Z) as adopted by the ICRU [9]. Those based on experimental measurements are shown by symbols with error flags; the interpolated values are simply joined. The grey point is for liquid H_2; the black point at 19.2 eV is for H_2 gas. The open circles show more recent determinations by Bichsel [11]. The dotted curve is from the approximate formula of Barkas [12] used in early editions of this *Review*.

Eq. (27.1) is based on a first-order Born approximation. Higher-order corrections, again important only at lower energy, are normally included by adding a term $z^2 L_2(\beta)$ inside the square brackets.

An additional "Barkas correction" $zL_1(\beta)$ makes the stopping power for a negative particle somewhat larger than for a positive particle with the same mass and velocity. In a 1956 paper, Barkas *et al.* noted that negative pions had a longer range than positive pions [6]. The effect has been measured for a number of negative/positive particle pairs, most recently for antiprotons at the CERN LEAR facility [13].

A detailed discussion of low-energy corrections to the Bethe formula is given in ICRU Report 49 [2]. When the corrections are properly included, the accuracy of the Bethe-Bloch treatment is accurate to about 1% down to $\beta \approx 0.05$, or about 1 MeV for protons.

For $0.01 < \beta < 0.05$, there is no satisfactory theory. For protons, one usually relies on the phenomenological fitting formulae developed by Andersen and Ziegler [2,14]. For particles moving more slowly than $\approx 0.01c$ (more or less the velocity of the outer atomic electrons), Lindhard has been quite successful in describing electronic stopping power, which is proportional to β [15,16]. Finally, we note that at low energies, *e.g.*, for protons of less than several hundred eV, non-ionizing nuclear recoil energy loss dominates the total energy loss [2,16,17].

As shown in ICRU49 [2] (using data taken from Ref. 14), the nuclear plus electronic proton stopping power in copper is 113 MeV cm^2 g^{-1} at $T = 10$ keV, rises to a maximum of 210 MeV cm^2 g^{-1} at 100–150 keV, then falls to 120 MeV cm^2 g^{-1} at 1 MeV. Above 0.5–1.0 MeV the corrected Bethe-Bloch theory is adequate.

27.2.2. ***Density effect***: As the particle energy increases, its electric field flattens and extends, so that the distant-collision contribution to Eq. (27.1) increases as $\ln\beta\gamma$. However, real media become polarized, limiting the field extension and effectively truncating this part of the logarithmic rise [3–4,18–21]. At very high energies,

$$\delta/2 \to \ln(\hbar\omega_p/I) + \ln\beta\gamma - 1/2 \ , \tag{27.3}$$

where $\delta/2$ is the density effect correction introduced in Eq. (27.1) and $\hbar\omega_p$ is the plasma energy defined in Table 27.1. A comparison with Eq. (27.1) shows that $|dE/dx|$ then grows as $\ln\beta\gamma$ rather than $\ln\beta^2\gamma^2$, and that the mean excitation energy I is replaced by the plasma energy $\hbar\omega_p$. The ionization stopping power as calculated with and without the density effect correction is shown in Fig. 27.1. Since the plasma frequency scales as the square root of the electron density, the correction is much larger for a liquid or solid than for a gas, as is illustrated by the examples in Fig. 27.3.

The density effect correction is usually computed using Sternheimer's parameterization [18]:

$$\delta = \begin{cases} 2(\ln 10)x - \overline{C} & \text{if } x \geq x_1; \\ 2(\ln 10)x - \overline{C} + a(x_1 - x)^k & \text{if } x_0 \leq x < x_1; \\ 0 & \text{if } x < x_0 \text{ (nonconductors);} \\ \delta_0 10^{2(x-x_0)} & \text{if } x < x_0 \text{ (conductors)} \end{cases} \tag{27.4}$$

Here $x = \log_{10}\eta = \log_{10}(p/Mc)$. $\overline{C}$ (the negative of the C used in Ref. 18) is obtained by equating the high-energy case of Eq. (27.4) with the limit given in Eq. (27.3). The other parameters are adjusted to give a best fit to the results of detailed calculations for momenta below $Mc\exp(x_1)$. Parameters for elements and nearly 200 compounds and mixtures of interest are published in a variety of places, notably in Ref. 21. A recipe for finding the coefficients for nontabulated materials is given by Sternheimer and Peierls [19], and is summarized in Ref. 1.

The remaining relativistic rise comes from the $\beta^2\gamma^2$ growth of T_{max}, which in turn is due to (rare) large energy transfers to a few electrons. When these events are excluded, the energy deposit in an absorbing layer approaches a constant value, the Fermi plateau (see Sec. 27.2.4 below). At extreme energies (*e.g.*, > 332 GeV for muons in iron, and at a considerably higher energy for protons in iron), radiative effects are more important than ionization losses. These are especially relevant for high-energy muons, as discussed in Sec. 27.6.

27.2.3. ***Energetic knock-on electrons (δ rays)***: The distribution of secondary electrons with kinetic energies $T \gg I$ is given by [3]

$$\frac{d^2N}{dTdx} = \frac{1}{2}\,Kz^2\frac{Z}{A}\frac{1}{\beta^2}\frac{F(T)}{T^2} \tag{27.5}$$

for $I \ll T \leq T_{max}$, where T_{max} is given by Eq. (27.2). Here β is the velocity of the primary particle. The factor F is spin-dependent, but is about unity for $T \ll T_{max}$. For spin-0 particles $F(T) = (1 - \beta^2 T/T_{max})$; forms for spins 1/2 and 1 are also given by Rossi [3]. For incident electrons, the indistinguishability of projectile and target means that the range of T extends only to half the kinetic energy of the incident particle. Additional formulae are given in Ref. 22. Equation (27.5) is inaccurate for T close to I: for $2I \lesssim T \lesssim 10I$, the $1/T^2$ dependence above becomes approximately $T^{-\eta}$, with $3 \lesssim \eta \lesssim 5$ [23].

δ rays of appreciable energy are rare. For example, for a 500 MeV pion incident on a silicon detector with thickness $x = 300$ μm, one may integrate Eq. (27.5) from T_{cut} to T_{max} to find that $x(dN/dx) = 1$, or an average of one δ ray per particle crossing, for T_{cut} equal to only 12 keV. For $T_{cut} = 116$ keV (the mean minimum energy loss in 300 μm of silicon), $x(dN/dx) = 0.0475$—less than one particle in 20 produces a δ ray with kinetic energy greater than T_{cut}.*

A δ ray with kinetic energy T_e and corresponding momentum p_e is produced at an angle θ given by

$$\cos\theta = (T_e/p_e)(p_{max}/T_{max}) \ , \tag{27.6}$$

where p_{max} is the momentum of an electron with the maximum possible energy transfer T_{max}.

27.2.4. ***Restricted energy loss rates for relativistic ionizing particles***: Further insight can be obtained by examining the mean energy deposit by an ionizing particle when energy transfers are restricted to $T \leq T_{cut} \leq T_{max}$. The restricted energy loss rate is

$$-\left.\frac{dE}{dx}\right|_{T<T_{cut}} = Kz^2\frac{Z}{A}\frac{1}{\beta^2}\left[\frac{1}{2}\ln\frac{2m_ec^2\beta^2\gamma^2T_{cut}}{I^2} - \frac{\beta^2}{2}\left(1 + \frac{T_{cut}}{T_{max}}\right) - \frac{\delta}{2}\right] . \tag{27.7}$$

This form approaches the normal Bethe-Bloch function (Eq. (27.1)) as $T_{cut} \to T_{max}$. It can be verified that the difference between Eq. (27.1) and Eq. (27.7) is equal to $\int_{T_{cut}}^{T_{max}} T(d^2N/dTdx)dT$, where $d^2N/dTdx$ is given by Eq. (27.5).

* These calculations assume a spin-0 incident particle and the validity of the Rutherford cross section used in Eq. (27.5).

Since $T_{\rm cut}$ replaces $T_{\rm max}$ in the argument of the logarithmic term of Eq. (27.1), the $\beta\gamma$ term producing the relativistic rise in the close-collision part of dE/dx is replaced by a constant, and $|dE/dx|_{T<T_{\rm cut}}$ approaches the constant "Fermi plateau." (The density effect correction δ eliminates the explicit $\beta\gamma$ dependence produced by the distant-collision contribution.)

27.2.5. ***Fluctuations in energy loss***: The mean energy loss per unit absorber thickness by charged particles in matter, as given by the Bethe-Bloch formula (Eq. (27.1)), is essentially useless in describing the behavior of a single particle because of the stochastic nature of the energy losses. Since the single-collision spectrum is highly skewed, the probability distribution function (pdf) describing the "straggling" is also highly skewed. The pdf $f(\Delta;\beta\gamma,x)$ describing the distribution of energy loss Δ in absorber thickness x is usually called the "Landau distribution [24]," although a careful reading of Rossi [3] shows that the matter is much more complicated. Examples of the distribution based on recent calculations by Bichsel [25–27] are shown in Fig. 27.6. The most probable loss Δ_p increases in a first approximation as $x\,(a+\ln x)$, and the ratio w/Δ_p decreases with increasing x (where w is the full width at half maximum, as indicated in the figure). For very thick absorbers, where the energy loss exceeds one half of the original energy, $f(\Delta)$ begins to approximate a Gaussian.

The most probable loss per unit thickness, normalized to the mean loss rate by a minimum ionizing particle, is shown in Fig. 27.7. These "Bichsel functions" rise by perhaps 10% from their minimum values as the energy increases, but reach a Fermi plateau for the same reasons that restricted energy loss does: The asymptotic $\ln\beta\gamma$ rise in the Bethe-Block formula comes from the hard-collision losses that create the tail.

The most probable loss is much more relevant to detector calibration than the mean energy loss, since the tail is often lost in background and in any case is difficult to define because of the weight of a few high-loss events. Note that the most probable loss is less than 70% of the mean for a typical silicon strip detector.

The function $f(\Delta;\beta\gamma,x)$ should be used in maximum likelihood fits to the signals produced by a single particle, as in the case of a track in a TPC.

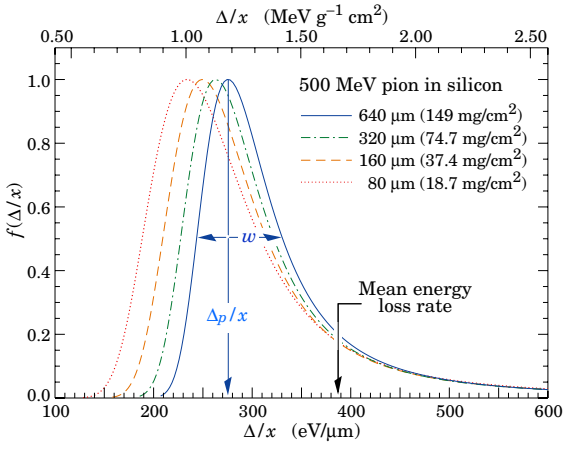

Figure 27.6: Straggling functions in silicon for 500 MeV pions, normalized to unity at the most probable value Δ_p/x. The width w is the full width at half maximum.

27.2.6. ***Energy loss in mixtures and compounds***: A mixture or compound can be thought of as made up of thin layers of pure elements in the right proportion (Bragg additivity). In this case,

$$\frac{dE}{dx} = \sum w_j \left.\frac{dE}{dx}\right|_j , \qquad (27.8)$$

where $dE/dx|_j$ is the mean rate of energy loss (in MeV g cm^{-2}) in the jth element. Eq. (27.1) can be inserted into Eq. (27.8) to find expressions for $\langle Z/A\rangle$, $\langle I\rangle$, and $\langle\delta\rangle$; for example, $\langle Z/A\rangle = \sum w_j Z_j/A_j = \sum n_j Z_j / \sum n_j A_j$. However, $\langle I\rangle$ as defined this way is an underestimate, because in a compound electrons are more tightly bound than in the free elements, and $\langle\delta\rangle$ as calculated this way has little relevance, because it is the electron density which matters. If possible, one uses the tables given in Refs. 21 and 28, which include effective excitation energies and interpolation coefficients for calculating the density effect correction for the chemical elements and nearly 200 mixtures and compounds. If a compound or mixture is not found, then one uses the recipe for δ given in Ref. 19 (repeated in Ref. 1), and calculates $\langle I\rangle$ according to the discussion in Ref. 8. (Note the "13%" rule!)

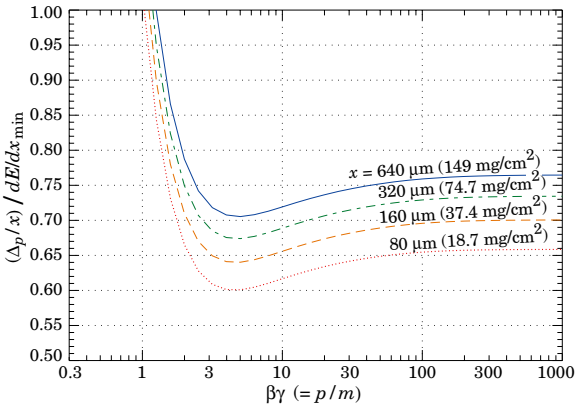

Figure 27.7: Most probable energy loss in silicon, scaled to the mean loss of a minimum ionizing particle, 388 eV/μm (1.66 MeV g^{-1}cm^2).

27.2.7. ***Ionization yields***: Physicists frequently relate total energy loss to the number of ion pairs produced near the particle's track. This relation becomes complicated for relativistic particles due to the wandering of energetic knock-on electrons whose ranges exceed the dimensions of the fiducial volume. For a qualitative appraisal of the nonlocality of energy deposition in various media by such modestly energetic knock-on electrons, see Ref. 29. The mean local energy dissipation per local ion pair produced, W, while essentially constant for relativistic particles, increases at slow particle speeds [30]. For gases, W can be surprisingly sensitive to trace amounts of various contaminants [30]. Furthermore, ionization yields in practical cases may be greatly influenced by such factors as subsequent recombination [31].

27.3. Multiple scattering through small angles

A charged particle traversing a medium is deflected by many small-angle scatters. Most of this deflection is due to Coulomb scattering from nuclei, and hence the effect is called multiple Coulomb scattering. (However, for hadronic projectiles, the strong interactions also contribute to multiple scattering.) The Coulomb scattering distribution is well represented by the theory of Molière [32]. It is roughly Gaussian for small deflection angles, but at larger angles (greater than a few θ_0, defined below) it behaves like Rutherford scattering, having larger tails than does a Gaussian distribution.

If we define

$$\theta_0 = \theta^{\rm rms}_{\rm plane} = \frac{1}{\sqrt{2}}\,\theta^{\rm rms}_{\rm space} . \qquad (27.9)$$

then it is sufficient for many applications to use a Gaussian approximation for the central 98% of the projected angular distribution, with a width given by [33,34]

$$\theta_0 = \frac{13.6\ {\rm MeV}}{\beta cp}\, z\,\sqrt{x/X_0}\Big[1 + 0.038\ln(x/X_0)\Big] . \qquad (27.10)$$

Here p, βc, and z are the momentum, velocity, and charge number of the incident particle, and x/X_0 is the thickness of the scattering medium in radiation lengths (defined below). This value of θ_0 is from a fit to Molière distribution [32] for singly charged particles with $\beta = 1$ for all Z, and is accurate to 11% or better for $10^{-3} < x/X_0 < 100$.

Eq. (27.10) describes scattering from a single material, while the usual problem involves the multiple scattering of a particle traversing many different layers and mixtures. Since it is from a fit to a Molière distribution, it is incorrect to add the individual θ_0 contributions in quadrature; the result is systematically too small. It is much more accurate to apply Eq. (27.10) once, after finding x and X_0 for the combined scatterer.

Lynch and Dahl have extended this phenomenological approach, fitting Gaussian distributions to a variable fraction of the Molière distribution for arbitrary scatterers [34], and achieve accuracies of 2% or better.

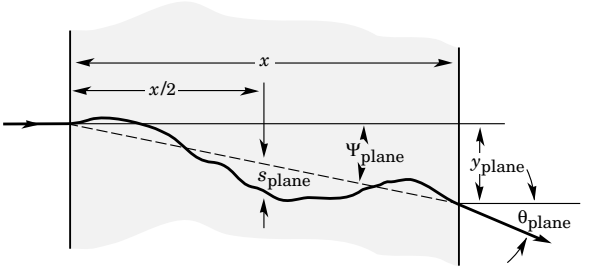

Figure 27.8: Quantities used to describe multiple Coulomb scattering. The particle is incident in the plane of the figure.

The nonprojected (space) and projected (plane) angular distributions are given approximately by [32]

$$\frac{1}{2\pi\,\theta_0^2}\,\exp\left(-\frac{\theta^2_{\rm space}}{2\theta_0^2}\right)\,d\Omega\ , \tag{27.11}$$

$$\frac{1}{\sqrt{2\pi}\,\theta_0}\,\exp\left(-\frac{\theta^2_{\rm plane}}{2\theta_0^2}\right)\,d\theta_{\rm plane}\ , \tag{27.12}$$

where θ is the deflection angle. In this approximation, $\theta^2_{\rm space} \approx (\theta^2_{{\rm plane},x} + \theta^2_{{\rm plane},y})$, where the x and y axes are orthogonal to the direction of motion, and $d\Omega \approx d\theta_{{\rm plane},x}\,d\theta_{{\rm plane},y}$. Deflections into $\theta_{{\rm plane},x}$ and $\theta_{{\rm plane},y}$ are independent and identically distributed.

Figure 27.8 shows these and other quantities sometimes used to describe multiple Coulomb scattering. They are

$$\psi^{\rm\ rms}_{\rm\ plane} = \frac{1}{\sqrt{3}}\,\theta^{\rm\ rms}_{\rm\ plane} = \frac{1}{\sqrt{3}}\,\theta_0\ , \tag{27.13}$$

$$y^{\rm\ rms}_{\rm\ plane} = \frac{1}{\sqrt{3}}\,x\,\theta^{\rm\ rms}_{\rm\ plane} = \frac{1}{\sqrt{3}}\,x\,\theta_0\ , \tag{27.14}$$

$$s^{\rm\ rms}_{\rm\ plane} = \frac{1}{4\sqrt{3}}\,x\,\theta^{\rm\ rms}_{\rm\ plane} = \frac{1}{4\sqrt{3}}\,x\,\theta_0\ . \tag{27.15}$$

All the quantitative estimates in this section apply only in the limit of small $\theta^{\rm\ rms}_{\rm\ plane}$ and in the absence of large-angle scatters. The random variables s, ψ, y, and θ in a given plane are distributed in a correlated fashion (see Sec. 31.1 of this *Review* for the definition of the correlation coefficient). Obviously, $y \approx x\psi$. In addition, y and θ have the correlation coefficient $\rho_{y\theta} = \sqrt{3}/2 \approx 0.87$. For Monte Carlo generation of a joint $(y_{\rm\ plane}, \theta_{\rm plane})$ distribution, or for other calculations, it may be most convenient to work with independent Gaussian random variables (z_1, z_2) with mean zero and variance one, and then set

$$\begin{aligned} y_{\rm plane} &= z_1\,x\,\theta_0(1-\rho^2_{y\theta})^{1/2}/\sqrt{3} + z_2\,\rho_{y\theta}\,x\,\theta_0/\sqrt{3} \\ &= z_1\,x\,\theta_0/\sqrt{12} + z_2\,x\,\theta_0/2\,; \end{aligned} \tag{27.16}$$

$$\theta_{\rm plane} = z_2\,\theta_0\ . \tag{27.17}$$

Note that the second term for $y_{\rm\ plane}$ equals $x\,\theta_{\rm plane}/2$ and represents the displacement that would have occurred had the deflection $\theta_{\rm plane}$ all occurred at the single point $x/2$.

For heavy ions the multiple Coulomb scattering has been measured and compared with various theoretical distributions [35].

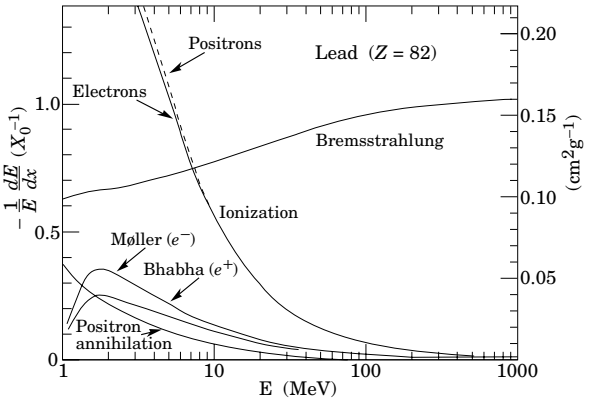

Figure 27.9: Fractional energy loss per radiation length in lead as a function of electron or positron energy. Electron (positron) scattering is considered as ionization when the energy loss per collision is below 0.255 MeV, and as Møller (Bhabha) scattering when it is above. Adapted from Fig. 3.2 from Messel and Crawford, *Electron-Photon Shower Distribution Function Tables for Lead, Copper, and Air Absorbers*, Pergamon Press, 1970. Messel and Crawford use X_0(Pb) = 5.82 g/cm^2, but we have modified the figures to reflect the value given in the Table of Atomic and Nuclear Properties of Materials (X_0(Pb) = 6.37 g/cm^2).

27.4. Photon and electron interactions in matter

27.4.1. ***Radiation length***: High-energy electrons predominantly lose energy in matter by bremsstrahlung, and high-energy photons by e^+e^- pair production. The characteristic amount of matter traversed for these related interactions is called the radiation length X_0, usually measured in g cm^{-2}. It is both (a) the mean distance over which a high-energy electron loses all but $1/e$ of its energy by bremsstrahlung, and (b) $\frac{7}{9}$ of the mean free path for pair production by a high-energy photon [36]. It is also the appropriate scale length for describing high-energy electromagnetic cascades. X_0 has been calculated and tabulated by Y.S. Tsai [37]:

$$\frac{1}{X_0} = 4\alpha r_e^2\,\frac{N_A}{A}\Big\{Z^2\big[L_{\rm rad} - f(Z)\big] + Z\,L'_{\rm rad}\Big\}\ . \tag{27.18}$$

For $A = 1$ g mol^{-1}, $4\alpha r_e^2 N_A/A = (716.408\ {\rm g\ cm^{-2}})^{-1}$. $L_{\rm rad}$ and $L'_{\rm rad}$ are given in Table 27.2. The function $f(Z)$ is an infinite sum, but for elements up to uranium can be represented to 4-place accuracy by

$$\begin{aligned} f(Z) = a^2\big[(1+a^2)^{-1} + 0.20206 \\ -0.0369\,a^2 + 0.0083\,a^4 - 0.002\,a^6\big]\ , \end{aligned} \tag{27.19}$$

where $a = \alpha Z$ [38].

Table 27.2: Tsai's $L_{\rm rad}$ and $L'_{\rm rad}$, for use in calculating the radiation length in an element using Eq. (27.18).

Element	Z	$L_{\rm rad}$	$L'_{\rm rad}$
H	1	5.31	6.144
He	2	4.79	5.621
Li	3	4.74	5.805
Be	4	4.71	5.924
Others	>4	$\ln(184.15\,Z^{-1/3})$	$\ln(1194\,Z^{-2/3})$

Although it is easy to use Eq. (27.18) to calculate X_0, the functional dependence on Z is somewhat hidden. Dahl provides a compact fit to the data [39]:

$$X_0 = \frac{716.4\ {\rm g\ cm^{-2}}\,A}{Z(Z+1)\ln(287/\sqrt{Z})}\ . \tag{27.20}$$

Results using this formula agree with Tsai's values to better than 2.5% for all elements except helium, where the result is about 5% low.

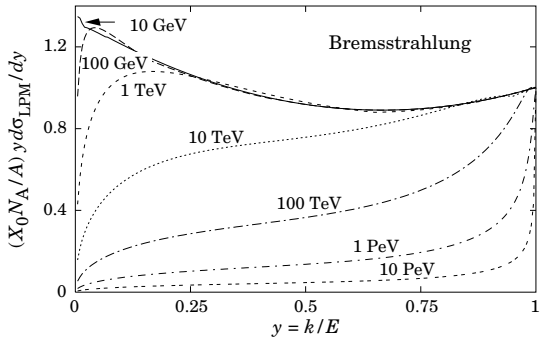

Figure 27.10: The normalized bremsstrahlung cross section $k\, d\sigma_{LPM}/dk$ in lead versus the fractional photon energy $y = k/E$. The vertical axis has units of photons per radiation length.

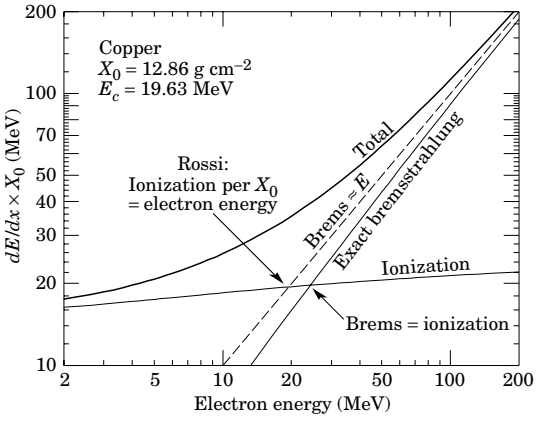

Figure 27.11: Two definitions of the critical energy E_c.

The radiation length in a mixture or compound may be approximated by

$$1/X_0 = \sum w_j/X_j \ , \tag{27.21}$$

where w_j and X_j are the fraction by weight and the radiation length for the jth element.

27.4.2. ***Energy loss by electrons***: At low energies electrons and positrons primarily lose energy by ionization, although other processes (Møller scattering, Bhabha scattering, e^+ annihilation) contribute, as shown in Fig. 27.9. While ionization loss rates rise logarithmically with energy, bremsstrahlung losses rise nearly linearly (fractional loss is nearly independent of energy), and dominates above a few tens of MeV in most materials

Ionization loss by electrons and positrons differs from loss by heavy particles because of the kinematics, spin, and the identity of the incident electron with the electrons which it ionizes. Complete discussions and tables can be found in Refs. 8, 9, and 28.

At very high energies and except at the high-energy tip of the bremsstrahlung spectrum, the cross section can be approximated in the "complete screening case" as [37]

$$d\sigma/dk = (1/k)4\alpha r_e^2 \{(\tfrac{4}{3} - \tfrac{4}{3}y + y^2)[Z^2(L_{\rm rad} - f(Z)) + Z\, L'_{\rm rad}] + \tfrac{1}{9}(1-y)(Z^2+Z)\} \ , \tag{27.22}$$

where $y = k/E$ is the fraction of the electron's energy transfered to the radiated photon. At small y (the "infrared limit") the term on the second line can reach 2.5%. If it is ignored and the first line simplified with the definition of X_0 given in Eq. (27.18), we have

$$\frac{d\sigma}{dk} = \frac{A}{X_0 N_A k}\left(\tfrac{4}{3} - \tfrac{4}{3}y + y^2\right) \ . \tag{27.23}$$

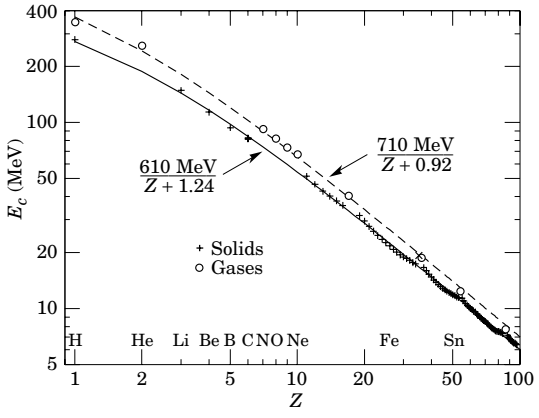

Figure 27.12: Electron critical energy for the chemical elements, using Rossi's definition [3]. The fits shown are for solids and liquids (solid line) and gases (dashed line). The rms deviation is 2.2% for the solids and 4.0% for the gases. (Computed with code supplied by A. Fassó.)

This cross section (times k) is shown by the top curve in Fig. 27.10.

This formula is accurate except in near $y = 1$, where screening may become incomplete, and near $y = 0$, where the infrared divergence is removed by the interference of bremsstrahlung amplitudes from nearby scattering centers (the LPM effect) [40,41] and dielectric supression [42,43]. These and other supression effects in bulk media are discussed in Sec. 27.4.5.

With decreasing energy ($E \lesssim 10$ GeV) the high-y cross section drops and the curves become rounded as $y \to 1$. Curves of this familar shape can be seen in Rossi [3] (Figs. 2.11.2,3); see also the review by Koch & Motz [44].

Except at these extremes, and still in the complete-screening approximation, the the number of photons with energies between $k_{\rm min}$ and $k_{\rm max}$ emitted by an electron travelling a distance $d \ll X_0$ is

$$N_\gamma = \frac{d}{X_0}\left[\frac{4}{3}\ln\left(\frac{k_{\rm max}}{k_{\rm min}}\right) - \frac{4(k_{\rm max} - k_{\rm min})}{3E} + \frac{(k_{\rm max} - k_{\rm min})^2}{2E^2}\right] \ . \tag{27.24}$$

27.4.3. ***Critical energy***: An electron loses energy by bremsstrahlung at a rate nearly proportional to its energy, while the ionization loss rate varies only logarithmically with the electron energy. The *critical energy* E_c is sometimes defined as the energy at which the two loss rates are equal [45]. Berger and Seltzer [45] also give the approximation $E_c = (800\ {\rm MeV})/(Z + 1.2)$. This formula has been widely quoted, and has been given in older editions of this *Review* [46]. Among alternate definitions is that of Rossi [3], who defines the critical energy as the energy at which the ionization loss per radiation length is equal to the electron energy. Equivalently, it is the same as the first definition with the approximation $|dE/dx|_{\rm brems} \approx E/X_0$. This form has been found to describe transverse electromagnetic shower development more accurately (see below). These definitions are illustrated in the case of copper in Fig. 27.11.

The accuracy of approximate forms for E_c has been limited by the failure to distinguish between gases and solid or liquids, where there is a substantial difference in ionization at the relevant energy because of the density effect. We distinguish these two cases in Fig. 27.12. Fits were also made with functions of the form $a/(Z+b)^\alpha$, but α was found to be essentially unity. Since E_c also depends on A, I, and other factors, such forms are at best approximate.

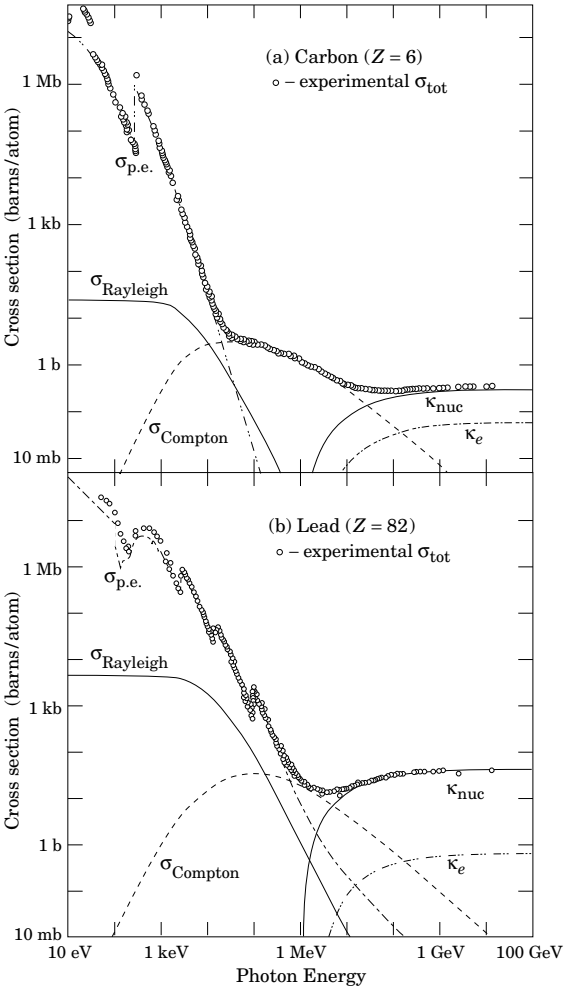

Figure 27.13: Photon total cross sections as a function of energy in carbon and lead, showing the contributions of different processes:

$\sigma_{\rm p.e.}$ = Atomic photoelectric effect (electron ejection, photon absorption)

$\sigma_{\rm Rayleigh}$ = Coherent scattering (Rayleigh scattering—atom neither ionized nor excited)

$\sigma_{\rm Compton}$ = Incoherent scattering (Compton scattering off an electron)

$\kappa_{\rm nuc}$ = Pair production, nuclear field

κ_e = Pair production, electron field

Data from Hubbell, Gimm, and Øverbø, J. Phys. Chem. Ref. Data **9**, 1023 (1980). Curves for these and other elements, compounds, and mixtures may be obtained from `http://physics.nist.gov/PhysRefData`. The photon total cross section is approximately flat for at least two decades beyond the energy range shown. Original figures courtesy J.H. Hubbell (NIST).

27.4.4. ***Energy loss by photons***: Contributions to the photon cross section in a light element (carbon) and a heavy element (lead) are shown in Fig. 27.13. At low energies it is seen that the photoelectric effect dominates, although Compton scattering, Rayleigh scattering, and photonuclear absorption also contribute. The photoelectric cross section is characterized by discontinuities (absorption edges) as thresholds for photoionization of various atomic levels are reached.

Photon attenuation lengths for a variety of elements are shown in Fig. 27.15, and data for 30 eV$< k <$100 GeV for all elements is available from the web pages given in the caption. Here k is the photon energy.

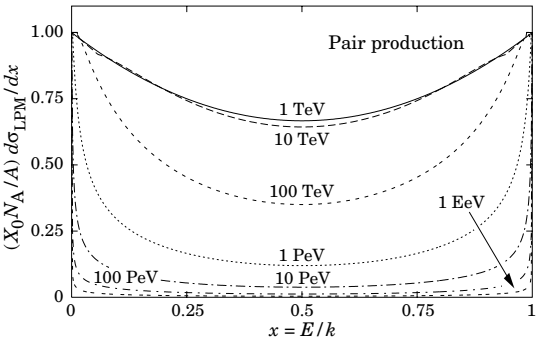

Figure 27.14: The normalized pair production cross section $d\sigma_{LPM}/dy$, versus fractional electron energy $x = E/k$.

The increasing domination of pair production as the energy increases is shown in Fig. 27.16. Using approximations similar to those used to obtain Eq. (27.23), Tsai's formula for the differential cross section [37] reduces to

$$\frac{d\sigma}{dE} = \frac{A}{X_0 N_A}\left[1 - \tfrac{4}{3}x(1-x)\right] \qquad (27.25)$$

in the complete-screening limit valid at high energies. Here $x = E/k$ is the fractional energy transfer to the pair-produced electron (or positron), and k is the incident photon energy. The cross section is very closely related to that for bremsstrahlung, since the Feynman diagrams are variants of one another. The cross section is of necessity symmetric between x and $1 - x$, as can be seen by the solid curve in Fig. 27.14. See the review by Motz, Olsen, & Koch for a more detailed treatment [47].

Eq. (27.25) may be integrated to find the high-energy limit for the total e^+e^- pair-production cross section:

$$\sigma = \tfrac{7}{9}(A/X_0 N_A)\ . \qquad (27.26)$$

Equation Eq. (27.26) is accurate to within a few percent down to energies as low as 1 GeV, particularly for high-Z materials.

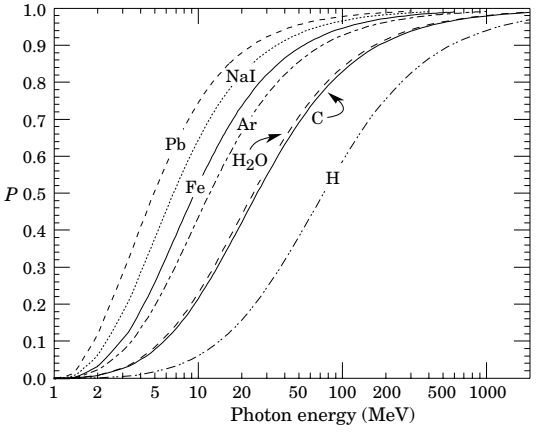

Figure 27.16: Probability P that a photon interaction will result in conversion to an e^+e^- pair. Except for a few-percent contribution from photonuclear absorption around 10 or 20 MeV, essentially all other interactions in this energy range result in Compton scattering off an atomic electron. For a photon attenuation length λ (Fig. 27.15), the probability that a given photon will produce an electron pair (without first Compton scattering) in thickness t of absorber is $P[1 - \exp(-t/\lambda)]$.

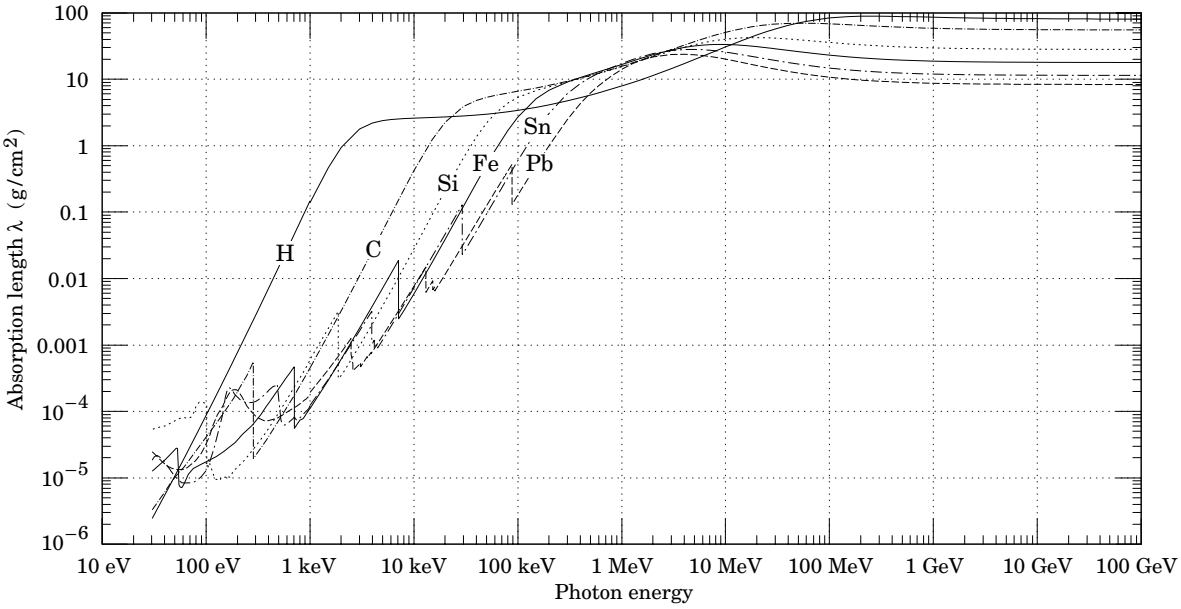

Fig. 27.15: The photon mass attenuation length (or mean free path) $\lambda = 1/(\mu/\rho)$ for various elemental absorbers as a function of photon energy. The mass attenuation coefficient is μ/ρ, where ρ is the density. The intensity I remaining after traversal of thickness t (in mass/unit area) is given by $I = I_0 \exp(-t/\lambda)$. The accuracy is a few percent. For a chemical compound or mixture, $1/\lambda_{\rm eff} \approx \sum_{\rm elements} w_Z/\lambda_Z$, where w_Z is the proportion by weight of the element with atomic number Z. The processes responsible for attenuation are given in not Fig. 27.9. Since coherent processes are included, not all these processes result in energy deposition. The data for 30 eV $< E <$ 1 keV are obtained from `http://www-cxro.lbl.gov/optical_constants` (courtesy of Eric M. Gullikson, LBNL). The data for 1 keV $< E <$ 100 GeV are from `http://physics.nist.gov/PhysRefData`, through the courtesy of John H. Hubbell (NIST).

27.4.5. ***Bremsstrahlung and pair production at very high energies:*** At ultrahigh energies, Eqns. 27.22–27.26 will fail because of quantum mechanical interference between amplitudes from different scattering centers. Since the longitudinal momentum transfer to a given center is small ($\propto k/E^2$, in the case of bremsstrahlung), the interaction is spread over a comparatively long distance called the formation length ($\propto E^2/k$) via the uncertainty principle. In alternate language, the formation length is the distance over which the highly relatistic electron and the photon "split apart." The interference is usually destructive. Calculations of the "Landau-Pomeranchuk-Migdal" (LPM) effect may be made semi-classically based on the average multiple scattering, or more rigorously using a quantum transport approach [40,41].

In amorphous media, bremsstrahlung is suppressed if the photon energy k is less than E^2/E_{LPM} [41], where*

$$E_{LPM} = \frac{(m_e c^2)^2 \alpha \rho X_0}{4\pi\hbar c} = (7.7 \text{ TeV/cm}) \times \rho X_0 \,. \qquad (27.27)$$

Since physical distances are involved, ρX_0, in cm, appears. The energy-weighted bremsstrahlung spectrum for lead, $k\, d\sigma_{LPM}/dk$, is shown in Fig. 27.10. With appropriate scaling by ρX_0, other materials behave similarly.

For photons, pair production is reduced for $E(k-E) > k\,E_{LPM}$. The pair-production cross sections for different photon energies are shown in Fig. 27.14.

If $k \ll E$, several additional mechanisms can also produce suppression. When the formation length is long, even weak factors can perturb the interaction. For example, the emitted photon can coherently forward scatter off of the electrons in the media. Because of this, for $k < \omega_p E/m_e \sim 10^{-4}$, bremsstrahlung is suppressed by a factor $(k m_e/\omega_p E)^2$ [43]. Magnetic fields can also suppress bremsstrahlung.

In crystalline media, the situation is more complicated, with coherent enhancement or suppression possible. The cross section depends on the electron and photon energies and the angles between the particle direction and the crystalline axes [41].

* This definition differs from that of Ref. 48 by a factor of two. E_{LPM} scales as the 4th power of the mass of the incident particle, so that $E_{LPM} = (1.4 \times 10^{10} \text{ TeV/cm}) \times \rho X_0$ for a muon.

27.5. Electromagnetic cascades

When a high-energy electron or photon is incident on a thick absorber, it initiates an electromagnetic cascade as pair production and bremsstrahlung generate more electrons and photons with lower energy. The longitudinal development is governed by the high-energy part of the cascade, and therefore scales as the radiation length in the material. Electron energies eventually fall below the critical energy, and then dissipate their energy by ionization and excitation rather than by the generation of more shower particles. In describing shower behavior, it is therefore convenient to introduce the scale variables

$$t = x/X_0 \,, \qquad y = E/E_c \,, \qquad (27.28)$$

so that distance is measured in units of radiation length and energy in units of critical energy.

Longitudinal profiles from an EGS4 [49] simulation of a 30 GeV electron-induced cascade in iron are shown in Fig. 27.17. The number of particles crossing a plane (very close to Rossi's II function [3]) is sensitive to the cutoff energy, here chosen as a total energy of 1.5 MeV for both electrons and photons. The electron number falls off more quickly than energy deposition. This is because, with increasing depth, a larger fraction of the cascade energy is carried by photons. Exactly what a calorimeter measures depends on the device, but it is not likely to be exactly any of the profiles shown. In gas counters it may be very close to the electron number, but in glass Cherenkov detectors and other devices with "thick" sensitive regions it is closer to the energy deposition (total track length). In such detectors the signal is proportional to the "detectable" track length T_d, which is in general less than the total track length T. Practical devices are

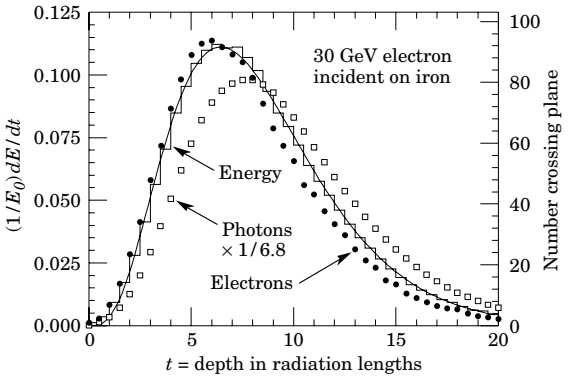

Figure 27.17: An EGS4 simulation of a 30 GeV electron-induced cascade in iron. The histogram shows fractional energy deposition per radiation length, and the curve is a gamma-function fit to the distribution. Circles indicate the number of electrons with total energy greater than 1.5 MeV crossing planes at $X_0/2$ intervals (scale on right) and the squares the number of photons with $E \geq 1.5$ MeV crossing the planes (scaled down to have same area as the electron distribution).

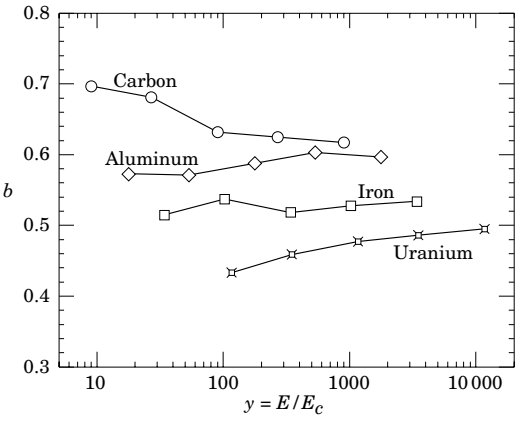

Figure 27.18: Fitted values of the scale factor b for energy deposition profiles obtained with EGS4 for a variety of elements for incident electrons with $1 \leq E_0 \leq 100$ GeV. Values obtained for incident photons are essentially the same.

sensitive to electrons with energy above some detection threshold E_d, and $T_d = T\,F(E_d/E_c)$. An analytic form for $F(E_d/E_c)$ obtained by Rossi [3] is given by Fabjan [50]; see also Amaldi [51].

The mean longitudinal profile of the energy deposition in an electromagnetic cascade is reasonably well described by a gamma distribution [52]:

$$\frac{dE}{dt} = E_0\, b\, \frac{(bt)^{a-1} e^{-bt}}{\Gamma(a)} \tag{27.29}$$

The maximum $t_{\max}$ occurs at $(a-1)/b$. We have made fits to shower profiles in elements ranging from carbon to uranium, at energies from 1 GeV to 100 GeV. The energy deposition profiles are well described by Eq. (27.29) with

$$t_{\max} = (a-1)/b = 1.0 \times (\ln y + C_j)\,, \qquad j = e, \gamma\,, \tag{27.30}$$

where $C_e = -0.5$ for electron-induced cascades and $C_\gamma = +0.5$ for photon-induced cascades. To use Eq. (27.29), one finds $(a-1)/b$ from Eq. (27.30) and Eq. (27.28), then finds a either by assuming $b \approx 0.5$ or by finding a more accurate value from Fig. 27.18. The results are very similar for the electron number profiles, but there is some dependence on the atomic number of the medium. A similar form for the electron number maximum was obtained by Rossi in the context of his "Approximation B," [3] (see Fabjan's review in Ref. 50), but with $C_e = -1.0$ and $C_\gamma = -0.5$; we regard this as superseded by the EGS4 result.

The "shower length" $X_s = X_0/b$ is less conveniently parameterized, since b depends upon both Z and incident energy, as shown in Fig. 27.18. As a corollary of this Z dependence, the number of electrons crossing a plane near shower maximum is underestimated using Rossi's approximation for carbon and seriously overestimated for uranium. Essentially the same b values are obtained for incident electrons and photons. For many purposes it is sufficient to take $b \approx 0.5$.

The gamma function distribution is very flat near the origin, while the EGS4 cascade (or a real cascade) increases more rapidly. As a result Eq. (27.29) fails badly for about the first two radiation lengths; it was necessary to exclude this region in making fits.

Because fluctuations are important, Eq. (27.29) should be used only in applications where average behavior is adequate. Grindhammer *et al.* have developed fast simulation algorithms in which the variance and correlation of a and b are obtained by fitting Eq. (27.29) to individually simulated cascades, then generating profiles for cascades using a and b chosen from the correlated distributions [53].

The transverse development of electromagnetic showers in different materials scales fairly accurately with the *Molière radius* R_M, given by [54,55]

$$R_M = X_0\, E_s/E_c\,, \tag{27.31}$$

where $E_s \approx 21$ MeV (Table 27.1), and the Rossi definition of E_c is used.

In a material containing a weight fraction w_j of the element with critical energy E_{cj} and radiation length X_j, the Molière radius is given by

$$\frac{1}{R_M} = \frac{1}{E_s} \sum \frac{w_j\, E_{cj}}{X_j}\,. \tag{27.32}$$

Measurements of the lateral distribution in electromagnetic cascades are shown in Refs. 54 and 55. On the average, only 10% of the energy lies outside the cylinder with radius R_M. About 99% is contained inside of $3.5R_M$, but at this radius and beyond composition effects become important and the scaling with R_M fails. The distributions are characterized by a narrow core, and broaden as the shower develops. They are often represented as the sum of two Gaussians, and Grindhammer [53] describes them with the function

$$f(r) = \frac{2r\,R^2}{(r^2 + R^2)^2}\,, \tag{27.33}$$

where R is a phenomenological function of x/X_0 and $\ln E$.

At high enough energies, the LPM effect (Sec. 27.4.5) reduces the cross sections for bremsstrahlung and pair production, and hence can cause significant enlongation of electromagnetic cascades [41].

27.6. Muon energy loss at high energy

At sufficiently high energies, radiative processes become more important than ionization for all charged particles. For muons and pions in materials such as iron, this "critical energy" occurs at several hundred GeV. (There is no simple scaling with particle mass, but for protons the "critical energy" is much, much higher.) Radiative effects dominate the energy loss of energetic muons found in cosmic rays or produced at the newest accelerators. These processes are characterized by small cross sections, hard spectra, large energy fluctuations, and the associated generation of electromagnetic and (in the case of photonuclear interactions) hadronic showers [56–64]. As a consequence, at these energies the treatment of energy loss as a uniform and continuous process is for many purposes inadequate.

It is convenient to write the average rate of muon energy loss as [65]

$$-dE/dx = a(E) + b(E)\,E\,. \tag{27.34}$$

Here $a(E)$ is the ionization energy loss given by Eq. (27.1), and $b(E)$ is the sum of e^+e^- pair production, bremsstrahlung, and photonuclear contributions. To the approximation that these slowly-varying functions are constant, the mean range x_0 of a muon with initial energy E_0 is given by

$$x_0 \approx (1/b) \ln(1 + E_0/E_{\mu c})\,, \tag{27.35}$$

where $E_{\mu c} = a/b$. Figure 27.19 shows contributions to $b(E)$ for iron. Since $a(E) \approx 0.002$ GeV g^{-1} cm^2, $b(E)E$ dominates the energy loss above several hundred GeV, where $b(E)$ is nearly constant. The rates of energy loss for muons in hydrogen, uranium, and iron are shown in Fig. 27.20 [1].

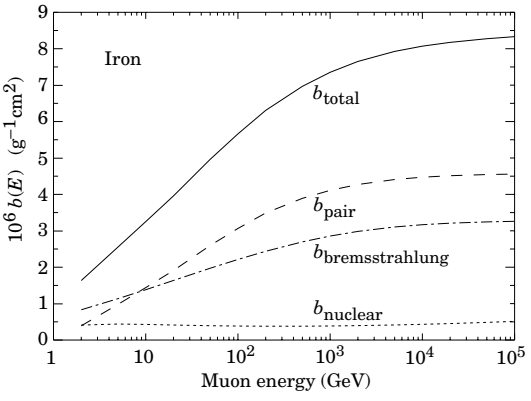

Figure 27.19: Contributions to the fractional energy loss by muons in iron due to e^+e^- pair production, bremsstrahlung, and photonuclear interactions, as obtained from Groom *et al.* [1] except for post-Born corrections to the cross section for direct pair production from atomic electrons.

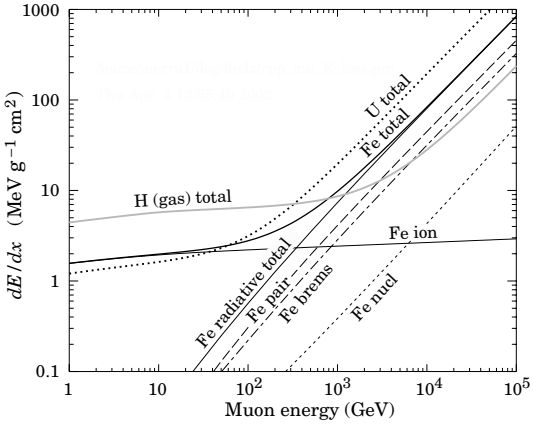

Figure 27.20: The average energy loss of a muon in hydrogen, iron, and uranium as a function of muon energy. Contributions to dE/dx in iron from ionization and the processes shown in Fig. 27.19 are also shown.

The "muon critical energy" $E_{\mu c}$ can be defined more exactly as the energy at which radiative and ionization losses are equal, and can be found by solving $E_{\mu c} = a(E_{\mu c})/b(E_{\mu c})$. This definition corresponds to the solid-line intersection in Fig. 27.11, and is different from the Rossi definition we used for electrons. It serves the same function: below $E_{\mu c}$ ionization losses dominate, and above $E_{\mu c}$ radiative effects dominate. The dependence of $E_{\mu c}$ on atomic number Z is shown in Fig. 27.21.

The radiative cross sections are expressed as functions of the fractional energy loss ν. The bremsstrahlung cross section goes roughly as $1/\nu$ over most of the range, while for the pair production case the distribution goes as ν^{-3} to ν^{-2} [66]. "Hard" losses are therefore more probable in bremsstrahlung, and in fact energy losses due to pair production may very nearly be treated as continuous. The simulated [64] momentum distribution of an incident 1 TeV/c muon beam after it crosses 3 m of iron is shown in Fig. 27.22.

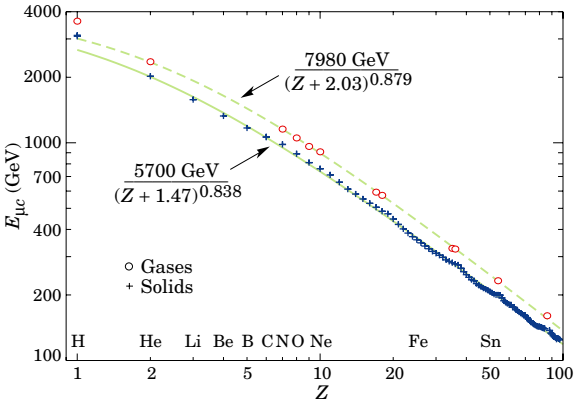

Figure 27.21: Muon critical energy for the chemical elements, defined as the energy at which radiative and ionization energy loss rates are equal [1]. The equality comes at a higher energy for gases than for solids or liquids with the same atomic number because of a smaller density effect reduction of the ionization losses. The fits shown in the figure exclude hydrogen. Alkali metals fall 3–4% above the fitted function, while most other solids are within 2% of the function. Among the gases the worst fit is for radon (2.7% high).

The most probable loss is 8 GeV, or 3.4 MeV g^{-1}cm^2. The full width at half maximum is 9 GeV/c, or 0.9%. The radiative tail is almost entirely due to bremsstrahlung, although most of the events in which more than 10% of the incident energy lost experienced relatively hard photonuclear interactions. The latter can exceed detector resolution [67], necessitating the reconstruction of lost energy. Tables [1] list the stopping power as 9.82 MeV g^{-1}cm^2 for a 1 TeV muon, so that the mean loss should be 23 MeV ($\approx$ 23 MeV/c), for a final momentum of 977 MeV/c, far below the peak. This agrees with the indicated mean calculated from the simulation. Electromagnetic and hadronic cascades in detector materials can obscure muon tracks in detector planes and reduce tracking efficiency [68].

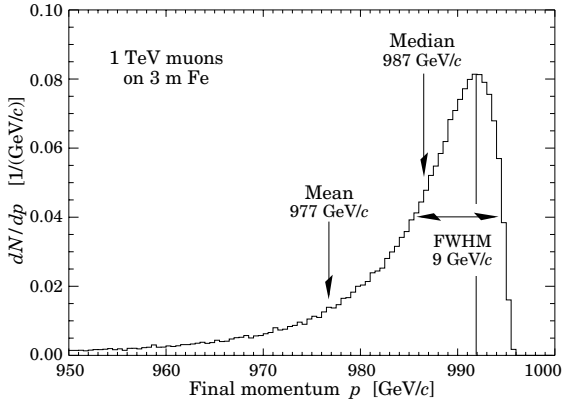

Figure 27.22: The momentum distribution of 1 TeV/c muons after traversing 3 m of iron as calculated withthe MARS14 Monte Carlo code [64] by S.I. Striganov [1].

27.7. Cherenkov and transition radiation [5,69,70]

A charged particle radiates if its velocity is greater than the local phase velocity of light (Cherenkov radiation) or if it crosses suddenly from one medium to another with different optical properties (transition radiation). Neither process is important for energy loss, but both are used in high-energy physics detectors.

Cherenkov Radiation. The half-angle θ_c of the Cherenkov cone for a particle with velocity βc in a medium with index of refraction n is

$$\theta_c = \arccos(1/n\beta) \approx \sqrt{2(1-1/n\beta)} \quad \text{for small } \theta_c, \textit{e.g.} \text{ in gases.} \tag{27.36}$$

The threshold velocity β_t is $1/n$, and $\gamma_t = 1/(1-\beta_t^2)^{1/2}$. Therefore, $\beta_t\gamma_t = 1/(2\delta+\delta^2)^{1/2}$, where $\delta = n-1$. Values of δ for various commonly used gases are given as a function of pressure and wavelength in Ref. 71. For values at atmospheric pressure, see Table 6.1. Data for other commonly used materials are given in Ref. 72.

The number of photons produced per unit path length of a particle with charge ze and per unit energy interval of the photons is

$$\frac{d^2N}{dEdx} = \frac{\alpha z^2}{\hbar c}\sin^2\theta_c = \frac{\alpha^2 z^2}{r_e\, m_e c^2}\left(1-\frac{1}{\beta^2 n^2(E)}\right) \approx 370 \sin^2\theta_c(E)\ \mathrm{eV}^{-1}\mathrm{cm}^{-1} \qquad (z=1)\,, \tag{27.37}$$

or, equivalently,

$$\frac{d^2N}{dxd\lambda} = \frac{2\pi\alpha z^2}{\lambda^2}\left(1-\frac{1}{\beta^2 n^2(\lambda)}\right)\,. \tag{27.38}$$

The index of refraction is a function of photon energy E, as is the sensitivity of the transducer used to detect the light. For practical use, Eq. (27.37) must be multiplied by the the transducer response function and integrated over the region for which $\beta\, n(E) > 1$. Further details are given in the discussion of Cherenkov detectors in the Detectors section (Sec. 28 of this *Review*).

Transition radiation. The energy radiated when a particle with charge ze crosses the boundary between vacuum and a medium with plasma frequency ω_p is

$$I = \alpha z^2 \gamma \hbar\omega_p/3\,, \tag{27.39}$$

where

$$\hbar\omega_p = \sqrt{4\pi N_e r_e^3}\; m_e c^2/\alpha = \sqrt{4\pi N_e a_\infty^3}\; 2\times 13.6\ \mathrm{eV}\,. \tag{27.40}$$

Here N_e is the electron density in the medium, r_e is the classical electron radius, and a_∞ is the Bohr radius. For styrene and similar materials, $\sqrt{4\pi N_e a_\infty^3} \approx 0.8$, so that $\hbar\omega_p \approx 20$ eV. The typical emission angle is $1/\gamma$.

The radiation spectrum is logarithmically divergent at low energies and decreases rapidly for $\hbar\omega/\gamma\hbar\omega_p > 1$. About half the energy is emitted in the range $0.1 \le \hbar\omega/\gamma\hbar\omega_p \le 1$. For a particle with $\gamma = 10^3$, the radiated photons are in the soft x-ray range 2 to 20 keV. The γ dependence of the emitted energy thus comes from the hardening of the spectrum rather than from an increased quantum yield. For a typical radiated photon energy of $\gamma\hbar\omega_p/4$, the quantum yield is

$$N_\gamma \approx \frac{1}{2}\,\frac{\alpha z^2\gamma\hbar\omega_p}{3}\Big/\frac{\gamma\hbar\omega_p}{4} \approx \tfrac{2}{3}\alpha z^2 \approx 0.5\% \times z^2\,. \tag{27.41}$$

More precisely, the number of photons with energy $\hbar\omega > \hbar\omega_0$ is given by [5]

$$N_\gamma(\hbar\omega > \hbar\omega_0) = \frac{\alpha z^2}{\pi}\left[\left(\ln\frac{\gamma\hbar\omega_p}{\hbar\omega_0}-1\right)^2 + \frac{\pi^2}{12}\right]\,, \tag{27.42}$$

within corrections of order $(\hbar\omega_0/\gamma\hbar\omega_p)^2$. The number of photons above a fixed energy $\hbar\omega_0 \ll \gamma\hbar\omega_p$ thus grows as $(\ln\gamma)^2$, but the number above a fixed fraction of $\gamma\hbar\omega_p$ (as in the example above) is constant. For example, for $\hbar\omega > \gamma\hbar\omega_p/10$, $N_\gamma = 2.519\,\alpha z^2/\pi = 0.59\% \times z^2$.

The yield can be increased by using a stack of plastic foils with gaps between. However, interference can be important, and the soft x rays are readily absorbed in the foils. The first problem can be overcome by choosing thicknesses and spacings large compared to the "formation length" $D = \gamma c/\omega_p$, which in practical situations is tens of μm. Other practical problems are discussed in Sec. 28.

References:

1. D.E. Groom, N.V. Mokhov, and S.I. Striganov, "Muon stopping-power and range tables: 10 MeV–100 TeV" Atomic Data and Nuclear Data Tables **78**, 183–356 (2001). Since submission of this paper it has become likely that post-Born corrections to the direct pair production cross section should be made. Code used to make Figs. 27.19, 27.20, and 27.11 included these corrections [D.Yu. Ivanov *et al.*, Phys. Lett. **B442**, 453 (1998)]. The effect is negligible for except at high Z. (It is less than 1% for iron);
   More extensive tables in printable and machine-readable formats are given at `http://pdg.lbl.gov/AtomicNuclearProperties/`.
2. "Stopping Powers and Ranges for Protons and Alpha Particles," ICRU Report No. 49 (1993);
   Tables and graphs of these data are available at `http://physics.nist.gov/PhysRefData/`.
3. B. Rossi, *High Energy Particles*, Prentice-Hall, Inc., Englewood Cliffs, NJ, 1952.
4. U. Fano, Ann. Rev. Nucl. Sci. **13**, 1 (1963).
5. J.D. Jackson, *Classical Electrodynamics*, 3rd edition, (John Wiley & Sons, New York, 1998).
6. W.H. Barkas, W. Birnbaum, and F.M. Smith, Phys. Rev. **101**, 778 (1956).
7. J. D. Jackson, Phys. Rev. **D59**, 017301 (1999).
8. S.M. Seltzer and M.J. Berger, Int. J. of Applied Rad. **33**, 1189 (1982).
9. "Stopping Powers for Electrons and Positrons," ICRU Report No. 37 (1984).
10. `http://physics.nist.gov/PhysRefData/XrayMassCoef/tab1.html`.
11. H. Bichsel, Phys. Rev. **A46**, 5761 (1992).
12. W.H. Barkas and M.J. Berger, *Tables of Energy Losses and Ranges of Heavy Charged Particles*, NASA-SP-3013 (1964).
13. M. Agnello *et al.*, Phys. Rev. Lett. **74**, 371 (1995).
14. H.H. Andersen and J.F. Ziegler, *Hydrogen: Stopping Powers and Ranges in All Elements*. Vol. 3 of *The Stopping and Ranges of Ions in Matter* (Pergamon Press 1977).
15. J. Lindhard, Kgl. Danske Videnskab. Selskab, Mat.-Fys. Medd. **28**, No. 8 (1954).
16. J. Lindhard, M. Scharff, and H.E. Schiøtt, Kgl. Danske Videnskab. Selskab, Mat.-Fys. Medd. **33**, No. 14 (1963).
17. J.F. Ziegler, J.F. Biersac, and U. Littmark, *The Stopping and Range of Ions in Solids*, Pergamon Press 1985.
18. R.M. Sternheimer, Phys. Rev. **88**, 851 (1952).
19. R.M. Sternheimer and R.F. Peierls, Phys. Rev. **B3**, 3681 (1971).
20. A. Crispin and G.N. Fowler, Rev. Mod. Phys. **42**, 290 (1970).
21. R.M. Sternheimer, S.M. Seltzer, and M.J. Berger, "The Density Effect for the Ionization Loss of Charged Particles in Various Substances," Atomic Data and Nuclear Data Tables **30**, 261 (1984). Minor errors are corrected in Ref. 1. Chemical composition for the tabulated materials is given in Ref. 8.
22. For unit-charge projectiles, see E.A. Uehling, Ann. Rev. Nucl. Sci. **4**, 315 (1954). For highly charged projectiles, see J.A. Doggett and L.V. Spencer, Phys. Rev. **103**, 1597 (1956). A Lorentz transformation is needed to convert these center-of-mass data to knock-on energy spectra.
23. N.F. Mott and H.S.W. Massey, *The Theory of Atomic Collisions*, Oxford Press, London, 1965.
24. L.D. Landau, J. Exp. Phys. (USSR) **8**, 201 (1944).
25. H. Bichsel, Rev. Mod. Phys. **60**, 663 (1988).
26. H. Bichsel, Nuc. Inst. Meth. **6 B 52**, 136 (1990).
27. H. Bichsel, Ch. 87 in the Atomic, Molecular and Optical Physics Handbook, G.W.F. Drake, editor (Am. Inst. Phys. Press, Woodbury NY, 1996).
28. S.M. Seltzer and M.J. Berger, Int. J. of Applied Rad. **35**, 665 (1984). This paper corrects and extends the results of Ref. 8.

29. L.V. Spencer "Energy Dissipation by Fast Electrons," Nat'l Bureau of Standards Monograph No. 1 (1959).
30. "Average Energy Required to Produce an Ion Pair," ICRU Report No. 31 (1979).
31. N. Hadley *et al.*, "List of Poisoning Times for Materials," Lawrence Berkeley Lab Report TPC-LBL-79-8 (1981).
32. H.A. Bethe, Phys. Rev. **89**, 1256 (1953). A thorough review of multiple scattering is given by W.T. Scott, Rev. Mod. Phys. **35**, 231 (1963). However, the data of Shen *et al.*, (Phys. Rev. **D20**, 1584 (1979)) show that Bethe's simpler method of including atomic electron effects agrees better with experiment that does Scott's treatment. For a thorough discussion of simple formulae for single scatters and methods of compounding these into multiple-scattering formulae, see W.T. Scott, Rev. Mod. Phys. **35**, 231 (1963). For detailed summaries of formulae for computing single scatters, see J.W. Motz, H. Olsen, and H.W. Koch, Rev. Mod. Phys. **36**, 881 (1964).
33. V.L. Highland, Nucl. Instrum. Methods **129**, 497 (1975), and Nucl. Instrum. Methods **161**, 171 (1979).
34. G.R. Lynch and O.I Dahl, Nucl. Instrum. Methods **B58**, 6 (1991).
35. M. Wong *et al.*, Med. Phys. **17**, 163 (1990).
36. E. Segré, *Nuclei and Particles*, New York, Benjamin (1964) p. 65 ff.
37. Y.S. Tsai, Rev. Mod. Phys. **46**, 815 (1974).
38. H. Davies, H.A. Bethe, and L.C. Maximon, Phys. Rev. **93**, 788 (1954).
39. O.I. Dahl, private communication.
40. L.D. Landau and I.J. Pomeranchuk, Dokl. Akad. Nauk. SSSR **92**, 535 (1953); **92**, 735 (1953). These papers are available in English in L. Landau, *The Collected Papers of L.D. Landau*, Pergamon Press, 1965; A.B. Migdal, Phys. Rev. **103**, 1811 (1956).
41. S. Klein, Rev. Mod. Phys. **71**, 1501 (1999).
42. M. L. Ter-Mikaelian, SSSR **94**, 1033 (1954);
    M. L. Ter-Mikaelian, *High Energy Electromagnetic Processes in Condensed Media* (John Wiley & Sons, New York, 1972).
43. P. Anthony *et al.*, Phys. Rev. Lett. **76**, 3550 (1996).
44. H. W. Koch and J. W. Motz, Rev. Mod. Phys. **31**, 920 (1959).
45. M.J. Berger and S.M. Seltzer, "Tables of Energy Losses and Ranges of Electrons and Positrons," National Aeronautics and Space Administration Report NASA-SP-3012 (Washington DC 1964).
46. K. Hikasa *et al.*, *Review of Particle Properties*, Phys. Rev. **D46** (1992) S1.
47. J. W. Motz, H. A. Olsen, and H. W. Koch, Rev. Mod. Phys. **41**, 581 (1969).
48. P. Anthony *et al.*, Phys. Rev. Lett. **75**, 1949 (1995).
49. W.R. Nelson, H. Hirayama, and D.W.O. Rogers, "The EGS4 Code System," SLAC-265, Stanford Linear Accelerator Center (Dec. 1985).
50. *Experimental Techniques in High Energy Physics*, ed. by T. Ferbel (Addision-Wesley, Menlo Park CA 1987).
51. U. Amaldi, Phys. Scripta **23**, 409 (1981).
52. E. Longo and I. Sestili, Nucl. Instrum. Methods **128**, 283 (1975).
53. G. Grindhammer *et al.*, in *Proceedings of the Workshop on Calorimetry for the Supercollider*, Tuscaloosa, AL, March 13–17, 1989, edited by R. Donaldson and M.G.D. Gilchriese (World Scientific, Teaneck, NJ, 1989), p. 151.
54. W.R. Nelson, T.M. Jenkins, R.C. McCall, and J.K. Cobb, Phys. Rev. **149**, 201 (1966).
55. G. Bathow *et al.*, Nucl. Phys. **B20**, 592 (1970).
56. H.A. Bethe and W. Heitler, *Proc. Roy. Soc.* **A146**, 83 (1934);
    H.A. Bethe, *Proc. Cambridge Phil. Soc.* **30**, 542 (1934).
57. A.A. Petrukhin and V.V. Shestakov, Can. J. Phys. **46**, S377 (1968).
58. V.M. Galitskii and S.R. Kel'ner, Sov. Phys. JETP **25**, 948 (1967).
59. S.R. Kel'ner and Yu.D. Kotov, Sov. J. Nucl. Phys. **7**, 237 (1968).
60. R.P. Kokoulin and A.A. Petrukhin, in *Proceedings of the International Conference on Cosmic Rays*, Hobart, Australia, August 16–25, 1971, Vol. **4**, p. 2436.
61. A.I. Nikishov, Sov. J. Nucl. Phys. **27**, 677 (1978).
62. Y.M. Andreev *et al.*, Phys. Atom. Nucl. **57**, 2066 (1994).
63. L.B. Bezrukov and E.V. Bugaev, Sov. J. Nucl. Phys. **33**, 635 (1981).
64. N.V. Mokhov, "The MARS Code System User's Guide," Fermilab-FN-628 (1995);
    N. V. Mokhov, S. I. Striganov, A. Van Ginneken, S. G. Mashnik, A. J. Sierk, J.Ranft, in *Proc. of the Fourth Workshop on Simulating Accelerator Radiation Environments* (SARE-4), Knoxville, TN, September 14-16, 1998, pp. 87–99, Fermilab-Conf-98/379 (1998), nucl-th/9812038-v2-16-Dec-1998;
    N. V. Mokhov, in *Proc. of ICRS-9 International Conference on Radiation Shielding*, (Tsukuba,Ibaraki, Japan, 1999), J. Nucl. Sci. Tech., **1** (2000), pp. 167–171, Fermilab-Conf-00/066 (2000);
    `http://www-ap.fnal.gov/MARS/`.
65. P.H. Barrett, L.M. Bollinger, G. Cocconi, Y. Eisenberg, and K. Greisen, Rev. Mod. Phys. **24**, 133 (1952).
66. A. Van Ginneken, Nucl. Instrum. Methods **A251**, 21 (1986).
67. U. Becker *et al.*, Nucl. Instrum. Methods **A253**, 15 (1986).
68. J.J. Eastman and S.C. Loken, in *Proceedings of the Workshop on Experiments, Detectors, and Experimental Areas for the Supercollider*, Berkeley, CA, July 7–17, 1987, edited by R. Donaldson and M.G.D. Gilchriese (World Scientific, Singapore, 1988), p. 542.
69. *Methods of Experimental Physics*, L.C.L. Yuan and C.-S. Wu, editors, Academic Press, 1961, Vol. 5A, p. 163.
70. W.W.M. Allison and P.R.S. Wright, "The Physics of Charged Particle Identification: dE/dx, Cherenkov Radiation, and Transition Radiation," p. 371 in *Experimental Techniques in High Energy Physics*, T. Ferbel, editor, (Addison-Wesley 1987).
71. E.R. Hayes, R.A. Schluter, and A. Tamosaitis, "Index and Dispersion of Some Cherenkov Counter Gases," ANL-6916 (1964).
72. T. Ypsilantis, "Particle Identification at Hadron Colliders", CERN-EP/89-150 (1989), or ECFA 89-124, **2** 661 (1989).

28. PARTICLE DETECTORS

Revised 2003 (see the various sections for authors).

In this section we give various parameters for common detector components. The quoted numbers are usually based on typical devices, and should be regarded only as rough approximations for new designs. More detailed discussions of detectors and their underlying physics can be found in books by Ferbel [1], Grupen [2], Kleinknecht [3], Knoll [4], and Green [5]. In Table 28.1 are given typical spatial and temporal resolutions of common detectors.

Table 28.1: Typical spatial and temporal resolutions of common detectors. Revised September 2003 by R. Kadel (LBNL).

Detector Type	Accuracy (rms)	Resolution Time	Dead Time
Bubble chamber	10–150 μm	1 ms	50 ms[a]
Streamer chamber	300 μm	2 μs	100 ms
Proportional chamber	50–300 μm[b,c,d]	2 ns	200 ns
Drift chamber	50–300 μm	2 ns[e]	100 ns
Scintillator	—	100 ps/n[f]	10 ns
Emulsion	1 μm	—	—
Liquid Argon Drift [Ref. 6]	$\sim$175–450 μm	$\sim$ 200 ns	$\sim$ 2 μs
Gas Micro Strip [Ref. 7]	30–40 μm	$<$ 10 ns	—
Resistive Plate chamber [Ref. 8]	$\lesssim$ 10 μm	1–2 ns	—
Silicon strip	pitch/(3 to 7)[g]	*h*	*h*
Silicon pixel	2 μm[i]	*h*	*h*

[a] Multiple pulsing time.
[b] 300 μm is for 1 mm pitch.
[c] Delay line cathode readout can give $\pm$150 μm parallel to anode wire.
[d] wirespacing/$\sqrt{12}$.
[e] For two chambers.
[f] n = index of refraction.
[g] The highest resolution ("7") is obtained for small-pitch detectors ($\lesssim$25 μm) with pulse-height-weighted center finding.
[h] Limited by the readout electronics [9]. (Time resolution of $\leq$ 25 ns is planned for the ATLAS SCT.)
[i] Analog readout of 34 μm pitch, monolithic pixel detectors.

28.1. Organic scintillators

Revised September 2001 by K.F. Johnson (FSU).

Organic scintillators are broadly classed into three types, crystalline, liquid, and plastic, all of which utilize the ionization produced by charged particles (see the section on "Passage of particles through matter" (Sec. 27.2) of this *Review*) to generate optical photons, usually in the blue to green wavelength regions [10]. Plastic scintillators are by far the most widely used. Crystal organic scintillators are practically unused in high-energy physics.

Densities range from 1.03 to 1.20 g cm^{-3}. Typical photon yields are about 1 photon per 100 eV of energy deposit [11]. A one-cm-thick scintillator traversed by a minimum-ionizing particle will therefore yield $\approx 2 \times 10^4$ photons. The resulting photoelectron signal will depend on the collection and transport efficiency of the optical package and the quantum efficiency of the photodetector.

Plastic scintillators do not respond linearly to the ionization density. Very dense ionization columns emit less light than expected on the basis of dE/dx for minimum-ionizing particles. A widely used semi-empirical model by Birks posits that recombination and quenching effects between the excited molecules reduce the light yield [12]. These effects are more pronounced the greater the density of the excited molecules. Birks' formula is

$$\frac{d\mathscr{L}}{dx} = \mathscr{L}_0 \frac{dE/dx}{1 + k_B\, dE/dx} ,$$

where $\mathscr{L}$ is the luminescence, $\mathscr{L}_0$ is the luminescence at low specific ionization density, and k_B is Birks' constant, which must be determined for each scintillator by measurement.

Decay times are in the ns range; rise times are much faster. The combination of high light yield and fast response time allows the possibility of sub-ns timing resolution [13]. The fraction of light emitted during the decay "tail" can depend on the exciting particle. This allows pulse shape discrimination as a technique to carry out particle identification. Because of the hydrogen content (carbon to hydrogen ratio $\approx$ 1) plastic scintillator is sensitive to proton recoils from neutrons. Ease of fabrication into desired shapes and low cost has made plastic scintillators a common detector component. Recently, plastic scintillators in the form of scintillating fibers have found widespread use in tracking and calorimetry [14].

28.1.1. *Scintillation mechanism* :

Scintillation: A charged particle traversing matter leaves behind it a wake of excited molecules. Certain types of molecules, however, will release a small fraction ($\approx$ 3%) of this energy as optical photons. This process, scintillation, is especially marked in those organic substances which contain aromatic rings, such as polystyrene (PS) and polyvinyltoluene (PVT). Liquids which scintillate include toluene and xylene.

Fluorescence: In fluorescence, the initial excitation takes place via the absorption of a photon, and de-excitation by emission of a longer wavelength photon. Fluors are used as "waveshifters" to shift scintillation light to a more convenient wavelength. Occurring in complex molecules, the absorption and emission are spread out over a wide band of photon energies, and have some overlap, that is, there is some fraction of the emitted light which can be re-absorbed [15]. This "self-absorption" is undesirable for detector applications because it causes a shortened attenuation length. The wavelength difference between the major absorption and emission peaks is called the Stokes' shift. It is usually the case that the greater the Stokes' shift, the smaller the self absorption—thus, a large Stokes' shift is a desirable property for a fluor (aka the "Better red than dead" strategy).

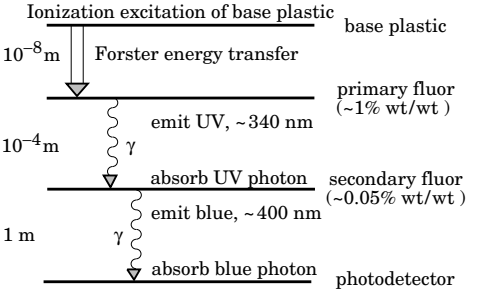

Figure 28.1: Cartoon of scintillation "ladder" depicting the operating mechanism of plastic scintillator. Approximate fluor concentrations and energy transfer distances for the separate sub-processes are shown.

Scintillators: The plastic scintillators used in high-energy physics are binary or ternary solutions of selected fluors in a plastic base containing aromatic rings. (See the appendix in Ref. 16 for a comprehensive list of components.) Virtually all plastic scintillators contain as a base either PVT or PS. PVT-based scintillator can be up to 50% brighter. The fluors must satisfy additional conditions besides being fluorescent. They must be sufficiently stable, soluble, chemically inert, fast, radiation tolerant, and efficient.

Ionization in the plastic base produces UV photons with short attenuation length (several mm). Longer attenuation lengths are obtained by dissolving a "primary" fluor in high concentration (1% by weight) into the base, which is selected to efficiently re-radiate absorbed energy at wavelengths where the base is more transparent.

The primary fluor has a second important function. The decay time of the scintillator base material can be quite long—in pure polystyrene it is 16 ns, for example. The addition of the primary fluor in high concentration can shorten the decay time by an order of magnitude and increase the total light yield. At the concentrations used (1% and greater), the average distance between a fluor molecule and an excited base unit is around 100 Å, much less than a wavelength of light. At these distances the predominant mode of energy transfer from base to fluor is not the radiation of a photon, but a resonant dipole-dipole interaction, first described by Foerster, which strongly couples the base and fluor [17]. The strong coupling sharply increases the speed and the light yield of the plastic scintillators.

Unfortunately, a fluor which fulfills other requirements is usually not completely adequate with respect to emission wavelength or attenuation length, so it is necessary to add yet another waveshifter (the "secondary" fluor), at fractional percent levels, and occasionally a third (not shown in Fig. 28.1).

External wavelength shifters: Light emitted from a plastic scintillator may be absorbed in a (nonscintillating) base doped with a wave-shifting fluor. Such wavelength shifters are widely used to aid light collection in complex geometries. The wavelength shifter must be insensitive to ionizing radiation and Cherenkov light. A typical wavelength shifter uses an acrylic base because of its good optical qualities, a single fluor to shift the light emerging from the plastic scintillator to the blue-green, and contains ultra-violet absorbing additives to deaden response to Cherenkov light.

28.1.2. ***Caveats and cautions***: Plastic scintillators are reliable, robust, and convenient. However, they possess quirks to which the experimenter must be alert.

Aging and Handling: Plastic scintillators are subject to aging which diminishes the light yield. Exposure to solvent vapors, high temperatures, mechanical flexing, irradiation, or rough handling will aggravate the process. A particularly fragile region is the surface which can 'craze"—develop microcracks—which rapidly destroy the capability of plastic scintillators to transmit light by total internal reflection. Crazing is particularly likely where oils, solvents, or *fingerprints* have contacted the surface.

Attenuation length: The Stokes' shift is not the only factor determining attenuation length. Others are the concentration of fluors (the higher the concentration of a fluor, the greater will be its self-absorption); the optical clarity and uniformity of the bulk material; the quality of the surface; and absorption by additives, such as stabilizers, which may be present.

Afterglow: Plastic scintillators have a long-lived luminescence which does not follow a simple exponential decay. Intensities at the 10^{-4} level of the initial fluorescence can persist for hundreds of ns [10,18].

Atmospheric quenching: Plastic scintillators will decrease their light yield with increasing partial pressure of oxygen. This can be a 10% effect in an artificial atmosphere [19]. It is not excluded that other gases may have similar quenching effects.

Magnetic field: The light yield of plastic scintillators may be changed by a magnetic field. The effect is very nonlinear and apparently not all types of plastic scintillators are so affected. Increases of $\approx 3\%$ at 0.45 T have been reported [20]. Data are sketchy and mechanisms are not understood.

Radiation damage: Irradiation of plastic scintillators creates color centers which absorb light more strongly in the UV and blue than at longer wavelengths. This poorly understood effect appears as a reduction both of light yield and attenuation length. Radiation damage depends not only on the integrated dose, but on the dose rate, atmosphere, and temperature, before, during and after irradiation, as well as the materials properties of the base such as glass transition temperature, polymer chain length, *etc.* Annealing also occurs, accelerated by the diffusion of atmospheric oxygen and elevated temperatures. The phenomena are complex, unpredictable, and not well understood [21]. Since color centers are less intrusive at longer wavelengths, the most reliable method of mitigating radiation damage is to shift emissions at every step to the longest practical wavelengths, *e.g.*, utilize fluors with large Stokes' shifts (aka the "Better red than dead" strategy).

28.1.3. ***Scintillating and wavelength-shifting fibers***:

The clad optical fiber is an incarnation of scintillator and wavelength shifter (WLS) which is particularly useful [22]. Since the initial demonstration of the scintillating fiber (SCIFI) calorimeter [23], SCIFI techniques have become mainstream. SCIFI calorimeters are found, for example, in the $g-2$ experiment at Brookhaven [24] and at KLOE; SCIFI trackers are found at CHORUS and DØ ; WLS readout is used in both ATLAS and CMS hadron calorimeters [25].

SCIFI calorimeters are fast, dense, radiation hard, and can have leadglass-like resolution. SCIFI trackers can handle high rates and are radiation tolerant, but the low photon yield at the end of a long fiber (see below) forces the use of very sophisticated photodetectors such as VLPC's, such as are used in DØ . WLS scintillator readout of a calorimeter allows a very high level of hermeticity since the solid angle blocked by the fiber on its way to the photodetector is very small. The sensitive region of scintillating fibers can be controlled by splicing them onto clear (non-scintillating/non-WLS) fibers.

A typical configuration would be fibers with a core of polystyrene-based scintillator or WLS (index of refraction $n = 1.59$), surrounded by a cladding of PMMA ($n = 1.49$) a few microns thick, or, for added light capture, with another cladding of fluorinated PMMA with $n = 1.42$, for an overall diameter of 0.5 to 1 mm. The fiber is drawn from a boule and great care is taken during production to ensure that the intersurface between the core and the cladding has the highest possible uniformity and quality, so that the signal transmission via total internal reflection has a low loss. The fraction of generated light which is transported down the optical pipe is denoted the capture fraction and is about 6% for the single-clad fiber and 10% for the double-clad fiber.

The number of photons from the fiber available at the photodetector is always smaller than desired, and increasing the light yield has proven difficult [26]. A minimum-ionizing particle traversing a high-quality 1 mm diameter fiber perpendicular to its axis will produce fewer than 2000 photons, of which about 200 are captured. Attenuation eliminates about 95% of these photons. DØ uses 0.775 mm diameter scintillating fibers in the tracker and obtains 9 photoelectrons with the VLPC reaching 85% quantum efficiency.

A scintillating or WLS fiber is often characterized by its "attenuation length," over which the signal is attenuated to $1/e$ of its original value. Many factors determine the attenuation length, including the importance of re-absorption of emitted photons by the polymer base or dissolved fluors, the level of crystallinity of the base polymer, and the quality of the total internal reflection boundary. Attenuation lengths of several meters are obtained by high quality fibers. However, it should be understood that the attenuation length is not necessarily a measure of fiber quality. Among other things, it is not constant with distance from the excitation source and it is wavelength dependent. So-called "cladding light" causes some of the distance dependence [27], but not all. The wavelength dependence is usually related to the higher re-absorption of shorter wavelength photons—once absorbed, re-emitted isotropically and lost with 90% probability—and to the lower absorption of longer wavelengths by polystyrene. Experimenters should be aware that measurements of attenuation length by a phototube with a bialkali photocathode, whose quantum efficiency drops below 10% at 480 nm, should not be naïvely compared to measurements utilizing a silicon photodiode, whose quantum efficiency is still rising at 600 nm.

28.2. Inorganic scintillators:

Revised September 2003 by C.L. Woody (BNL). and R.-Y. Zhu (California Inst. of Technology).

Inorganic crystals form a class of scintillating materials with much higher densities than organic plastic scintillators (typically $\sim$ 4–8 g/cm^3) with a variety of different properties for use as scintillation detectors. Due to their high density and high effective atomic number, they can be used in applications where high stopping power or

a high conversion efficiency for electrons or photons is required. These include total absorption electromagnetic calorimeters (see Sec. 28.10.1), which consist of a totally active absorber (as opposed to a sampling calorimeter), as well as serving as gamma ray detectors over a wide range of energies. Many of these crystals also have very high light output, and can therefore provide excellent energy resolution down to very low energies ($\sim$ few hundred keV).

Some crystals are intrinsic scintillators in which the luminescence is produced by a part of the crystal lattice itself. However, other crystals require the addition of a dopant, typically fluorescent ions such as thallium (Tl) or cerium (Ce) which is responsible for producing the scintillation light. However, in both cases, the scintillation mechanism is the same. Energy is deposited in the crystal by ionization, either directly by charged particles, or by the conversion of photons into electrons or positrons which subsequently produce ionization. This energy is transfered to the luminescent centers which then radiate scintillation photons. The efficiency η for the conversion of energy deposit in the crystal to scintillation light can be expressed by the relation [28]

$$\eta = \beta \cdot S \cdot Q \ . \tag{28.1}$$

where β is the efficiency of the energy conversion process, S is the efficiency of energy transfer to the luminescent center, and Q is the quantum efficiency of the luminescent center. The value of η ranges between 0.1 and $\sim$ 1 depending on the crystal, and is the main factor in determining the intrinsic light output of the scintillator. In addition, the scintillation decay time is primarily determined by the energy transfer and emission process. The decay time of the scintillator is mainly dominated by the decay time of the luminescent center. For example, in the case of thallium doped sodium iodide (NaI(Tl)), the value of η is $\sim$ 0.5, which results in a light output $\sim$ 40,000 photons per MeV of energy deposit. This high light output is largely due to the high quantum efficiency of the thallium ion (Q $\sim$ 1), but the decay time is rather slow ($\tau \sim 250$ ns).

Table 28.2 lists the basic properties of some commonly used inorganic crystal scintillators. NaI(Tl) is one of the most common and widely used scintillators, with an emission that is well matched to a bialkali photomultiplier tube, but it is highly hygroscopic and difficult to work with, and has a rather low density. CsI(Tl) has high light yield, an emission that is well matched to solid state photodiodes, and is mechanically robust (high plasticity and resistance to cracking). However, it needs careful surface treatment and is slightly hygroscopic. Compared with CsI(Tl), pure CsI has identical mechanical properties, but faster emission at shorter wavelengths and light output approximately an order of magnitude lower. BaF_2 has a fast component with a sub-nanosecond decay time, and is the fastest known scintillator. However, it also has a slow component with a much longer decay time ($\sim$ 630 ns). Bismuth gemanate ($Bi_4Ge_3O_{12}$ or BGO) has a very high density, and consequently a short radiation length X_0 and Molière radius R_M. BGO's emission is well-matched to the spectral sensitivity of photodiodes, and it is easy to handle and not hygroscopic. Lead tungstate ($PbWO_4$ or PWO) has a very high density, with a very short X_0 and R_M, but its intrinsic light yield is rather low. Both cerium doped lutetium oxyorthosilicate (Lu_2SiO_5:Ce, or LSO:Ce) [29] and cerium doped gadolinium orthosilicate (Gd_2SiO_5:Ce, or GSO:Ce) [30] are dense crystal scintillators which have a high light yield and a fast decay time.

Beside the crystals listed in Table 28.2, a number of new crystals are being developed that may have potenial applications in high energy or nuclear physics. Of particular interest is the family of yttrium and lutetium perovskites, which include YAP ($YAlO_3$:Ce) and LuAP ($LuAlO_3$:Ce) and their mixed compositions. These have been shown to be linear over a large energy range [31], and have the potential for providing extremely good intrinsic energy resolution. In addition, other fluoride crystals such as CeF_3 have been shown to provide excellent energy resolution in calorimeter applications.

Table 28.2 gives the light output of other crystals relative to NaI(Tl) as measured with a bialkalai photomultiplier tube. However, the useful signal produced by a scintillator is usually quoted in terms of the number of photoelectrons per MeV produced by a given photodetector. The relationship between the number of photons/MeV produced and photoelectrons/MeV detected involves the factors for the light collection efficiency L and the quantum efficiency QE of the photodetector:

$$N_{\text{p.e.}}/\text{MeV} = L \cdot QE \cdot N_\gamma/\text{MeV} \tag{28.2}$$

L includes the transmission of scintillation light within the crystal (*i.e.*, the bulk attenuation length of the material), reflections and scattering from the surfaces, and the size and shape of the crystal. These factors can vary considerably depending on the sample, but can be in the range of $\sim$50–60%. However, the internal light transmission depends on the intrinsic properties of the material, as well as the number and type of impurites and defects that can produce internal absorption within the crystal, and can be highly affected by factors such as radiation damage, as discussed below.

The quantum efficiency depends on the type of photodetector used to detect the scintillation light, which is typically $\sim$15–20% for photomultiplier tubes and $\sim$70% for silicon photodiodes for visible wavelengths. The quantum efficiency of the detector is usually highly wavelength dependent and should be matched to the particular crystal of interest to give the highest quantum yield at the wavelength corresponding to the peak of the scintillation emission. The comparison of the light output given in Table 28.2 is for a standard photomultiplier tube with a bialkali photocathode. Results with different photodetectors can be significantly different. For example, the response of CsI(Tl) relative to NaI(Tl) with a silicon photodiode would be 140 rather than 45 due to its higher quantum efficiency at longer wavelengths. For scintillators which emit in the UV, a detector with a quartz window should be used.

One important issue related to the application of a crystal scintillator is its radiation hardness. Stability of its light output, or the ability to track and monitor the variation of its light output in a radiation environment, is required for high resolution and precision calibration [32]. All known crystal scintillators suffer from radiation damage. A common damage phenomenon is the appearance of radiation induced absorption caused by the formation of impurities or point defect related color centers. This radiation induced absorption reduces the light attenuation length in the crystal, and hence its light output. For crystals with high defect density, a severe reduction of light attenuation length may lead to a distortion of the light response uniformity, leading to a degradation of energy resolution. Additional radiation damage effects may include a reduced intrinsic scintillation light yield (damage to the luminescent centers) and an increased phosphorescence (afterglow). For crystals to be used in the construction a high precision calorimeter in a radiation environment, its scintillation mechanism must not be damaged and its light attenuation length in the expected radiation environment must be long enough so that its light response uniformity, and thus its energy resolution, does not change [33].

Most of the crystals listed in Table 28.2 have been used in high energy or nuclear physics experiments when the ultimate energy resolution for electrons and photons is desired. Examples are the Crystal Ball NaI(Tl) calorimeter at SPEAR, the L3 BGO calorimeter at LEP, the CLEO CsI(Tl) calorimeter at CESR, the KTeV CsI calorimeter at the Tevatron, and the BaBar and BELLE CsI(Tl) calorimeters at PEP-II and KEK. Because of its high density and low cost, PWO calorimeters are now being constructed by CMS and ALICE at LHC, by CLAS and PrimEx at CEBAF, and by BTeV at the Tevatron.

28.3. Cherenkov detectors

Written September 2003 by B.N. Ratcliff (SLAC).

Although devices using Cherenkov radiation are often thought of as particle identification (PID) detectors, in practice, they are widely used over a much broader range of applications; including (1) fast particle counters; (2) hadronic particle identification; and (3) tracking detectors performing complete event reconstruction. A few examples of specific applications from each category include; (1) the polarization detector of the SLD [34]; (2) the hadronic PID detectors at the B factory detectors (DIRC in BaBar [8] and the aerogel threshold Cherenkov in Belle [35]); and (3) large water Cherenkov counters

Table 28.2: Properties of several inorganic crystal scintillators. Most of the notation is defined in Sec. 6 of this *Review*.

Parameter:	ρ	MP	X_0	R_M	dE/dx	λ_I	$\tau_{\rm decay}$	$\lambda_{\rm max}$	n^*	Relative output†	Hygro-scopic?	d(LY)/dT
Units:	g/cm^3	°C	cm	cm	MeV/cm	cm	ns	nm				%/°C‡
NaI(Tl)	3.67	651	2.59	4.8	4.8	41.4	230	410	1.85	100	yes	$\sim$0
BGO	7.13	1050	1.12	2.3	9.0	21.8	300	480	2.15	9	no	-1.6
BaF_2	4.89	1280	2.06	3.4	6.6	29.9	630^s	300^s	1.50	21^s	no	-2^s
							0.9^f	220^f		2.7^f		$\sim 0^f$
CsI(Tl)	4.51	621	1.85	3.5	5.6	37.0	1300	560	1.79	45	slight	0.3
CsI(pure)	4.51	621	1.85	3.5	5.6	37.0	35^s	420^s	1.95	5.6^s	slight	-0.6
							6^f	310^f		2.3^f		
$PbWO_4$	8.3	1123	0.9	2.0	10.2	18	50^s	560^s	2.20	0.1^s	no	-1.9
							10^f	420^f			0.6^f	
LSO(Ce)	7.40	2070	1.14	2.3	9.6	21	40	420	1.82	75	no	-0.3
GSO(Ce)	6.71	1950	1.37	2.4	8.9	22	600^s	430	1.85	3^s	no	-0.1
							56^f			30^f		

* Refractive index at the wavelength of the emission maximum.
† Relative light yield measured with a bi-alkali cathode PMT.
‡ Variation of light yield with temperature evalutated at room temperature.
f = fast component, s = slow component

such as Super-Kamiokande [36]. Cherenkov counters contain two main elements; (1) a radiator through which the charged particle passes, and (2) a photodetector. As Cherenkov radiation is a weak source of photons, light collection and detection must be as efficient as possible. The presence of the refractive index n and the path length of the particle in the radiator in the Cherenkov relations allows tuning these quantities for a particular experimental application.

Cherenkov detectors utilize one or more of the properties of Cherenkov radiation discussed in the Passages of Particles through Matter section (Sec. 27 of this *Review*): the prompt emission of a light pulse; the existence of a velocity threshold for radiation; and the dependence of the Cherenkov cone half-angle θ_c and the number of emitted photons on the velocity of the particle.

The number of photoelectrons ($N_{\rm p.e.}$) detected in a given device is

$$N_{\rm p.e.} = L\frac{\alpha^2 z^2}{r_e\, m_e c^2}\int \epsilon(E)\, \sin^2\theta_c(E) dE\ , \qquad (28.3)$$

where L is the path length in the radiator, ϵ(E) is the efficiency for collecting the Cherenkov light and transducing it in photoelectrons, and $\alpha^2/(r_e\, m_e c^2) = 370\ {\rm cm}^{-1}{\rm eV}^{-1}$.

The quantities ϵ and θ_c are functions of the photon energy E. However, since the typical energy dependent variation of the index of refraction is modest, a quantity called the *Cherenkov detector quality factor* N_0 can be defined as

$$N_0 = \frac{\alpha^2 z^2}{r_e\, m_e c^2}\int \epsilon\, dE\ , \qquad (28.4)$$

so that

$$N_{\rm p.e.} \approx L N_0 \langle \sin^2\theta_c\rangle\ . \qquad (28.5)$$

We take $z = 1$, the usual case in high-energy physics, in the following discussion.

This definition of the quality factor N_0 is not universal, nor, indeed, very useful for situations where the geometrical photon collection efficiency ($\epsilon_{\rm coll}$) varies substantially for different tracks. In this case, separate factors for photon collection and detection ($\epsilon_{\rm det}$), so that $\epsilon = \epsilon_{\rm coll}\epsilon_{\rm det}$, are sometimes included on the right hand side of the equation. A typical value of N_0 for a photomultiplier (PMT) detection system working in the visible and near UV, and collecting most of the Cherenkov light, is about 100 cm^{-1}. Practical counters, utilizing a variety of different photodetectors, have values ranging between about 30 and 180 cm^{-1}.

Radiators can be chosen from a variety of transparent materials (Sec. 27 of this *Review* and Table 6.1). In addition to refractive index, the choice requires consideration of factors such as material density, radiation length, transmission bandwidth, absorption length, chromatic dispersion, optical workability (for solids), availability, and cost. Long radiator lengths are required to obtain sufficient numbers of photons when the momenta of the particle species to be separated are high. Recently, the gap in refractive index that has traditionally existed between gases and liquid or solid materials has been partially closed with transparent *silica aerogels* with indices that range between about 1.007 and 1.13.

Cherenkov counters may be classified as either *imaging* or *threshold* types, depending on whether they do or do not make use of Cherenkov angle (θ_c) information. Imaging counters may be used to track particles as well as identify them.

28.3.1. ***Threshold counters:***: Threshold Cherenkov detectors [37], in their simplest form, make a yes/no decision based on whether the particle is above or below the Cherenkov threshold velocity $\beta_t = 1/n$. A straightforward enhancement of such detectors uses the number of observed photoelectrons (or a calibrated pulse height) to discriminate between species or to set probabilities for each particle species [38]. This strategy can increase the momentum range of particle separation by a modest amount (to a momentum some 20% above the threshold momentum of the heavier particle in a typical case).

Careful designs give $\langle\epsilon_{\rm coll}\rangle \gtrsim 90\%$. For a photomultiplier with a typical bialkali cathode, $\int \epsilon_{\rm det} dE \approx 0.27$, so that

$$N_{\rm p.e.}/L \approx 90\ {\rm cm}^{-1}\langle\sin^2\theta_c\rangle \quad (i.e.,\ N_0 = 90\ {\rm cm}^{-1})\ . \qquad (28.6)$$

Suppose, for example, that n is chosen so that the threshold for species a is p_t; that is, at this momentum species a has velocity $\beta_a = 1/n$. A second, lighter, species b with the same momentum has velocity β_b, so $\cos\theta_c = \beta_a/\beta_b$, and

$$N_{\rm p.e.}\, L \approx 90\ {\rm cm}^{-1}\,\frac{m_a^2 - m_b^2}{p_t^2 + m_a^2}\ . \qquad (28.7)$$

For K/π separation at $p = p_t = 1(5)$ GeV/c, $N_{\rm p.e.}/L \approx 16(0.8)$ cm^{-1} for π's and (by design) 0 for K's.

For limited path lengths $N_{\rm p.e.}$ can be small, and a minimum number is required to trigger external electronics. The overall efficiency of the device is controlled by Poisson fluctuations, which can be especially critical for separation of species where one particle type is dominant. The effective number of photoelectrons is often less than the average

number calculated above due to additional equivalent noise from the photodetector. It is common to design for at least 10 photoelectrons for the high velocity particle in order to obtain a robust counter. As rejection of the particle that is below threshold depends on *not* seeing a signal, electronic and other background noise can be important. Physics sources of light production for the below threshold particle, such as decay of the above threshold particle or the production of delta rays in the radiator, often limit the separation attainable, and need to be carefully considered. Well designed, modern multi-channel counters, such as the ACC at Belle [35], can attain good particle separation performance over a substantial momentum range for essentially the full solid angle of the spectrometer.

28.3.2. ***Imaging counters***: The most powerful use of the information available from the Cherenkov process comes from measuring the ring-correlated angles of emission of the individual Cherenkov photons. Since low-energy photon detectors can measure only the position (and, perhaps, a precise detection time) of the individual Cherenkov photons (not the angles directly), the photons must be "imaged" onto a detector so that their angles can be derived [39]. In most cases the optics map the Cherenkov cone onto (a portion of) a distorted circle at the photodetector. Though this imaging process is directly analogous to the familiar imaging techniques used in telescopes and other optical instruments, there is a somewhat bewildering variety of methods used in a wide variety of counter types with different names. Some of the imaging methods used include (1) focusing by a lens; (2) proximity focusing (i.e., focusing by limiting the emission region of the radiation); and (3) focusing through an aperture (a pinhole). In addition, the prompt Cherenkov emission coupled with the speed of modern photon detectors allows the use of time imaging, a method which is used much less frequently in conventional imaging technology. Finally, full tracking (and event reconstruction) can be performed in large water counters by combining the individual space position and time of each photon together with the constraint that Cherenkov photons are emitted from each track at a constant polar angle.

In a simple model of an imaging PID counter, the fractional error on the particle velocity (δ_β) is given by

$$\delta_\beta = \frac{\sigma_\beta}{\beta} = \tan\theta_c \sigma(\theta_c) \quad , \tag{28.8}$$

where

$$\sigma(\theta_c) = \frac{\langle\sigma(\theta_i)\rangle}{\sqrt{N_{\rm p.e.}}} \oplus C \ , \tag{28.9}$$

where $\langle\sigma(\theta_i)\rangle$ is the average single photoelectron resolution, as defined by the optics, detector resolution and the intrinsic chromaticity spread of the radiator index of refraction averaged over the photon detection bandwidth. C combines a number of other contributions to resolution including,(1) correlated terms such as tracking, alignment, and multiple scattering, (2) hit ambiguities, (3) background hits from random sources, and (4) hits coming from other tracks. In many practical cases, the resolution is limited by these effects.

For a $\beta \approx 1$ particle of momentum (p) well above threshold entering a radiator with index of refraction (n), the number of σ separation (N_σ) between particles of mass m_1 and m_2 is approximately

$$N_\sigma \approx \frac{|m_1^2 - m_2^2|}{2p^2\sigma(\theta_c)\sqrt{n^2-1}} \, . \tag{28.10}$$

In practical counters, the angular resolution term $\sigma(\theta_c)$ varies between about 0.1 and 5 mrad depending on the size, radiator, and photodetector type of the particular counter. The range of momenta over which a particular counter can separate particle species extends from the point at which the number of photons emitted becomes sufficient for the counter to operate efficiently as a threshold device ($\sim$20% above the threshold for the lighter species) to the value in the imaging region given by the equation above. For example, for $\sigma(\theta_c) = 2$mrad, a fused silica radiator($n = 1.474$), or a flourocarbon gas radiator (C_5F_{12}, $n = 1.0017$), would separate π/K's from the threshold region starting around 0.15(3) GeV/c through the imaging region up to about 4.2(18) GeV/c at better than 3σ.

Many different imaging counters have been built during the last several decades [42]. Among the earliest examples of this class of counters are the very limited acceptance Differential Cherenkov detectors, designed for particle selection in high momentum beam lines. These devices use optical focusing and/or geometrical masking to select particles having velocities in a specified region. With careful design, a velocity resolution of $\sigma_\beta/\beta \approx 10^{-4}$–$10^{-5}$ can be obtained [37].

Practical multi-track Ring-Imaging Cherenkov detectors (generically called RICH counters) are a more recent development. They have been built in small-aperture and 4π geometries both as PID counters and as stand-alone detectors with complete tracking and event reconstruction as discussed more fully below. PID RICH counters are sometimes further classified by 'generations' that differ based on performance, design, and photodetection techniques.

A typical example of a first generation RICH used at the Z factory e^+e^- colliders [40,41] has both liquid (C_6F_{14}, $n = 1.276$) and gas (C_5F_{12}, $n = 1.0017$) radiators, the former being proximity imaged using the small radiator thickness while the latter use mirrors. The phototransducers are a TPC/wire-chamber combination having charge division or pads. They are made sensitive to photons by doping the TPC gas (usually, ethane/methane) with $\sim 0.05\%$ TMAE (tetrakis(dimethylamino)ethylene). Great attention to detail is required, (1) to avoid absorbing the UV photons to which TMAE is sensitive, (2) to avoid absorbing the single photoelectrons as they drift in the long TPC, and (3) to keep the chemically active TMAE vapor from interacting with materials in the system. In spite of their unforgiving operational characteristics, these counters attained good $e/\pi/K/p$ separation over wide momentum ranges during several years of operation. In particular, their π/K separation range extends over momenta from about 0.25 to 20 GeV/c.

Second and third generation counters [42] generally must operate at much higher particle rates than the first generation detectors, and utilize different photon detection bandwidths, with higher readout channel counts, and faster, more forgiving photon detection technology than the TMAE doped TPCs just described. Radiator choices have broadened to include materials such as lithium flouride, fused silica, and aerogel. Vacuum based photodetection systems (*e.g.*, photomultiplier tubes (PMT) or hybrid photodiodes (HPD)) have become increasingly common. They handle very high rates, can be used in either single or multi anode versions, and allow a wide choice of radiators. Other fast detection systems that use solid cesium iodide (CSI) photocathodes or triethylamine (TEA) doping in proportional chambers are useful with certain radiator types and geometries.

A DIRC (Detector of Internally Reflected Cherenkov light) is a third generation subtype of a RICH first used in the BaBar detector [8]. It "inverts" the usual principle for use of light from the radiator of a RICH by collecting and imaging the total internally reflected light, rather than the transmitted light. A DIRC utilizes the optical material of the radiator in two ways, simultaneously; first as a Cherenkov radiator, and second, as a light pipe for the Cherenkov light trapped in the radiator by total internal reflection. The DIRC makes use of the fact that the magnitudes of angles are preserved during reflection from a flat surface. This fact, coupled with the high reflection coefficients of the total internal reflection process (> 0.9995 for higly polished SiO_2), and the long attenuation length for photons in high purity fused silica, allows the photons of the ring image to be transported to a detector outside the path of the particle where they may be imaged. The BaBar DIRC uses 144 fused silica radiator bars ($1.7 \times 3.5 \times 490$ cm) with the light being focused onto 11 000 conventional PMT's located about 120 cm from the end of the bars by the "pinhole" of the bar end. DIRC performance can be understood using the formula for (N_σ) discussed above. Typically, $N_{\rm p.e.}$ is rather large (between 15 and 60) and the Cherenkov polar angle is measured to about 2.5 mrad. The momentum range with good π/K separation extends up to about 4 GeV/c, matching the B decay momentum spectrum observed in BaBar.

28.4. Cherenkov tracking calorimeters

Written August 2003 by D. Casper (UC Irvine).

In addition to the specialized applications described in the previous section, Cherenkov radiation is also exploited in large, ring-imaging detectors with masses measured in kilotons or greater. Such devices are not subdetector components, but complete experiments with triggering, tracking, vertexing, particle identification and calorimetric capabilities, where the large mass of the transparent dielectric medium serves as an active target for neutrino interactions (or their secondary muons) and rare processes like nucleon decay.

For volumes of this scale, absorption and scattering of Cherenkov light are non-negligible, and a wavelength-dependent factor $e^{-d/L(\lambda)}$ (where d is the distance from emission to the sensor and $L(\lambda)$ is the attenuation length of the medium) must be included in the integral of Eq. (28.3) for the photoelectron yield. The choice of medium is therefore constrained by the refractive index and transparency in the region of photodetector sensitivity; highly-purified water is an inexpensive and effective choice; sea-water, mineral oil, polar ice, and D_2O are also used. Photo-multiplier tubes (PMTs) on either a volume or surface lattice measure the time of arrival and intensity of Cherenkov radiation. Hemispherical PMTs are favored for the widest angular acceptance, and sometimes mounted with reflectors or wavelength-shifting plates to increase the effective photosensitive area. Gains and calibration curves are measured with pulsed laser signals transmitted to each PMT individually via optical fiber or applied to the detector as a whole through one or more diffusing balls.

Volume instrumentation [43] is only cost-effective at low densities, with a spacing comparable to the attenuation (absorption and scattering) length of Cherenkov light in the medium (15–40 m for Antarctic ice and ∼45 m in the deep ocean). PMTs are deployed in vertical strings as modular units which include pressure housings, front-end electronics and calibration hardware. The effective photocathode coverage of such arrays is less than 1% but still adequate (using timing information and the Cherenkov angular constraint) to reconstruct the direction of TeV muons to 1° or better. The size of such "neutrino telescopes" is limited only by cost once the technical challenges of deployment, power, signal extraction and calibration in an inaccessible and inhospitable environment are addressed; arrays up to $(1\ \mathrm{km})^3$ in size are under study or development.

Surface instrumentation [44] allows the target volume to be viewed with higher photocathode density by a number of PMTs which scales like $(\mathrm{volume})^{2/3}$. To improve hermeticity and shielding, and to ensure that an outward-going particle's Cherenkov cone illuminates sufficient PMTs for reconstruction, a software-defined fiducial volume begins some distance (∼ 2 m) inside the photosensor surface. Events originating within the fiducial volume are classified as *fully-contained* if no particles exit the inner detector, or *partially-contained* otherwise. An outer (veto) detector, optically separated from the inner volume and instrumented at reduced density, greatly assists in making this determination and also simplifies the selection of contained events. The maximum size of a pure surface array is limited by the attenuation length (∼ 100 m has been achieved for large volumes using reverse-osmosis water purification), pressure tolerance of the PMTs (< 80 meters of water, without pressure housings) and structural integrity of the enclosing cavity, if underground. In practice, these limitations can be overcome by a segmented design involving multiple modules of the nominal maximum size; megaton-scale devices are under study.

Cherenkov detectors are excellent electromagnetic calorimeters, and the number of Cherenkov photons *produced* by an e/γ is nearly proportional to its kinetic energy. For massive particles, the number of photons produced is also related to the energy, but not linearly. For any type of particle, the *visible energy* E_{vis} is defined as the energy of an electron which would produce the same number of Cherenkov photons. The number of photoelectrons *collected* depends on a detector-specific scale factor, with event-by-event corrections for geometry and attenuation. For typical PMTs, in water $N_{\mathrm{p.e.}} \approx 15\,\xi\,E_{\mathrm{vis}}(\mathrm{MeV})$, where ξ is the effective fractional photosensor coverage; for other materials, the photoelectron yield scales with the ratio of $\sin^2\theta_c$ over density. At solar neutrino energies, the visible energy resolution ($\sim 30\%/\sqrt{\xi\,E_{\mathrm{vis}}(\mathrm{MeV})}$) is about 20% worse than photoelectron counting statistics would imply. For higher energies, multi-photoelectron hits are likely and the charge collected by each PMT (rather the number of PMTs firing) must be used; this degrades the energy resolution to approximately $2\%/\sqrt{\xi\,E_{\mathrm{vis}}(\mathrm{GeV})}$. In addition, the absolute energy scale must be determined with sources of known energy. Using an electron LINAC and/or nuclear sources, 0.5–1.5% has been achieved at solar neutrino energies; for higher energies, cosmic-ray muons, Michel electrons and π^0 from neutrino interactions allow ∼ 3% absolute energy calibration.

A trigger can be formed by the coincidence of PMTs within a window comparable to the detector's light crossing time; the coincidence level thus corresponds to a visible energy threshold. Physics analysis is usually not limited by the hardware trigger, but rather the ability to reconstruct events. The interaction vertex can be estimated using timing and refined by applying the Cherenkov angle constraint to identified ring edges. Multi-ring events are more strongly constrained, and their vertex resolution is 33–50% better than single rings. Vertex resolution depends on the photosensor density and detector size, with smaller detectors performing somewhat better than large ones (∼ 25 cm is typical for existing devices). Angular resolution is limited by multiple scattering at solar neutrino energies (25–30°) and improves to a few degrees around $E_{vis} = 1\,\mathrm{GeV}$.

A non-showering $(\mu, \pi^{\pm}, p)$ track produces a sharp ring with small contributions from delta rays and other radiated secondaries, while the more diffuse pattern of a showering (e, γ) particle is actually the superposition of many individual rings from charged shower products. Using maximum likelihood techniques and the Cherenkov angle constraint, these two topologies can be distinguished with an efficiency which depends on the photosensor density and detector size [45]. This particle identification capability has been confirmed by using cosmic-rays and Michel electrons, as well as charged-particle [46] and neutrino [47] beams. Large detectors perform somewhat better than smaller ones with identical photocathode coverage; a misidentification probability of $\sim 0.4\%/\xi$ in the sub-GeV range is consistent with the performance of several experiments for $4\% < \xi < 40\%$. Detection of a delayed coincidence from muon decay offers another, more indirect, means of particle identification; with suitable electronics, efficiency approaches 100% for μ^+ decays but is limited by nuclear absorption (22% probability in water) for μ^-.

Reconstruction of multiple Cherenkov rings presents a challenging pattern recognition problem, which must be attacked by some combination of heuristics, maximum likelihood fitting, Hough transforms and/or neural networks. The problem itself is somewhat ill-defined since, as noted, even a single showering primary produces many closely-overlapping rings. For $\pi^0 \to \gamma\gamma$ two-ring identification, performance falls off rapidly with increasing π^0 momentum, and selection criteria must be optimized with respect to the analysis-dependent cost-function for $e \leftrightarrow \pi^0$ mis-identification. Two representative cases for $\xi = 39\%$ will be illustrated. In an atmospheric neutrino experiment, where π^0 are relatively rare compared to $e^{\pm}$, one can isolate a $> 90\%$ pure 500 MeV/c π^0 sample with an efficiency of ∼ 40%. In a ν_e appearance experiment at $E_\nu \leq 1\,\mathrm{GeV}$, where $e^{\pm}$ are rare compared to π^0, a 99% pure 500 MeV/c electron sample can be identified with an efficiency of ∼ 70%. For constant ξ, a larger detector (with, perforce, a greater number of pixels to sample the light distribution) performs somewhat better at multi-ring separation than a smaller one. For a more detailed discussion of event reconstruction techniques, see Ref. 36.

28.5. Transition radiation detectors (TRD's)

Revised September 2003 by D. Froidevaux (CERN).

It is clear from the discussion in the section on "Passages of Particles Through Matter" (Sec. 27 of this *Review*) that transition radiation (TR) only becomes useful for particle detectors when the signal can be observed as x rays emitted along the particle direction for Lorentz factors γ larger than 1000. In practice, TRD's are therefore used to provide electron/pion separation for $0.5\ \mathrm{GeV}/c \lesssim p \lesssim 100\ \mathrm{GeV}/c$. The charged-particle momenta have usually been measured elsewhere in the detector in the past [57].

Table 28.3: Properties of Cherenkov tracking calorimeters. LSND was a hybrid scintillation/Cherenkov detector; the estimated ratio of isotropic to Cherenkov photoelectrons was about 5:1. MiniBooNE's light yield also includes a small scintillation component.

Detector	Fiducial mass (kton)	PMTs (diameter, cm)	ξ	p.e./ MeV	Dates
IMB-1 [48]	3.3 H_2O	2048 (12.5)	1%	0.25	1982–85
IMB-3 [49]	3.3 H_2O	2048 (20 +plate)	4.5%	1.1	1987–90
KAM I [50,51]	0.88/0.78 H_2O	1000/948 (50)	20%	3.4	1983–85
KAM II [52]	1.04 H_2O	948 (50)	20%	3.4	1986–90
LSND [53]	0.084 oil+scint.	1220 (20)	25%	33	1993–98
SK-1 [54]	22.5 H_2O	11146 (50)	39%	6	1997–2001
SK-2	22.5 H_2O	5182 (50)	18%	3	2002–
K2K [55]	0.025 H_2O	680 (50)	39%	6	1999–
SNO [56]	1.0 D_2O	9456 (20+cone)	55%	9	1999–
MiniBooNE	0.445 oil	1280 (20)	10%	3–4	2002–

Since soft x rays, in the useful energy range between 2 and 20 keV, are radiated with about 1% probability per boundary crossing, practical detectors use radiators with several hundred interfaces, *e.g.* foils or fibers of low-Z materials such as polypropylene (or, more rarely, lithium) in a gas. Absorption inside the radiator itself and in the inactive material of the x-ray detector is important and limits the usefulness of the softer x rays, but interference effects are even larger, and saturate the x-ray yield for electron energies above a few GeV [58,59].

A classical detector is composed of several similar modules, each consisting of a radiator and an x-ray detector, which is usually a wire chamber operated with a xenon-rich mixture, in order to efficiently absorb the x rays. The most prominent and recent examples of such detectors for large-scale experiments are the TRD detectors of NOMAD [60], ALICE [61], and PHENIX. Since transition-radiation photons are mostly emitted at very small angles with respect to the charged-particle direction, the x-ray detector most often detects the sum of the ionization loss (dE/dx) of the charged particle in the gas and energy deposition of the x rays. The discrimination between electrons and pions can be based on the charges measured in each detection module, on the number of energy clusters observed above an optimal threshold (usually in the 5 to 7 keV region), or on more sophisticated methods analyzing the pulse shape as a function of time. Once properly calibrated and optimized, most of these methods yield very similar results.

Development work over the past years for accelerator (ATLAS [62]) and space (AMS [63], PAMELA [64] applications has aimed at increasing the intrinsic quality of the TRD-performance by increasing the probability per detection module of observing a signal from TR-photons produced by electrons. This has been achieved experimentally by distributing small-diameter straw-tube detectors uniformly throughout the radiator material. This method has thereby also cured one of the major drawbacks of more classical TRD's, that is, their need to rely on another detector to measure the charged-particle trajectory. For example, in the ATLAS Transition Radiator Tracker [65] charged particles cross about 35 straw tubes embedded in the radiator material. Dedicated R&D work and detailed simulations have shown that the combination of charged-track measurement and particle identification in the same detector will provide a very powerful tool even at the highest LHC luminosity [66].

The major factor in the performance of any TRD is its overall length. This is illustrated in Fig. 28.2, which shows, for a variety of detectors, the measured (or predicted) pion efficiency at a fixed electron efficiency of 90% as a function of the overall detector length. The experimental data cover too wide a range of particle energies (from a few GeV to 40 GeV) to allow for a quantitative fit to a universal curve. Fig. 28.2 shows that an order of magnitude in rejection power against pions is gained each time the detector length is increased by ~ 20 cm.

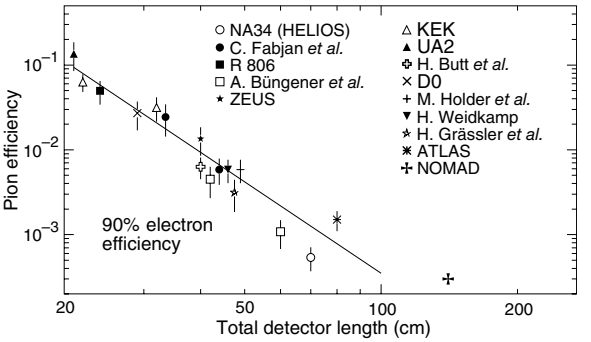

Figure 28.2: Pion efficiency measured (or predicted) for different TRDs as a function of the detector length for a fixed electron efficiency of 90%. The experimental data are directly taken or extrapolated from references [67–79,60](NA34 to NOMAD).

28.6. Wire chambers

Written October 1999 by A. Cattai and G. Rolandi (CERN).

A wire chamber relies on the detection of a large fraction of the charge created in a volume filled with an appropriate gas mixture. A charged particle traversing a gas layer of thickness Δ produces electron-ion pairs along its path (see Sec. 27.2). The yield $(1/\lambda)$ of ionization encounters for a minimum ionization particle (m.i.p.) (see Fig. 27.1) is given in Table 28.4.

Table 28.4: For various gases at STP: (a) yield of ionization encounters $(1/\lambda)$ for m.i.p. [80], (b) t_{99}: thickness of the gas layer for 99% efficiency, and (c) the average number of free electrons produced by a m.i.p. (calculated using data from Ref. 81).

	Encounters/cm	t_{99}(mm)	Free electrons/cm
He	5	9.2	16
Ne	12	3.8	42
Ar	25	1.8	103
Xe	46	1.0	340
CH_4	27	1.7	62
CO_2	35	1.3	107
C_2H_6	43	1.1	113

The probability to have at least one ionization encounter is $1-\exp(-\Delta/\lambda)$ and the thickness of the gas layer for 99% efficiency is $t_{99} = 4.6\lambda$. Depending on the gas, some 65–80% of the encounters result in the production of only one electron; the probability that a cluster has more than five electrons is smaller than 10%. However the tail of the distribution is very long and the yield of ionization electrons is 3–4 times that of the ionization encounters. The secondary ionization happens either in collisions of (primary) ionization electrons with atoms or through intermediate excited states. The process is non-linear and gas mixtures may have larger yields than each of their components. See also the discussion in Sec. 27.7.

Under the influence of electric and magnetic fields the ionization electrons drift inside the gas with velocity $\boldsymbol{u}$ given by:

$$\boldsymbol{u} = \mu|\boldsymbol{E}|\frac{1}{1+\omega^2\tau^2}\left(\widehat{\boldsymbol{E}} + \omega\tau(\widehat{\boldsymbol{E}}\times\widehat{\boldsymbol{B}}) + \omega^2\tau^2(\widehat{\boldsymbol{E}}\cdot\widehat{\boldsymbol{B}})\widehat{\boldsymbol{B}}\right) \qquad (28.11)$$

where $\widehat{\boldsymbol{E}}$ and $\widehat{\boldsymbol{B}}$ are unit vectors in the directions of the electric and magnetic fields respectively, μ is the electron mobility in the gas, ω is the cyclotron frequency eB/mc, and $\tau = \mu m/e$ is the mean time between collisions of the drifting electrons. The magnitude of the drift velocity depends on many parameters; typical values are in the range 1–8 cm/μs.

In a quite common geometry, the drift electric field is perpendicular to the magnetic field. In this case the electrons drift at an angle ψ with respect to the electric field direction such that $\tan\psi = \omega\tau$.

The ionization electrons are eventually collected by a thin (typically 10 μm radius) anode wire where a strong electric field—increasing as $1/r$—accelerates the electrons enough to produce secondary ionization and hence an avalanche. A quenching gas (organic molecules with large photo-absorption cross-section) absorbs the majority of the photons produced during the avalanche development, keeping the avalanche region localized. The gain achievable with a wire counter depends exponentially on the charge density on the wire, on the gas density ρ and—through it—on pressure and temperature: $dG/G \approx -K\,d\rho/\rho$, where the coefficient K ranges between 5 and 8 in practical cases. Gains larger than 10^4 can be obtained in proportional mode.

The electrons produced in the avalanche are collected by the wire in a few nanoseconds. The positive ions move away from the wire and generate a signal that can be detected with an amplifier. Depending on whether the wire is treated as a current source or a voltage source, the signal is described respectively by:

$$I(t) = q\frac{d}{dt}F(t)\ ; \qquad \Delta V(t) = \frac{q}{C}F(t)\ , \tag{28.12}$$

where q is the positive charge in the avalanche, C is the capacitance between the anode wire and the cathodes and $F(t) = \ln(1 + t/t_0)/\ln(1 + t_{\max}/t_0)$. The constant t_0 is of the order of one or few nanoseconds; the constant $t_{\max}$ (several microseconds) describes the time that it takes ions to reach the cathodes.

A sketch of the first multi-wire proportional chamber (MWPC) [82] is shown in Fig. 28.3. It consists of a plane of parallel sense wires with spacing s and length L inserted in a gap of thickness Δ. The potential distributions and fields in a proportional or drift chamber can usually be calculated with good accuracy from the exact formula for the potential around an array of parallel line charges q (coul/m) along z and located at $y = 0$, $x = 0$, $\pm s$, $\pm 2s$, ...,

$$V(x,y) = -\frac{q}{4\pi\,\epsilon_0}\ln\left\{4\left[\sin^2\left(\frac{\pi x}{s}\right) + \sinh^2\left(\frac{\pi y}{s}\right)\right]\right\}\ . \tag{28.13}$$

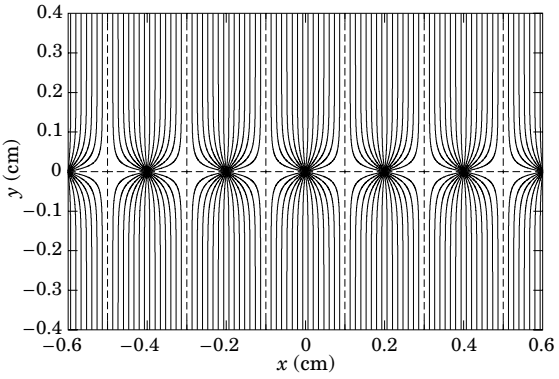

Figure 28.3: Electric field lines in a (MWPC) with an anode pitch of 2 mm as calculated with GARFIELD program [83].

With digital readout, the resolution in the direction perpendicular to the wire is $s/\sqrt{12}$, where s is typically 1–2 mm. Similar resolution can be achieved with a smaller channel density by measuring the difference in time between the arrival of electrons at the wire and the traversal of the particle, albeit with a longer response time. In the case of drift chambers, the spatial resolution is limited by the diffusion of ionization electrons during the drift and by the fluctuations of the ionization process. Depending on the gas mixture, the width of the diffusing cloud after 1 cm of drift is typically between 50 and 300 μm; small diffusion implies low drift velocity. With drift lengths up to 5 cm (1 μs), resolutions in the range 100–200 μm have been achieved in chambers with surface areas of several square meters [84]. The central detectors in many collider experiments are drift chambers with the wires parallel to the beam direction. Small volume chambers (0.1 m^3) have been used for vertex measurement achieving resolutions of 50 μm using high pressure (2–4 bar) and low diffusion gas mixtures [85]. Large volume chambers (5–40 m^3) with several thousand wires of length of 1–2 meters are operated with resolution between 100 and 200 μm [86].

The spatial resolution cannot be improved by arbitrarily reducing the spacing of the wires. In addition to the practical difficulties of precisely stringing wires at a pitch below 1 mm, there is a fundamental limitation: the electrostatic force between the wires is balanced by the mechanical tension, which cannot exceed a critical value. This gives the following approximate stability condition:

$$\frac{s}{L} \geq 1.5 \times 10^{-3} V(\mathrm{kV})\sqrt{\frac{20\ \mathrm{g}}{T}}\ , \tag{28.14}$$

where V is the voltage of the sense wire and T is the tension of the wire in grams-weight equivalent.

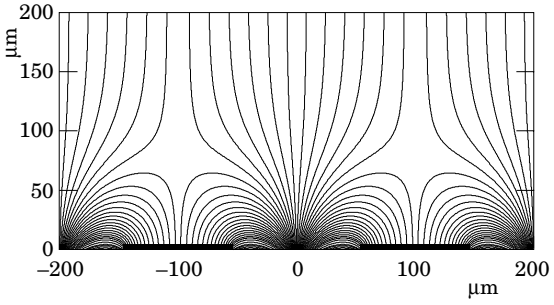

Figure 28.4: Electron drift lines in a micro-strip gas chamber with a pitch of 200 μm.

This limitation can be overcome by means of lithographic techniques [87]: a series of thin aluminum strips are precisely 0.2 μm engraved on an insulating support producing a miniaturized version of a MWPC (see Fig. 28.4). With this technique the spacing of the anodes can be reduced to 0.1–0.2 mm, reducing the drift time of the ions and improving on the spatial resolution and on the rate capability of the chamber.

In all these devices, since the avalanche is very localized along the anode, signals induced on nearby electrodes can be used to measure the coordinate along the anode direction (see Sec. 28.7).

A review of the principle of particle detection with drift chambers can be found in [88]. A compilation of the mobilities, diffusion coefficients and drift deflection angles as a function of $\boldsymbol{E}$ and $\boldsymbol{B}$ for several gas mixtures used in proportional chambers can be found in [89]. A review of micro-strip gas chambers (MSGC) can be found in [90].

28.7. Time-projection chambers

Written November 1997 by M.T Rownan; revised August 2003.

Detectors with long drift distances perpendicular to a multi-anode proportional plane provide three-dimensional information, with one being the time projection. A (typically strong) magnetic field parallel to the drift direction suppresses transverse diffusion ($\sigma = \sqrt{2Dt}$) by a factor

$$D(B)/D(0) = \frac{1}{1 + \omega^2\tau^2}\ , \tag{28.15}$$

where D is the diffusion coefficient, $\omega = eB/mc$ is the cyclotron frequency, and τ is the mean time between collisions. Multiple measurements of energy deposit along the particle trajectory combined with the measurement of momentum in the magnetic field allows excellent particle identification [91], as can be seen in Fig. 28.5.

A typical gas-filled TPC consists of a long uniform drift region (1–2 m) generated by a central high-voltage membrane and precision concentric cylindrical field cages within a uniform, parallel magnetic field [88]. Details of construction and electron trajectories near the anode end are shown in Fig. 28.6. Signal shaping and processing using analog storage devices or FADC's allows excellent pattern recognition,

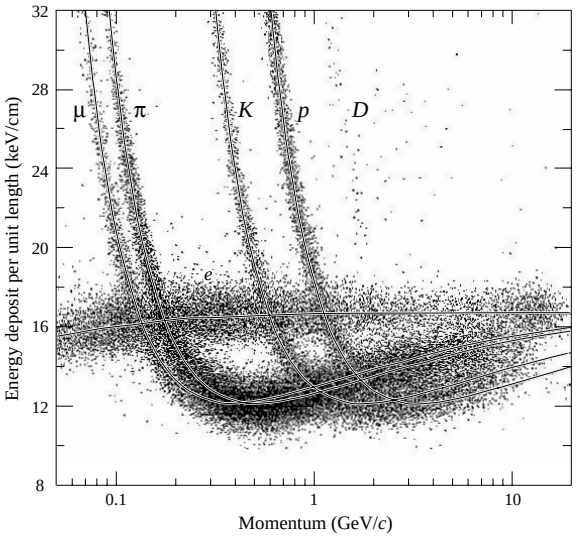

Figure 28.5: PEP4/9-TPC energy-deposit measurements (185 samples @8.5 atm Ar-CH_4 80–20%) in multihadron events. The electrons reach a Fermi plateau value of 1.4 times the most probably energy deposit at minimum ionization. Muons from pion decays are separated from pions at low momentum; π/K are separated over all momenta except in the cross-over region. (Low-momentum protons and deuterons originate from hadron-nucleus collisions in inner materials such as the beam pipe.)

track reconstruction, and particle identification within the same detector.

Typical values:	
Gas: Ar + (10–20%) CH_4	Pressure(P) = 1–8.5 atm.
E/P = 100–200 V/cm/atm	B = 1–1.5 Tesla
$v_{\rm drift}$ = 5–7 cm/μs	$\omega\tau$ = 1–8
$\sigma_{x\ {\rm or}\ y}$ = 100–200 μm	σ_z = 0.2–1 mm
σ_{Edep} = 2.5–5.5 %	

Truncated mean energy-deposit resolution depends on the number and size of samples, and gas pressure:

$$\sigma_{Edep} \propto N^{-0.43} \times (P\ell)^{-0.32} \ . \qquad (28.16)$$

Here N is the number of samples, ℓ is the sample size, and P is the pressure. Typical energy-deposit distributions are shown in Fig. 28.5. Good three-dimensional two-track resolutions of about 1–1.5 cm are routinely achieved.

$E \times B$ distortions arise from nonparallel E and B fields (see Eq. (28.11)), and from the curved drift of electrons to the anode wires in the amplification region. Position measurement errors include contributions from the anode-cathode geometry, the track crossing angle (α), $E \times B$ distortions, and from the drift diffusion of electrons

$$\sigma^2_{x\ {\rm or}\ y} = \sigma_0^2 + \sigma_D^2(1+\tan^2\alpha)L/L_{\rm max} + \sigma_\alpha^2(\tan\alpha - \tan\psi)^2 \qquad (28.17)$$

where σ is the coordinate resolution, σ_0 includes the anode-cathode geometry contribution, ψ is the Lorentz angle, and L is the drift distance.

Space-charge distortions arise in high-rate environments, especially for low values of $\omega\tau$. However, they are mitigated by an effective gating grid (Fig. 28.6). Field uniformities of

$$\int (E_\perp/E)\, dz \lesssim 0.5\text{–}1 \text{ mm} \ , \qquad (28.18)$$

over 10–40 m^3 volumes have been obtained. Laser tracks and calibration events allow mapping of any remnant drift non-uniformities.

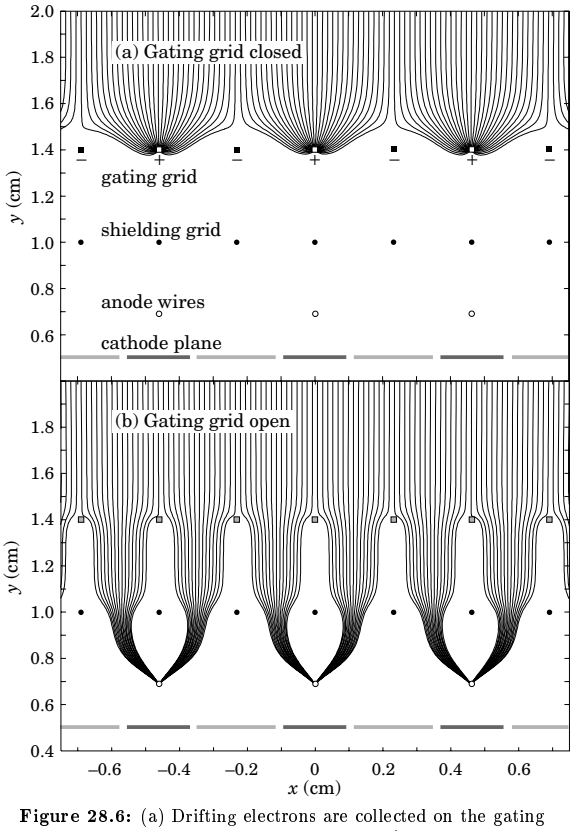

Figure 28.6: (a) Drifting electrons are collected on the gating grid until gated open by a triggering event. A shielding grid at ground potential is used to terminate the drift region. Electrons drifting through an open gating grid (b) pass through to the amplification region around the anode wires. Positive ions generated in the avalanche are detected on segmented cathode pads to provide precise measurements along the wire. The slow positive ions are blocked from entering the drift region by closing the gating grid after the electrons have drifted through.

28.8. Silicon semiconductor detectors

Updated August 2003 by H. Spieler (LBNL).

Semiconductor detectors are widely used in modern high-energy physics experiments. They are the key ingredient of high-resolution vertex and tracking detectors and are also used as photodetectors in scintillation calorimeters. The most commonly used material is silicon, but germanium, gallium-arsenide and diamond are also useful in some applications. Integrated circuit technology allows the formation of high-density micron-scale electrodes on large (10–15 cm diameter) wafers, providing excellent position resolution. Furthermore, the density of silicon and its small ionization energy result in adequate signals with active layers only 100–300 μm thick, so the signals are also fast (typically tens of ns). Semiconductor detectors depend crucially on low-noise electronics (see Sec. 28.9), so the detection sensitivity is determined by signal charge and capacitance. For a survey of recent developments see Ref. 92.

Silicon detectors are p-n junction diodes operated at reverse bias. This forms a sensitive region depleted of mobile charge and sets up an electric field that sweeps charge liberated by radiation to the electrodes. Detectors typically use an asymmetric structure, e.g. a highly doped p electrode and a lightly doped n region, so that the depletion region extends predominantly into the lightly doped volume.

The thickness of the depleted region is

$$W = \sqrt{2\epsilon(V + V_{bi})/Ne} = \sqrt{2\rho\mu\epsilon(V + V_{bi})}\,, \qquad (28.19)$$

where $V =$ external bias voltage
$V_{bi} =$ "built-in" voltage (≈ 0.5 V for resistivities typically used in detectors)
$N =$ doping concentration
$e =$ electronic charge
$\epsilon =$ dielectric constant $= 11.9\ \epsilon_0 \approx 1$ pF/cm
$\rho =$ resistivity (typically 1–10 kΩ cm)
$\mu =$ charge carrier mobility
$= 1350$ cm^2 V^{-1} s^{-1} for electrons
$= 450$ cm^2 V^{-1} s^{-1} for holes

or

$W = 0.5\ [\mu\text{m}/\sqrt{\Omega\text{-cm}\cdot\text{V}}] \times \sqrt{\rho(V + V_{bi})}$ for n-type material, and

$W = 0.3\ [\mu\text{m}/\sqrt{\Omega\text{-cm}\cdot\text{V}}] \times \sqrt{\rho(V + V_{bi})}$ for p-type material.

The conductive p and n regions together with the depleted volume form a capacitor with the capacitance per unit area

$$C = \epsilon/W \approx 1\,[\text{pF/cm}]\ /W\ . \qquad (28.20)$$

In strip and pixel detectors the capacitance is dominated by the fringing capacitance. For example, the strip-to-strip fringing capacitance is $\sim$ 1–1.5 pF cm^{-1} of strip length at a strip pitch of 25–50 μm.

For energetic particles and photons the energy required to create an electron-hole pair $E_i = 3.6$ eV (which is larger than the band gap because phonon excitation is required for momentum conservation). For minimum-ionizing particles, the most probable charge deposition in a 300 μm thick silicon detector is about 3.5 fC (22000 electrons). Since both electronic and lattice excitations are involved, the variance in the number of charge carriers $N = E/E_i$ produced by an absorbed energy E is reduced by the Fano factor F (about 0.1 in Si). Thus, $\sigma_N = \sqrt{FN}$ and the energy resolution $\sigma_E/E = \sqrt{FE_i/E}$. However, the measured signal fluctuations are usually dominated by electronic noise or energy loss fluctuations in the detector. Visible light can be detected with photon energies above the band gap. In optimized photodiodes quantum efficiencies $> 80\%$ for wavelengths between 400 nm and nearly 1 μm are achievable. UV-extended photodiodes have useful efficiency down to 200 nm.

Charge collection time decreases with increasing bias voltage, and can be reduced further by operating the detector with "overbias," *i.e.*, a bias voltage exceeding the value required to fully deplete the device. The collection time is limited by velocity saturation at high fields (approaching 10^7 cm/s at $E > 10^4$ V/cm); at an average field of 10^4 V/cm the collection time is about 15 ps/μm for electrons and 30 ps/μm for holes. In typical fully-depleted detectors 300 μm thick, electrons are collected within about 10 ns, and holes within about 25 ns.

Position resolution is limited by transverse diffusion during charge collection (typically 5 μm for 300 μm thickness) and by knock-on electrons. Resolutions of 2–4 μm (rms) have been obtained in beam tests. In magnetic fields, the Lorentz drift deflects the electron and hole trajectories and the detector must be tilted to reduce spatial spreading (see "Hall effect" in semiconductor textbooks).

Radiation damage occurs through two basic mechanisms:

1. Bulk damage due to displacement of atoms from their lattice sites. This leads to increased leakage current, carrier trapping, and build-up of space charge that changes the required operating voltage. Displacement damage depends on the nonionizing energy loss and the energy imparted to the recoil atoms, which can initiate a chain of subsequent displacements, *i.e.*, damage clusters. Hence, it is critical to consider both particle type and energy.
2. Surface damage due to charge build-up in surface layers, which leads to increased surface leakage currents. In strip detectors the inter-strip isolation is affected. The effects of charge build-up are strongly dependent on the device structure and on fabrication details. Since the damage is proportional to the absorbed energy (when ionization dominates), the dose can be specified in rad (or Gray) independent of particle type.

The increase in reverse bias current due to bulk damage is $\Delta I_r = \alpha\Phi$ per unit volume, where Φ is the particle fluence and α the damage coefficient ($\alpha \approx 3 \times 10^{-17}$ A/cm for minimum ionizing protons and pions after long-term annealing; $\alpha \approx 2 \times 10^{-17}$ A/cm for 1 MeV neutrons). The reverse bias current depends strongly on temperature

$$\frac{I_R(T_2)}{I_R(T_1)} = \left(\frac{T_2}{T_1}\right)^2 \exp\left[-\frac{E}{2k}\left(\frac{T_1 - T_2}{T_1 T_2}\right)\right] \qquad (28.21)$$

where $E = 1.2$ eV, so rather modest cooling can reduce the current substantially ($\sim$ 6-fold current reduction in cooling from room temperature to 0°C).

The space-charge concentration in high-resistivity n-type Si changes approximately as

$$N = N_0 e^{-\delta\Phi} - \beta\Phi\ , \qquad (28.22)$$

where N_0 is the initial donor concentration, $\delta \approx 6 \times 10^{-14}$ cm^2 determines donor removal, and $\beta \approx 0.03$ cm^{-1} describes acceptor creation. The acceptor states trap electrons, building up a negative space charge, which in turn requires an increase in the applied voltage to sweep signal charge through the detector thickness. This has the same effect as a change in resistivity, *i.e.*, the required voltage drops initially with fluence, until the positive and negative space charge balance and very little voltage is required to collect all signal charge. At larger fluences the negative space charge dominates, and the required operating voltage increases ($V \propto N$). The safe operating limit of depletion voltage ultimately limits the detector lifetime. Strip detectors specifically designed for high voltages have been operated at bias voltages >500V. Since the effect of radiation damage depends on the electronic activity of defects, various techniques have been applied to neutralize the damage sites. For example, additional doping with oxygen increases the allowable charged hadron fluence roughly three-fold [93]. The increase in leakage current with fluence, on the other hand, appears to be unaffected by resistivity and whether the material is n or p-type.

Strip and pixel detectors have remained functional at fluences beyond 10^{15} cm^{-2} for minimum ionizing protons. At this damage level, charge loss due to recombination and trapping also becomes significant and the high signal-to-noise ratio obtainable with low-capacitance pixel structures extends detector lifetime. The occupancy of the defect charge states is strongly temperature dependent; competing processes can increase or decrease the required operating voltage. It is critical to choose the operating temperature judiciously (-10 to 0°C in typical collider detectors) and limit warm-up periods during maintenance. For a more detailed summary see Ref. 94 and and the web-site of the ROSE collaboration at `http://RD48.web.cern.ch/rd48`.

Currently, the lifetime of detector systems is still limited by the detectors; in the electronics use of standard "deep submicron" CMOS fabrication processes with appropriately designed circuitry has increased the radiation resistance to fluences $> 10^{15}$ cm^{-2} of minimum ionizing protons or pions. For a comprehensive discussion of radiation effects see Ref. 95.

28.9. Low-noise electronics

Revised August 2003 by H. Spieler (LBNL).

Many detectors rely critically on low-noise electronics, either to improve energy resolution or to allow a low detection threshold. A typical detector front-end is shown in Fig. 28.7.

The detector is represented by a capacitance C_d, a relevant model for most detectors. Bias voltage is applied through resistor R_b and the signal is coupled to the preamplifier through a blocking capacitor C_c. The series resistance R_s represents the sum of all resistances present in the input signal path, *e.g.* the electrode resistance, any input protection networks, and parasitic resistances in the input transistor. The preamplifier provides gain and feeds a pulse shaper, which tailors

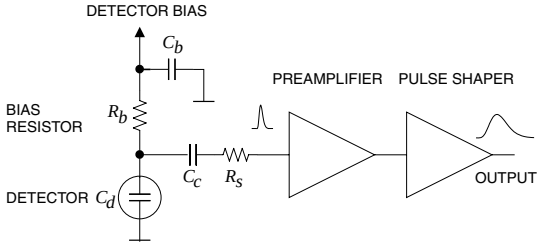

Figure 28.7: Typical detector front-end circuit.

the overall frequency response to optimize signal-to-noise ratio while limiting the duration of the signal pulse to accommodate the signal pulse rate. Even if not explicitly stated, all amplifiers provide some form of pulse shaping due to their limited frequency response.

The equivalent circuit for the noise analysis (Fig. 28.8) includes both current and voltage noise sources. The leakage current of a semiconductor detector, for example, fluctuates due to electron emission statistics. This "shot noise" i_{nd} is represented by a current noise generator in parallel with the detector. Resistors exhibit noise due to thermal velocity fluctuations of the charge carriers. This noise source can be modeled either as a voltage or current generator. Generally, resistors shunting the input act as noise current sources and resistors in series with the input act as noise voltage sources (which is why some in the detector community refer to current and voltage noise as "parallel" and "series" noise). Since the bias resistor effectively shunts the input, as the capacitor C_b passes current fluctuations to ground, it acts as a current generator i_{nb} and its noise current has the same effect as the shot noise current from the detector. Any other shunt resistances can be incorporated in the same way. Conversely, the series resistor R_s acts as a voltage generator. The electronic noise of the amplifier is described fully by a combination of voltage and current sources at its input, shown as e_{na} and i_{na}.

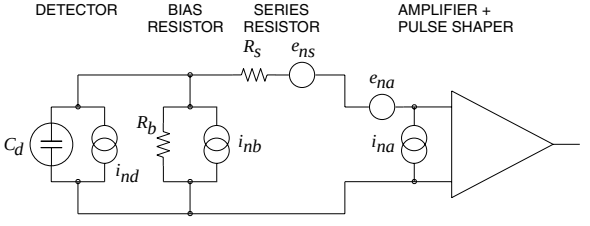

Figure 28.8: Equivalent circuit for noise analysis.

Shot noise and thermal noise have a "white" frequency distribution, *i.e.* the spectral power densities $dP_n/df \propto di_n^2/df \propto de_n^2/df$ are constant with the magnitudes

$$\begin{aligned} i_{nd}^2 &= 2eI_d \ , \\ i_{nb}^2 &= \frac{4kT}{R_b} \ , \\ e_{ns}^2 &= 4kTR_s \ , \end{aligned} \tag{28.23}$$

where e is the electronic charge, I_d the detector bias current, k the Boltzmann constant and T the temperature. Typical amplifier noise parameters e_{na} and i_{na} are of order $\mathrm{nV}/\sqrt{\mathrm{Hz}}$ and $\mathrm{pA}/\sqrt{\mathrm{Hz}}$. Trapping and detrapping processes in resistors, dielectrics and semiconductors can introduce additional fluctuations whose noise power frequently exhibits a $1/f$ spectrum. The spectral density of the $1/f$ noise voltage is

$$e_{nf}^2 = \frac{A_f}{f} \ , \tag{28.24}$$

where the noise coefficient A_f is device specific and of order 10^{-10}–$10^{-12}\,\mathrm{V}^2$.

A fraction of the noise current flows through the detector capacitance, resulting in a frequency-dependent noise voltage $i_n/(\omega C_d)$, which is added to the noise voltage in the input circuit. Since the individual noise contributions are random and uncorrelated, they add in quadrature. The total noise at the output of the pulse shaper is obtained by integrating over the full bandwidth of the system. Superimposed on repetitive detector signal pulses of constant magnitude, purely random noise produces a Gaussian signal distribution.

Since radiation detectors typically convert the deposited energy into charge, the system's noise level is conveniently expressed as an equivalent noise charge Q_n, which is equal to the detector signal that yields a signal-to-noise ratio of one. The equivalent noise charge is commonly expressed in Coulombs, the corresponding number of electrons, or the equivalent deposited energy (eV). For a capacitive sensor

$$Q_n^2 = i_n^2 F_i T_S + e_n^2 F_v \frac{C^2}{T_S} + F_{vf} A_f C^2 \ , \tag{28.25}$$

where C is the sum of all capacitances shunting the input, F_i, F_v, and F_{vf} depend on the shape of the pulse determined by the shaper and T_s is a characteristic time, for example, the peaking time of a semi-gaussian pulse or the sampling interval in a correlated double sampler. The form factors F_i, F_v are easily calculated

$$F_i = \frac{1}{2T_S} \int_{-\infty}^{\infty} [W(t)]^2 \, dt \ , \qquad F_v = \frac{T_S}{2} \int_{-\infty}^{\infty} \left[\frac{dW(t)}{dt} \right]^2 dt \ , \tag{28.26}$$

where for time-invariant pulse-shaping $W(t)$ is simply the system's impulse response (the output signal seen on an oscilloscope) with the peak output signal normalized to unity. For more details see Refs. [96–97].

A pulse shaper formed by a single differentiator and integrator with equal time constants has $F_i = F_v = 0.9$ and $F_{fv} = 4$, independent of the shaping time constant. The overall noise bandwidth, however, depends on the time constant, *i.e.* the characteristic time T_s. The contribution from noise currents increases with shaping time, *i.e.*, pulse duration, whereas the voltage noise decreases with increasing shaping time. Noise with a $1/f$ spectrum depends only on the ratio of upper to lower cutoff frequencies (integrator to differentiator time constants), so for a given shaper topology the $1/f$ contribution to Q_n is independent of T_s. Furthermore, the contribution of noise voltage sources to Q_n increases with detector capacitance. Pulse shapers can be designed to reduce the effect of current noise, *e.g.*, mitigate radiation damage. Increasing pulse symmetry tends to decrease F_i and increase F_v (*e.g.*, to 0.45 and 1.0 for a shaper with one CR differentiator and four cascaded integrators). For the circuit shown in Fig. 28.8,

$$\begin{aligned} Q_n^2 = &\left(2eI_d + 4kT/R_b + i_{na}^2 \right) F_i T_S \\ &+ \left(4kTR_s + e_{na}^2 \right) F_v C_d^2 / T_S + F_{vf} A_f C_d^2 \ . \end{aligned} \tag{28.27}$$

As the characteristic time T_S is changed, the total noise goes through a minimum, where the current and voltage contributions are equal. Fig. 28.9 shows a typical example. At short shaping times the voltage noise dominates, whereas at long shaping times the current noise takes over. The noise minimum is flattened by the presence of $1/f$ noise. Increasing the detector capacitance will increase the voltage noise and shift the noise minimum to longer shaping times.

For quick estimates, one can use the following equation, which assumes an FET amplifier (negligible i_{na}) and a simple CR–RC shaper with time constants τ (equal to the peaking time):

$$\begin{aligned} (Q_n/e)^2 = &\, 12 \left[\frac{1}{\mathrm{nA \cdot ns}} \right] I_d \tau + 6 \times 10^5 \left[\frac{\mathrm{k\Omega}}{\mathrm{ns}} \right] \frac{\tau}{R_b} \\ &+ 3.6 \times 10^4 \left[\frac{\mathrm{ns}}{(\mathrm{pF})^2 (\mathrm{nV})^2 / \mathrm{Hz}} \right] e_n^2 \frac{C^2}{\tau} \ . \end{aligned} \tag{28.28}$$

Noise is improved by reducing the detector capacitance and leakage current, judiciously selecting all resistances in the input circuit, and choosing the optimum shaping time constant.

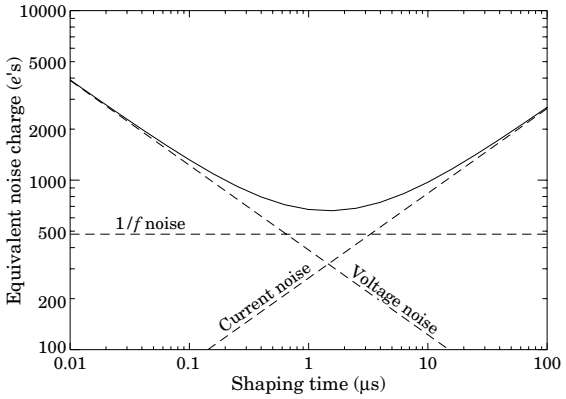

Figure 28.9: Equivalent noise charge vs shaping time.

The noise parameters of the amplifier depend primarily on the input device. In field effect transistors, the noise current contribution is very small, so reducing the detector leakage current and increasing the bias resistance will allow long shaping times with correspondingly lower noise. In bipolar transistors, the base current sets a lower bound on the noise current, so these devices are best at short shaping times. In special cases where the noise of a transistor scales with geometry, *i.e.*, decreasing noise voltage with increasing input capacitance, the lowest noise is obtained when the input capacitance of the transistor is equal to the detector capacitance, albeit at the expense of power dissipation. Capacitive matching is useful with field-effect transistors, but not bipolar transistors. In bipolar transistors, the minimum obtainable noise is independent of shaping time, but only at the optimum collector current I_C, which does depend on shaping time.

$$Q^2_{n,\min} = 4kT\frac{C}{\sqrt{\beta_{DC}}}\sqrt{F_i F_v} \quad \text{at} \quad I_c = \frac{kT}{e}C\sqrt{\beta_{DC}}\sqrt{\frac{F_v}{F_i}}\frac{1}{T_S}\,, \quad (28.29)$$

where β_{DC} is the DC current gain. For a CR–RC shaper and $\beta_{DC} = 100$,

$$Q_{n,\min}/e \approx 250\sqrt{C/\text{pF}}\,. \quad (28.30)$$

Practical noise levels range from $\sim 1e$ for CCDs at long shaping times to $\sim 10^4$ e in high-capacitance liquid argon calorimeters. Silicon strip detectors typically operate at $\sim 10^3$ e electrons, whereas pixel detectors with fast readout provide noise of several hundred electrons.

In timing measurements, the slope-to-noise ratio must be optimized, rather than the signal-to-noise ratio alone, so the rise time t_r of the pulse is important. The "jitter" σ_t of the timing distribution is

$$\sigma_t = \frac{\sigma_n}{(dS/dt)_{S_T}} \approx \frac{t_r}{S/N}\,, \quad (28.31)$$

where σ_n is the rms noise and the derivative of the signal dS/dt is evaluated at the trigger level S_T. To increase dS/dt without incurring excessive noise, the amplifier bandwidth should match the rise-time of the detector signal. The 10 to 90% rise time of an amplifier with bandwidth f_U is $0.35/f_U$. For example, an oscilloscope with 350 MHz bandwidth has a 1 ns rise time. When amplifiers are cascaded, which is invariably necessary, the individual rise times add in quadrature.

$$t_r \approx \sqrt{t_{r1}^2 + t_{r2}^2 + \ldots + t_{rn}^2}$$

Increasing signal-to-noise ratio also improves time resolution, so minimizing the total capacitance at the input is also important. At high signal-to-noise ratios, the time jitter can be much smaller than the rise time. The timing distribution may shift with signal level ("walk"), but this can be corrected by various means, either in hardware or software [9].

For a more detailed introduction to detector signal processing and electronics see Ref. 98.

28.10. Calorimeters

28.10.1. *Electromagnetic calorimeters*:

Written August 2003 by R.-Y. Zhu (California Inst. of Technology).

The development of electromagnetic showers is discussed in the section on "Passage of Particles Through Matter" (Sec. 27 of this *Review*).

Formulae are given which approximately describe average showers, but since the physics of electromagnetic showers is well understood, detailed and reliable Monte Carlo simulation is possible. EGS4 [99] and GEANT [100] have emerged as the standards.

There are homogeneous and sampling electromagnetic calorimeters. In a homogeneous calorimeter the entire volume is sensitive, *i.e.*, contributes signal. Homogeneous electromagnetic calorimeters may be built with inorganic heavy (high-Z) scintillating crystals such as BGO, CsI, NaI, and PWO, non-scintillating Cherenkov radiators such as lead glass and lead fluoride, or ionizing noble liquids. Properties of commonly used inorganic crystal scintillators can be found in Table 28.2. A sampling calorimeter consists of an active medium which generates signal and a passive medium which functions as an absorber. The active medium may be a scintillator, an ionizing noble liquid, a gas chamber, or a semiconductor. The passive medium is usually a material of high density, such as lead, iron, copper, or depleted uranium.

The energy resolution σ_E/E of a calorimeter can be parametrized as $a/\sqrt{E}\oplus b\oplus c/E$, where $\oplus$ represents addition in quadrature and E is in GeV. The stochastic term a represents statistics-related fluctuations such as intrinsic shower fluctuations, photoelectron statistics, dead material at the front of the calorimeter, and sampling fluctuations. For a fixed number of radiation lengths, the stochastic term a for a sampling calorimeter is expected to be proportional to $\sqrt{t/f}$, where t is plate thickness and f is sampling fraction [101,102]. While a is at a few percent level for a homogeneous calorimeter, it is typically 10% for sampling calorimeters. The main contributions to the systematic, or constant, term b are detector non-uniformity and calibration uncertainty. In the case of the hadronic cascades discussed below, non-compensation also contributes to the constant term. One additional contribution to the constant term for calorimeters built for modern high-energy physics experiments, operated in a high-beam intensity environment, is radiation damage of the active medium. This can be minimized by developing radiation-hard active media [33] and by frequent *in situ* calibration and monitoring [32,102]. With effort, the constant term b can be reduced to below one percent. The term c is due to electronic noise summed over readout channels within a few Molière radii. The best energy resolution for electromagnetic shower measurement is obtained in total absorption homogeneous calorimeters, *e.g.* calorimeters built with heavy crystal scintillators. These are used when ultimate performance is pursued.

The position resolution depends on the effective Molière radius and the transverse granularity of the calorimeter. Like the energy resolution, it can be factored as $a/\sqrt{E}\oplus b$, where a is a few to 20 mm and b can be as small as a fraction of mm for a dense calorimeter with fine granularity. Electromagnetic calorimeters may also provide direction measurement for electrons and photons. This is important for photon-related physics when there are uncertainties in event origin, since photons do not leave information in the particle tracking system. Typical photon angular resolution is about 45 $mrad/\sqrt{E}$, which can be provided by implementing longitudinal segmentation [103] for a sampling calorimeter or by adding a preshower detector [104] for a homogeneous calorimeter without longitudinal segmentation.

Novel technologies have been developed for electromagnetic calorimetry. New heavy crystal scintillators, such as PWO, LSO:Ce, and GSO:Ce (see Sec. 28.2), have attracted much attention for homogeneous calorimetry. In some cases, such as PWO, it has received broad applications in high-energy and nuclear physics experiments. The "spaghetti" structure has been developed for sampling calorimetry with scintillating fibers as the sensitive medium. The "accordion" structure has been developed for sampling calorimetry with ionizing noble liquid as the sensitive medium. Table 28.5 provides a brief description of typical electromagnetic calorimeters built recently for high-energy physics experiments. Also listed in this table are

calorimeter depths in radiation lengths (X_0) and the achieved energy resolution. Whenever possible, the performance of calorimeters *in situ* is quoted, which is usually in good agreement with prototype test beam results as well as EGS or GEANT simulations, provided that all systematic effects are properly included. Detailed references on detector design and performance can be found in Appendix C of reference [102] and Proceedings of the International Conference series on Calorimetry in Particle Physics.

Table 28.5: Resolution of typical electromagnetic calorimeters. E is in GeV.

Technology (Experiment)	Depth	Energy resolution	Date
NaI(Tl) (Crystal Ball)	$20X_0$	$2.7\%/\mathrm{E}^{1/4}$	1983
$Bi_4Ge_3O_{12}$ (BGO) (L3)	$22X_0$	$2\%/\sqrt{E} \oplus 0.7\%$	1993
CsI (KTeV)	$27X_0$	$2\%/\sqrt{E} \oplus 0.45\%$	1996
CsI(Tl) (BaBar)	16–$18X_0$	$2.3\%/E^{1/4} \oplus 1.4\%$	1999
CsI(Tl) (BELLE)	$16X_0$	1.7% for $E_\gamma > 3.5$ GeV	1998
$PbWO_4$ (PWO) (CMS)	$25X_0$	$3\%/\sqrt{E} \oplus 0.5\% \oplus 0.2/E$	1997
Lead glass (OPAL)	$20.5X_0$	$5\%/\sqrt{E}$	1990
Liquid Kr (NA48)	$27X_0$	$3.2\%/\sqrt{E} \oplus 0.42\% \oplus 0.09/E$	1998
Scintillator/depleted U (ZEUS)	20–$30X_0$	$18\%/\sqrt{E}$	1988
Scintillator/Pb (CDF)	$18X_0$	$13.5\%/\sqrt{E}$	1988
Scintillator fiber/Pb spaghetti (KLOE)	$15X_0$	$5.7\%/\sqrt{E} \oplus 0.6\%$	1995
Liquid Ar/Pb (NA31)	$27X_0$	$7.5\%/\sqrt{E} \oplus 0.5\% \oplus 0.1/E$	1988
Liquid Ar/Pb (SLD)	$21X_0$	$8\%/\sqrt{E}$	1993
Liquid Ar/Pb (H1)	20–$30X_0$	$12\%/\sqrt{E} \oplus 1\%$	1998
Liquid Ar/depl. U (DØ)	$20.5X_0$	$16\%/\sqrt{E} \oplus 0.3\% \oplus 0.3/E$	1993
Liquid Ar/Pb accordion (ATLAS)	$25X_0$	$10\%/\sqrt{E} \oplus 0.4\% \oplus 0.3/E$	1996

28.10.2. ***Hadronic calorimeters***: [102,105] The length scale appropriate for hadronic cascades is the nuclear interaction length, given very roughly by

$$\lambda_I \approx 35 \text{ g cm}^{-2} A^{1/3} . \tag{28.32}$$

Longitudinal energy deposition profiles are characterized by a sharp peak near the first interaction point (from the fairly local deposition of EM energy resulting from π^0's produced in the first interaction), followed by a more gradual development with a maximum at

$$x/\lambda_I \equiv t_{\max} \approx 0.2 \ln(E/1 \text{ GeV}) + 0.7 \tag{28.33}$$

as measured from the front of the detector.

The depth required for containment of a fixed fraction of the energy also increases logarithmically with incident particle energy. The thickness of iron required for 95% (99%) containment of cascades induced by single hadrons is shown in Fig. 28.10 [106]. Two of the sets of data are from large neutrino experiments, while the third is from a commonly-used parameterization. Depths as measured in nuclear interaction lengths presumably scale to other materials. From the same data it can be concluded that the requirement that 95% of the energy in 95% of the showers be contained requires 40 to 50 cm (2.4 to 3.0 λ_I) more material material than for an average 95% containment. The transverse dimensions of hadronic showers also scale as λ_I, although most of the energy is contained in a narrow core.

The energy deposit in a hadronic cascade consists of a prompt EM component due to π^0 production and a somewhat slower component mainly due to low-energy hadronic activity. An induction argument verified by Monte-Carlo simulations has shown that the

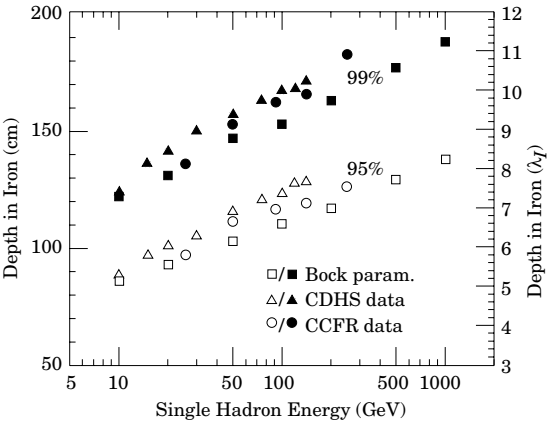

Figure 28.10: Required calorimeter thickness for 95% and 99% hadronic cascade containment in iron, on the basis of data from two large neutrino detectors and the parameterization of Bock *et al.* [106].

fraction of hadronic energy in a cascade is $(E/E_0)^{m-1}$, where $0.80 \lesssim m \lesssim 0.85$ [107]. E_0 is about 1 GeV for incident pions, and the power-law description is approximately valid for incident energy E greater than a few tens of GeV. In general, the electromagnetic and hadronic energy depositions are converted to electrical signals with different efficiencies. The ratio of the conversion efficiencies is usually called the intrinsic e/h ratio. It follows in the power-law approximation the ratio of the responses for incident pions and incident electrons is given by "π/e"$= 1 - (1 - h/e)(E/E_0)^{m-1}$. With or without the power-law approximation the response for pions is not a linear function of energy for $e/h \neq 1$. (But in any case, as the energy increases a larger and larger fraction of the energy is transferred to π^0's, and "π/e"$\to 1$.) If $e/h = 1.0$ the calorimeter is said to be *compensating*. If e/h differs from unity by more than 5% or 10%, detector performance is compromised because of fluctuations in the π^0 content of the cascades. This results in (a) a skewed signal distribution and (b) an almost-constant contribution to detector resolution which is proportional to the degree of noncompensation $|1 - h/e|$. The coefficient relating the size of the constant term to $|1 - h/e|$ is 14% according to FLUKA simulations [107], and 21% according to Wigmans' calculations [108]. (Wigmans now prefers a different approach to the "constant term" [102].)

The formula for "π/e" given above is valid for a large uniform calorimeter. Real calorimeters usually have an EM front structure which is different, and so modifications must be made in modeling the response.

In most cases e/h is greater than unity, particularly if little hydrogen is present or if the gate time is short. This is because much of the low-energy hadronic energy is "hidden" in nuclear binding energy release, low-energy spallation products, *etc.* Partial correction for these losses occurs in a sampling calorimeter with high-Z absorbers, because a disproportionate fraction of electromagnetic energy is deposited in the inactive region. For this reason, a fully sensitive detector such as scintillator or glass cannot be made compensating.

The average electromagnetic energy fraction in a high-energy cascade is smaller for incident protons than for pions; $E_0 \approx 2.6$ GeV rather than ≈ 1 GeV. As a result "π/e">"p/e" (if $e/h > 1$) in a noncompensating calorimeter [107]. This difference has now been measured [109].

Circa 1990 compensation was thought to be very important in hadronic calorimeter design. Motivated very much by the work of Wigmans [108], several calorimeters were built with $e/h \approx 1 \pm 0.02$. These include

- ZEUS [110] 2.6 cm thick scintillator sheets sandwiched between 3.3 mm depleted uranium plates; a resolution of $0.35/\sqrt{E}$ was obtained;

- ZEUS prototype study [111], with 10 mm lead plates and 2.5 mm scintillator sheets; $0.44/\sqrt{E}$;
- D0 [112], where the sandwich cell consists of a 4–6 mm thick depleted uranium plate, 2.3 mm LAr, a G-10 signal board, and another 2.3 mm LAr gap; $45\%/\sqrt{E}$.

Approximately Gaussian signal distributions were observed.

More recently, compensation has not been considered as important, and, in addition, the new generation of calorimeters for LHC experiments operate in a different energy regime and can tolerate poorer resolution in return for simpler, deeper structures. For example, the ATLAS endcaps consist of iron plates with scintillating fiber readout [113]. The fraction of the structure consisting of low-Z active region (scintillator in this case) is much smaller than would be necessary to achieve compensation. Test beam results with these modules show a resolution of $\approx 46\%/\sqrt{E}$, and $e/h = 1.5$–1.6.

28.10.3. ***Free electron drift velocities in liquid ionization sensors***: Velocities as a function of electric field strength are given in Refs. 114–117 and are plotted in Fig. 28.11. Recent precise measurements of the free electron drift velocity in LAr have been published by W. Walkowiak [118]. These measurements were motivated by the design of the ATLAS electromagnetic calorimeter and inconsistencies in the previous literature. Velocities are systematically higher than those shown in Fig. 28.11.

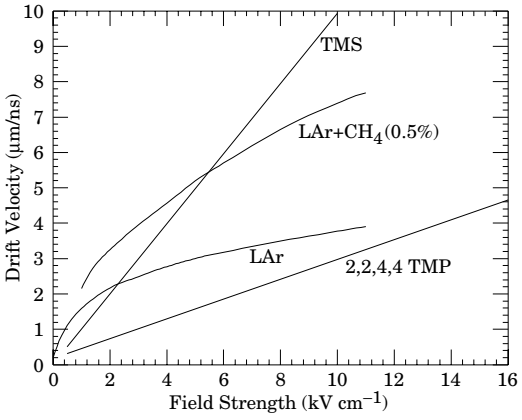

Figure 28.11: Electron drift velocity as a function of field strength for commonly used liquids.

28.11. Superconducting solenoids for collider detectors

Revised October 2001 by R.D. Kephart (FNAL).

28.11.1. ***Basic (approximate) equations***: In all cases SI units are assumed, so that B is in tesla, E is in joules, dimensions are in meters, and $\mu_0 = 4\pi \times 10^{-7}$.

Magnetic field: The magnetic field at the center of a solenoid of length L and radius R, having N total turns and a current I is

$$B(0,0) = \frac{\mu_0 NI}{\sqrt{L^2 + 4R^2}} \, . \tag{28.34}$$

Stored energy: The energy stored in the magnetic field of any magnet is calculated by integrating B^2 over all space:

$$E = \frac{1}{2\mu_0} \int B^2 dV \, . \tag{28.35}$$

For a solenoid with an iron flux return in which the magnetic field is $< 2T$, the field in the aperture is approximately uniform and equal to $\mu_0 NI/L$. If the thickness of the coil is small, (which is the case if it is superconducting), then

$$E \approx (\pi/2\mu_0) B^2 R^2 L \, . \tag{28.36}$$

Cost of a superconducting solenoid [119]:

$$\text{Cost (in M\$)} = 0.523\,[E/(1 \text{ MJ})]^{0.662} \tag{28.37}$$

Magnetostatic computer programs: It is too difficult to solve the Biot-Savart equation for a magnetic circuit which includes iron components and so iterative computer programs are used. These include POISSON, TOSCA [120], and ANSYS [121].

28.11.2. ***Scaling laws for thin solenoids***: For a detector in which the calorimetry is outside the aperture of the solenoid, the coil must be thin in terms of radiation and absorption lengths. This usually means that the coil is superconducting and that the vacuum vessel encasing it is of minimum real thickness and fabricated of a material with long radiation length. There are two major contributers to the thickness of a thin solenoid:

1. The conductor, consisting of the current-carrying superconducting material (usually Cu/Nb-Ti) and the quench protecting stabilizer (usually aluminum), is wound on the inside of a structural support cylinder (usually aluminum also). This package typically represents about 60% of the total thickness in radiation lengths. The thickness scales approximately as B^2R.
2. Approximately another 25% of the thickness of the magnet comes from the outer cylindrical shell of the vacuum vessel. Since this shell is susceptible to buckling collapse, its thickness is determined by the diameter, length, and the modulus of the material of which it is fabricated. When designing this shell to a typical standard, the real thickness is

$$t = P_c D^{2.5}[(L/D) - 0.45(t/D)^{0.5}]/2.6Y^{0.4} \, , \tag{28.38}$$

where t = shell thickness (in), D = shell diameter (in), L = shell length (in), Y = modulus of elasticity (psi), and P_c = design collapse pressure (= 30 psi). For most large-diameter detector solenoids, the thickness to within a few percent is given by [122]

$$t = P_c D^{2.5}(L/D)/2.6Y^{0.4} \, . \tag{28.39}$$

28.11.3. ***Properties of collider detector solenoids***: The physical dimensions, central field, stored energy and thickness in radiation lengths normal to the beam line of the superconducting solenoids associated with the major colliders are given in Table 28.6.

Table 28.6: Properties of superconducting collider detector solenoids.

Experiment–Lab	Field (T)	Bore Dia (m)	Length (m)	Energy (MJ)	Thickness (X_0)
CDF–Fermilab	1.5	2.86	5.07	30	0.86
DØ –Fermilab	2.0	1.06	2.73	5.6	0.87
BaBar–SLAC	1.5	2.80	3.46	27.0	< 1.4
Topaz–KEK*	1.2	2.72	5.4	19.5	0.70
Venus–KEK*	0.75	3.4	5.64	12	0.52
Cleo II–Cornell	1.5	2.9	3.8	25	2.5
Aleph–CERN*	1.5	5.0	7.0	130	1.7
ATLAS–CERN†	2.0	2.5	5.3	700	0.66
CMS–CERN†	4.0	5.9	12.5	2700	‡
Delphi–CERN*	1.2	5.2	7.4	109	4.0
H1–DESY	1.2	5.2	5.75	120	1.2
Zeus–DESY	1.8	1.72	2.85	10.5	0.9

*No longer in service.
†Detectors under construction.
‡EM calorimeter inside solenoid, so small X_0 not a goal.

The ratio of stored energy to cold mass (E/M) is a useful performance measure. One would like the cold mass to be as small as possible to minimize the thickness, but temperature rise during a quench must also be minimized. Ratios as large as 12 kJ/kg may

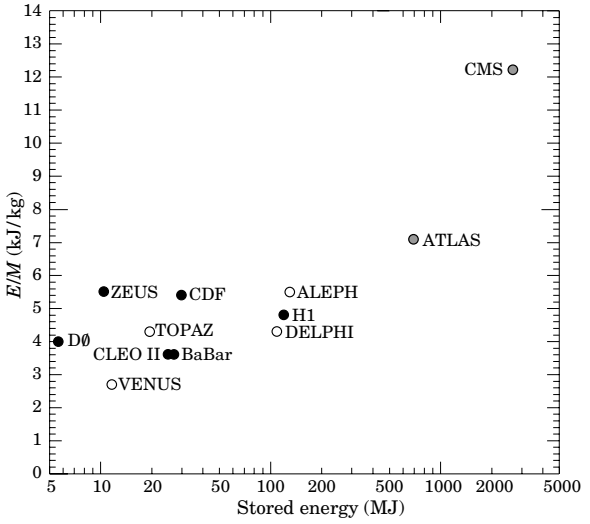

Figure 28.12: Ratio of stored energy to cold mass for existing thin detector solenoids. Solenoids in decommissioned detectors are indicated by open circles. Solenoids for detectors under construction are indicated by grey circles.

be used. The limit is set by the maximum temperature that the coil design can tolerate during a fast quench. This maximum temperature is usually limited to < 100 K so that thermal expansion effects in the coil are manageable. This quantity is shown as a function of total stored energy for some major collider detectors in Fig. 28.12.

28.12. Measurement of particle momenta in a uniform magnetic field [123,124]

The trajectory of a particle with momentum p (in GeV/c) and charge ze in a constant magnetic field $\vec{B}$ is a helix, with radius of curvature R and pitch angle λ. The radius of curvature and momentum component perpendicular to $\vec{B}$ are related by

$$p\cos\lambda = 0.3\,z\,B\,R\,, \tag{28.40}$$

where B is in tesla and R is in meters.

The distribution of measurements of the curvature $k \equiv 1/R$ is approximately Gaussian. The curvature error for a large number of uniformly spaced measurements on the trajectory of a charged particle in a uniform magnetic field can be approximated by

$$(\delta k)^2 = (\delta k_{\rm res})^2 + (\delta k_{\rm ms})^2\,, \tag{28.41}$$

where $\delta k =$ curvature error

$\delta k_{\rm res} =$ curvature error due to finite measurement resolution

$\delta k_{\rm ms} =$ curvature error due to multiple scattering.

If many (≥ 10) uniformly spaced position measurements are made along a trajectory in a uniform medium,

$$\delta k_{\rm res} = \frac{\epsilon}{L'^2}\sqrt{\frac{720}{N+4}}\,, \tag{28.42}$$

where $N =$ number of points measured along track

$L' =$ the projected length of the track onto the bending plane

$\epsilon =$ measurement error for each point, perpendicular to the trajectory.

If a vertex constraint is applied at the origin of the track, the coefficient under the radical becomes 320.

For arbitrary spacing of coordinates s_i measured along the projected trajectory and with variable measurement errors ϵ_i the curvature error $\delta k_{\rm res}$ is calculated from:

$$(\delta k_{\rm res})^2 = \frac{4}{w}\,\frac{V_{ss}}{V_{ss}V_{s^2s^2} - (V_{ss^2})^2}\,, \tag{28.43}$$

where V are covariances defined as $V_{s^m s^n} = \langle s^m s^n\rangle - \langle s^m\rangle\langle s^n\rangle$ with $\langle s^m\rangle = w^{-1}\sum(s_i{}^m/\epsilon_i{}^2)$ and $w = \sum \epsilon_i{}^{-2}$.

The contribution due to multiple Coulomb scattering is approximately

$$\delta k_{\rm ms} \approx \frac{(0.016)(\text{GeV}/c)z}{Lp\beta\cos^2\lambda}\sqrt{\frac{L}{X_0}}\,, \tag{28.44}$$

where $p =$ momentum (GeV/c)

$z =$ charge of incident particle in units of e

$L =$ the total track length

$X_0 =$ radiation length of the scattering medium (in units of length; the X_0 defined elsewhere must be multiplied by density)

$\beta =$ the kinematic variable v/c.

More accurate approximations for multiple scattering may be found in the section on Passage of Particles Through Matter (Sec. 27 of this *Review*). The contribution to the curvature error is given approximately by $\delta k_{\rm ms} \approx 8 s^{\rm rms}_{\rm plane}/L^2$, where $s^{\rm rms}_{\rm plane}$ is defined there.

References:

1. *Experimental Techniques in High Energy Physics*, T. Ferbel (ed.) (Addison-Wesley, Menlo Park, CA, 1987).
2. Claus Grupen, *Particle Detectors,* Cambridge Monographs on Particle Physics, Nuclear Physics and Cosmology, # 5, Cambridge University Press (1996).
3. K. Kleinknecht, *Detectors for Particle Radiation*, Cambridge University Press (1998).
4. G.F. Knoll, *Radiation Detection and Measurement*, 3nd edition, John Wiley & Sons, New York (1999).
5. Dan Green, *The Physics of Particle Detectors,* Cambridge Monographs on Particle Physics, Nuclear Physics and Cosmology, # 12, Cambridge University Press (2000).
6. [Icarus Collaboration], ICARUS-TM/2001-09; LGNS-EXP 13/89 add 2-01.
7. E. Albert *et al.*, Nucl. Instrum. Methods **A409**, 70 (1998).
8. B. Aubert *et al.*, [BaBar Collaboration], Nucl. Instrum. Methods **A479**, 1 (2002).
9. H. Spieler, IEEE Trans. Nucl. Sci. **NS-29**, 1142 (1982).
10. J.B. Birks, *The Theory and Practice of Scintillation Counting*(Pergamon, London, 1964).
11. D. Clark, Nucl. Instrum. Methods **117**, 295 (1974).
12. J.B. Birks, Proc. Phys. Soc. **A64**, 874 (1951).
13. B. Bengston and M. Moszynski, Nucl. Instrum. Methods **117**, 227 (1974);
    J. Bialkowski *et al.*, Nucl. Instrum. Methods **117**, 221 (1974).
14. *Proceedings of the Symposium on Detector Research and Development for the Superconducting Supercollider*, eds. T. Dombeck, V. Kelly, and G.P. Yost (World Scientific, Singapore, 1991).
15. I.B. Berlman, *Handbook of Fluorescence Spectra of Aromatic Molecules*, 2nd edition (Academic Press, New York, 1971).
16. C. Zorn, in *Instrumentation in High Energy Physics,* ed. F. Sauli, (1992, World Scientific, Singapore) pp. 218–279.
17. T. Foerster, Ann. Phys. **2**, 55 (1948).
18. J.M. Fluornoy, Conference on Radiation-Tolerant Plastic Scintillators and Detectors, K.F. Johnson and R.L. Clough editors, Rad. Phys. and Chem., **41** 389 (1993).
19. D. Horstman and U. Holm, *ibid,* 395.
20. D. Blomker *et al.*, Nucl. Instrum. Methods **A311**, 505 (1992);
    J. Mainusch *et al.*, Nucl. Instrum. Methods **A312**, 451 (1992).
21. Conference on Radiation-Tolerant Plastic Scintillators and Detectors, K.F. Johnson and R.L. Clough editors, Rad. Phys. and Chem., **41** (1993).
22. S.R. Borenstein and R.C. Strand, IEEE Trans. Nuc. Sci. **NS-31(1)**, 396 (1984).
23. P. Sonderegger, Nucl. Instrum. Methods **A257**, 523 (1987).

24. S.A. Sedykh *et al.*, Nucl. Instrum. Methods **A455**, 346 (2000).
25. SCIFI 97: Conference on Scintillating Fiber Detectors, 1997 University of Notre Dame, Indiana, eds. A. Bross, R. Ruchti, and M. Wayne.
26. K.F. Johnson, Nucl. Instrum. Methods **A344**, 432 (1994).
27. C.M. Hawkes *et al.*, Nucl. Instrum. Methods **A292**, 329 (1990).
28. A. Lempicki *et al.*, Nucl. Instrum. Methods **A333**, 304 (1993); G. Blasse, *Proceedings of the Crystal 2000 International Workshop on Heavy Scintillators for Scientific and Industrial Applications*, Chamonix, France, Sept. (1992), Edition Frontieres.
29. C. Melcher and J. Schweitzer, Nucl. Instrum. Methods **A314**, 212 (1992).
30. K. Takagi and T. Fakazawa, Appl. Phys. Lett. **42**, 43 (1983).
31. C. Kuntner *et al.*, Nucl. Instrum. Methods **A493**, 131 (2002).
32. G. Gratta, H. Newman, and R.Y. Zhu, Ann. Rev. Nucl. and Part. Sci. **44**, 453 (1994).
33. R.Y. Zhu, Nucl. Instrum. Methods **A413**, 297 (1998).
34. M. Woods *et al.*, SPIN96 (QCD161:S921:1996) 843.
35. A. Abashian *et al.*, Nucl. Instrum. Methods **A479**, 117 (2002).
36. M. Shiozawa, [Super-Kamiokande Collaboration], Nucl. Instrum. Methods **A433**, 240 (1999).
37. J. Litt and R. Meunier, Ann. Rev. Nucl. Sci. **23**, 1 (1973).
38. D. Bartlett *et al.*, Nucl. Instrum. Methods **A260**, 55 (1987).
39. B. Ratcliff, Nucl. Instrum. Methods **A502**, 211 (2003).
40. M. Cavalli-Sforza *et al.*, "Construction and Testing of the SLC Cherenkov Ring Imaging Detector," IEEE **37**, N3:1132 (1990).
41. E.G. Anassontzis *et al.*, "Recent Results from the DELPHI Barrel Ring Imaging Cherenkov Counter," IEEE **38**, N2:417 (1991).
42. See the RICH Workshop series: Nucl. Instrum. Methods **A343**, 1 (1993); Nucl. Instrum. Methods **A371**, 1 (1996); Nucl. Instrum. Methods **A433**, 1 (1999); Nucl. Instrum. Methods **A502**, 1 (2003).
43. H. Blood *et al.*, FERMILAB-PUB-76-051-EXP.
44. L. Sulak, HUEP-252 Presented at the Workshop on Proton Stability, Madison, Wisc. (1978).
45. K.S. Hirata *et al.*, Phys. Lett. **B205**, 416 (1988).
46. S. Kasuga *et al.*, Phys. Lett. **B374**, 238 (1996).
47. M.H. Ahn *et al.*, Phys. Rev. Lett. **90**, 041801 (2003).
48. R.M. Bionta *et al.*, Phys. Rev. Lett. **51**, 27 (1983); [Erratum-ibid. **51**, 522 (1983)].
49. R. Becker-Szendy *et al.*, Nucl. Instrum. Methods **A324**, 363 (1993).
50. H. Ikeda *et al.*, UTLICEPP-82-04.
51. K. Arisaka *et al.*, J. Phys. Soc. Jap. **54**, 3213 (1985).
52. K.S. Hirata *et al.*, Phys. Rev. **D38**, 448 (1988).
53. C. Athanassopoulos *et al.*, Nucl. Instrum. Methods **A388**, 149 (1997).
54. Y. Fukuda *et al.*, Nucl. Instrum. Methods **A501**, 418 (2003).
55. S.H. Ahn *et al.*, Phys. Lett. **B511**, 178 (2001).
56. J. Boger *et al.*, Nucl. Instrum. Methods **A449**, 172 (2000).
57. B. Dolgoshein Nucl. Instrum. Methods **A326**, 434 (1993).
58. X. Artru *et al.*, Phys. Rev. **D12**, 1289 (1975).
59. G.M. Garibian *et al.*, Nucl. Instrum. Methods **125**, 133 (1975).
60. G. Bassompierre *et al.*, Nucl. Instrum. Methods **411**, 63 (1998).
61. ALICE Collaboration, "Technical Design Report of the Transition Radiation Tracker," CERN/LHCC/ 2001-021 (2001).
62. RD6 Collaboration, CERN/DRDC 90-38 (1990); CERN/DRDC 91-47 (1991); CERN/DRDC 93-46 (1993).
63. T. Kirn et al., *Proceedings of TRDs for the 3rd millenium,* Workshop on advanced transition radiation detectors for accelerator and space applications, eds N. Giglietto and P. Spinelli, Frascati Physics Series, Vol. XXV, 161 (2002).
64. P. Spinelli et al., Proceedings of "TRDs for the 3rd millenium", Workshop on advanced transition radiation detectors for accelerator and space applications,"eds N. Giglietto and P. Spinelli, Frascati Physics Series, Vol. XXV, 177 (2002).
65. ATLAS Collaboration, ATLAS Inner Detector Technical Design Report, v 2, ATLAS TDR 5, CERN/LHCC/97-16 (30 April 1997).
66. ATLAS Collaboration, Detector and Physics Performance Technical Design Report, CERN/LHCC/99-14, 71 (1999).
67. B. Dolgoshein, Nucl. Instrum. Methods **252**, 137 (1986).
68. C.W. Fabjan *et al.*, Nucl. Instrum. Methods **185**, 119 (1981).
69. J. Cobb *et al.*, Nucl. Instrum. Methods **140**, 413 (1977).
70. A. Büngener *et al.*, Nucl. Instrum. Methods **214**, 261 (1983).
71. R.D. Appuhn *et al.*, Nucl. Instrum. Methods **263**, 309 (1988).
72. Y. Watase *et al.*, Nucl. Instrum. Methods **248**, 379 (1986).
73. R. Ansari *et al.*, Nucl. Instrum. Methods **263**, 51 (1988).
74. H.J. Butt *et al.*, Nucl. Instrum. Methods **252**, 483 (1986).
75. J.F. Detoeuf *et al.*, Nucl. Instrum. Methods **265**, 157 (1988).
76. M. Holder *et al.*, Nucl. Instrum. Methods **263**, 319 (1988).
77. H. Weidkamp, DiplomArbeit, Rhein-Westf. Tech. Hochschule Aachen (1984).
78. H. Grässler *et al.*, Proc. Vienna Wire Chamber Conference (1989).
79. T. Akesson *et al.*, Nucl. InstrumMethods A412, 200 (1998).
80. F.F. Rieke and W. Prepejchal, Phys. Rev. **A6**, 1507 (1972).
81. L.G. Christophorou, "Atomic and molecular radiation physics" (Wiley, London 1991).
82. G. Charpak *et al.*, Nucl. Instrum. Methods **62**, 262 (1968).
83. R. Veenhof, GARFIELD program: simulation of gaseous detectors, version 6.32, CERN Program Library Pool W999 (W5050).
84. As representative examples see: B. Adeva *et al.*, Nucl. Instrum. Methods **A287**, 35 (1990).
85. As representative example see: A. Alexander *et al.*, Nucl. Instrum. Methods **A276**, 42 (1989).
86. As representative examples see: F. Bedeschi *et al.*, Nucl. Instrum. Methods **A268**, 50 (1988); **Opal** Collaboration: Nucl. Instrum. Methods **A305**, 275 (1991).
87. A. Oed, Nucl. Instrum. Methods **A263**, 351 (1988).
88. W. Blum and G. Rolandi, *Particle Detection with Drift Chambers*, Springer-Verlag (1994).
89. A. Peisert and F. Sauli, CERN-84-08 (Jul 1984).
90. R. Bellazzini and A. M. Spezziga, Rivista del Nuovo Cimento **17**, 1 (1994).
91. D.R. Nygren and J.N. Marx, "The Time Projection Chamber," Phys. Today **31**, 46 (1978).
92. P. Weilhammer, Nucl. Instrum. Methods **A453**, 60 (2000).
93. G. Lindström *et al.*, Nucl. Instrum. Methods **A465**, 60 (2001).
94. G. Lindström *et al.*, Nucl. Instrum. Methods **A426**, 1 (1999).
95. A. Holmes-Siedle and L. Adams, *Handbook of Radiation Effects*, 2nd ed., Oxford 2002, ISBN 0-19-850733-X, QC474.H59 2001.
96. V. Radeka, IEEE Trans. Nucl. Sci. **NS-15/3**, 455 (1968); V. Radeka, IEEE Trans. Nucl. Sci. **NS-21**, 51 (1974).
97. F.S. Goulding, Nucl. Instrum. Methods **100**, 493 (1972); F.S. Goulding and D.A. Landis, IEEE Trans. Nucl. Sci. **NS-29**, 1125 (1982).
98. H. Spieler, Front-End Electronics and Signal Processing, in *Proceedings of the First ICFA School at the ICFA Instrumentation Center in Morelia*, AIP vol. 674, pp. 76 - 100, eds. L. Villaseñor, V. Villanueva, ISBN 0-7354-0141-1, LBNL-52914.
99. W.R. Nelson, H. Hirayama, and D.W.O. Rogers, "The EGS4 Code System," SLAC-265, Stanford Linear Accelerator Center (Dec. 1985).
100. R. Brun *et al.*, *GEANT3*, `CERN DD/EE/84-1` (1987).

101. D. Hitlin *et al.*, Nucl. Instrum. Methods **137**, 225 (1976). See also W. J. Willis and V. Radeka, Nucl. Instrum. Methods **120**, 221 (1974), for a more detailed discussion.
102. R. Wigmans, *Calorimetry: Energy Measurement in Particle Physics*, Clarendon, Oxford (2000).
103. ATLAS Collaboration, *The ATLAS Liquid Argon Calorimeter Technical Design Report*, CERN/LHCC 96-41 (1996).
104. CMS Collaboration, *The CMS Electromagnetic Calorimeter Technical Design Report*, CERN/LHCC 97-33 (1997).
105. C. Leroy and P.-G. Rancoita, Rep. Prog. Phys. **63**, 505 (2000).
106. D. Bintinger, in *Proceedings of the Workshop on Calorimetry for the Supercollider*, Tuscaloosa, AL, March 13–17, 1989, edited by R. Donaldson and M.G.D. Gilchriese (World Scientific, Teaneck, NJ, 1989), p. 91;
R.K. Bock, T. Hansl-Kozanecka, and T.P. Shah, Nucl. Instrum. Methods **186**, 533 (1981).
107. T.A. Gabriel, D.E. Groom, P.K. Job, N.V. Mokhov, and G.R. Stevenson, Nucl. Instrum. Methods **A338**, 336 (1994).
108. R. Wigmans, Nucl. Instrum. Methods **A259**, 389 (1987);
R. Wigmans, Nucl. Instrum. Methods **A265**, 273 (1988).
109. N. Akchurian *et al.*, Nucl. Instrum. Methods **A408**, 380 (1998).
110. U. Behrens *et al.*, Nucl. Instrum. Methods **A289**, 115 (1990);
A. Bernstein *et al.*, Nucl. Instrum. Methods **A336**, 23 (1993).
111. E. Bernardi *et al.*, Nucl. Instrum. Methods **A262**, 229 (1987).
112. S. Abachi *et al.*, Nucl. Instrum. Methods **A324**, 53 (1993).
113. F. Ariztizabal *et al.*, Nucl. Instrum. Methods **A349**, 384 (1994).
114. E. Shibamura *et al.*, Nucl. Instrum. Methods **131**, 249 (1975).
115. T.G. Ryan and G.R. Freeman, J. Chem. Phys. **68**, 5144 (1978).
116. W.F. Schmidt, "Electron Migration in Liquids and Gases," HMI B156 (1974).
117. A.O. Allen, "Drift Mobilities and Conduction Band Energies of Excess Electrons in Dielectric Liquids," NSRDS-NBS-58 (1976).
118. W. Walkowiak, Nucl. Instrum. Methods **A449**, 288 (2000).
119. M.A. Green, R.A. Byrns, and S.J. St. Lorant, "Estimating the cost of superconducting magnets and the refrigerators needed to keep them cold," in *Advances in Cryogenic Engineering*, Vol. 37, Plenum Press, New York (1992).
120. Vector Fields, Inc., 1700 N. Farnsworth Ave., Aurora, IL.
121. Swanson Analysis Systems, Inc., P.O. Box 65, Johnson Rd., Houston, PA.
122. CGA-341-1987, "Standard for insulated cargo tank specification for cryogenic liquids," Compressed Gas Association, Inc., Arlington, VA (1987).
123. R.L. Gluckstern, Nucl. Instrum. Methods **24**, 381 (1963).
124. V. Karimäki, Nucl. Instrum. Methods **A410**, 284 (1998).

29. RADIOACTIVITY AND RADIATION PROTECTION

Revised March 1998 by R.J. Donahue (LBNL) and A. Fassò (SLAC).

29.1. Definitions

The International Commission on Radiation Units and Measurements (ICRU) recommends the use of SI units. Therefore we list SI units first, followed by cgs (or other common) units in parentheses, where they differ.

• **Unit of activity** = becquerel (curie):
1 Bq = 1 disintegration s^{-1} [$= 1/(3.7 \times 10^{10})$ Ci]

• **Unit of absorbed dose** = gray (rad):
1 Gy = 1 joule kg^{-1} ($= 10^4$ erg g^{-1} = 100 rad)
$= 6.24 \times 10^{12}$ MeV kg^{-1} deposited energy

• **Unit of exposure**, the quantity of x- or γ- radiation at a point in space integrated over time, in terms of charge of either sign produced by showering electrons in a small volume of air about the point:
= 1 coul kg^{-1} of air (roentgen; 1 $R = 2.58 \times 10^{-4}$ coul kg^{-1})
= 1 esu cm^{-3}(= 87.8 erg released energy per g of air)
Implicit in the definition is the assumption that the small test volume is embedded in a sufficiently large uniformly irradiated volume that the number of secondary electrons entering the volume equals the number leaving. This unit is somewhat historical, but appears on many measuring instruments.

• **Unit of equivalent dose** (for biological damage) = sievert [= 100 rem (**r**oentgen **e**quivalent for **m**an)]: Equivalent dose in Sv = absorbed dose in grays $\times\, w_R$, where w_R (radiation weighting factor, formerly the quality factor Q) expresses long-term risk (primarily cancer and leukemia) from low-level chronic exposure. It depends upon the type of radiation and other factors, as follows [2]:

Table 29.1: Radiation weighting factors.

Radiation	w_R
X- and γ-rays, all energies	1
Electrons and muons, all energies	1
Neutrons < 10 keV	5
10–100 keV	10
> 100 keV to 2 MeV	20
2–20 MeV	10
> 20 MeV	5
Protons (other than recoils) > 2 MeV	5
Alphas, fission fragments, & heavy nuclei	20

29.2. Radiation levels [3]

• **Natural annual background**, all sources: Most world areas, whole-body equivalent dose rate ≈ (0.4–4) mSv (40–400 millirems). Can range up to 50 mSv (5 rems) in certain areas. U.S. average ≈ 3.6 mSv, including ≈ 2 mSv (≈ 200 mrem) from inhaled natural radioactivity, mostly radon and radon daughters (0.1–0.2 mSv in open areas. Average is for a typical house and varies by more than an order of magnitude. It can be more than two orders of magnitude higher in poorly ventilated mines).

• **Cosmic ray background** in counters (Earth's surface): ∼ 1 min^{-1} cm^{-2} sr^{-1}. For more accurate estimates and details, see the Cosmic Rays section (Sec. 24 of this *Review*).

• **Fluxes** (per cm^2) to deposit one Gy, assuming uniform irradiation:
≈ (**charged particles**) $6.24 \times 10^9/(dE/dx)$, where dE/dx (MeV g^{-1} cm^2), the energy loss per unit length, may be obtained from the Mean Range and Energy Loss figures.
≈ 3.5×10^9 cm^{-2} minimum-ionizing singly-charged particles in carbon.
≈ (**photons**) $6.24 \times 10^9/[Ef/\lambda]$, for photons of energy E (MeV), attenuation length λ (g cm^{-2}) (see Photon Attenuation Length figure), and fraction $f \lesssim 1$ expressing the fraction of the photon's energy deposited in a small volume of thickness $\ll \lambda$ but large enough to contain the secondary electrons.
≈ 2×10^{11} photons cm^{-2} for 1 MeV photons on carbon ($f \approx 1/2$).
(Quoted fluxes are good to about a factor of 2 for all materials.)

• **Recommended limits to exposure of radiation workers (whole-body dose):***
CERN: 15 mSv yr^{-1}
U.K.: 15 mSv yr^{-1}
U.S.: 50 mSv yr^{-1} (5 rem yr^{-1})†

• **Lethal dose**: Whole-body dose from penetrating ionizing radiation resulting in 50% mortality in 30 days (assuming no medical treatment) 2.5–3.0 Gy (250–300 rads), as measured internally on body longitudinal center line. Surface dose varies due to variable body attenuation and may be a strong function of energy.

29.3. Prompt neutrons at accelerators

29.3.1. ***Electron beams***: At electron accelerators neutrons are generated via photonuclear reactions from bremsstrahlung photons. Neutron yields from semi-infinite targets per unit electron beam power are plotted in Fig. 29.1 as a function of electron beam energy [4]. In the photon energy range 10–30 MeV neutron production results from the giant photonuclear resonance mechanism. Neutrons are produced roughly isotropically (within a factor of 2) and with a Maxwellian energy distribution described as:

$$\frac{dN}{dE_n} = \frac{E_n}{T^2} e^{-E_n/T} \ , \qquad (29.1)$$

where T is the nuclear temperature characteristic of the target nucleus, generally in the range of T = 0.5–1.0 MeV. For higher energy photons the quasi-deuteron and photopion production mechanisms become important.

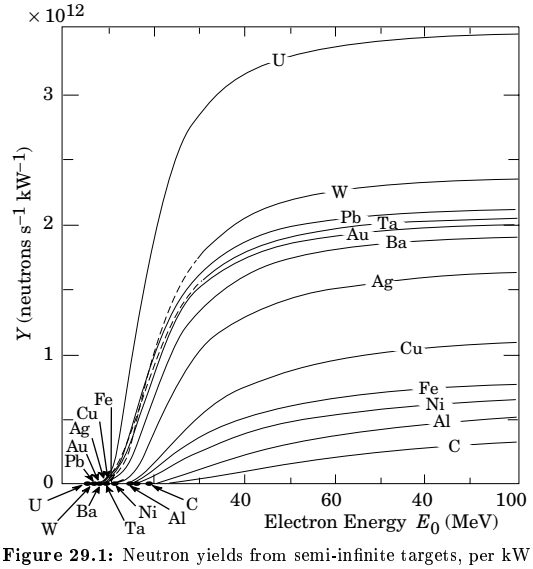

Figure 29.1: Neutron yields from semi-infinite targets, per kW of electron beam power, as a function of electron beam energy, disregarding target self-shielding.

29.3.2. ***Proton beams***: At proton accelerators neutron yields emitted per incident proton by different target materials are roughly independent [5] of proton energy between 20 MeV and 1 GeV and are given by the ratio C:Al:Cu-Fe:Sn:Ta-Pb = 0.3 : 0.6 : 1.0 : 1.5 : 1.7. Above 1 GeV neutron yield [6] is proportional to E^m, where $0.80 \leq m \leq 0.85$.

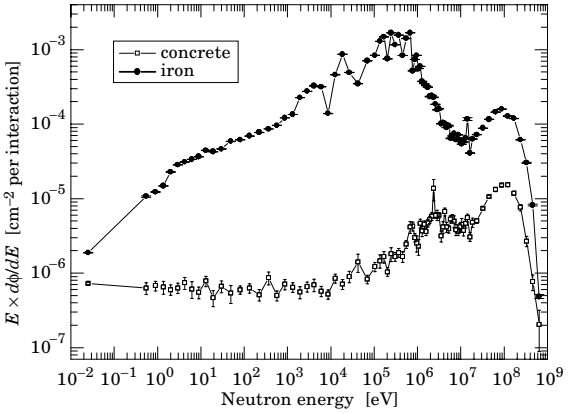

Figure 29.2: Calculated neutron spectrum from 205 GeV/c hadrons (2/3 protons and 1/3 π^+) on a thick copper target. Spectra are evaluated at 90° to beam and through 80 cm of normal density concrete or 40 cm of iron.

A typical neutron spectrum [7] outside a proton accelerator concrete shield is shown in Fig. 29.2. The shape of these spectra are generally characterized as having a thermal-energy peak which is very dependent on geometry and the presence of hydrogenic material, a low-energy evaporation peak around 2 MeV, and a high-energy spallation shoulder.

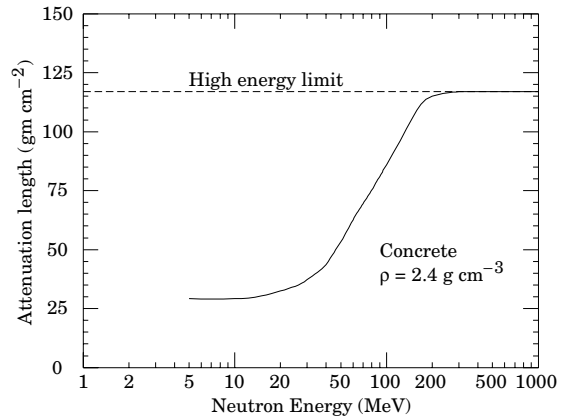

Figure 29.3: The variation of the attenuation length for monoenergetic neutrons in concrete as a function of neutron energy [5].

The neutron-attenuation length, λ, is shown in Fig. 29.3 for monoenergetic broad-beam conditions. These values give a satisfactory representation at depths greater than 1 m in concrete.

Letaw's [8] formula for the energy dependence of the inelastic proton cross-section (asymptotic values given in Table 6.1) for $E < 2$ GeV is:

$$\sigma(E) = \sigma_{\rm asympt}\left[1 - 0.62e^{-E/200}\sin(10.9E^{-0.28})\right] \ , \qquad (29.2)$$

and for $E > 2$ GeV:

$$\sigma_{\rm asympt} = 45A^{0.7}\left[1 + 0.016\sin(5.3 - 2.63\ln\ A)\right] \ , \qquad (29.3)$$

where σ is in mb, E is the proton energy in MeV and A is the mass number.

29.4. Dose conversion factors

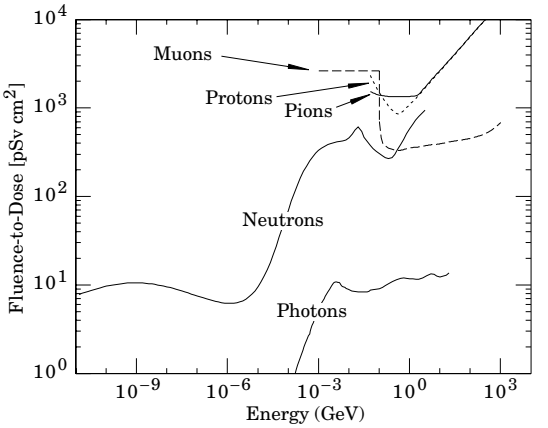

Figure 29.4: Fluence to dose equivalent conversion factors for various particles.

Fluence to dose equivalent factors are given in Fig. 29.4 for photons [9], neutrons [10], muons [11], protons and pions [12]. These factors can be used for converting particle fluence to dose for personnel protection purposes.

29.5. Accelerator-induced activity

The dose rate at 1 m due to spallation-induced activity by high energy hadrons in a 1 g medium atomic weight target can be estimated [13] from the following expression:

$$D = D_0\ \Phi\ \ln[(T+t)/t] \ , \qquad (29.4)$$

where T is the irradiation time, t is the decay time since irradiation, Φ is the flux of irradiating hadrons (hadrons cm^{-2} s^{-1}) and D_0 has a value of 5.2×10^{-17} [(Sv hr^{-1})/(hadron cm^{-2} s^{-1})]. This relation is essentially independent of hadron energy above 200 MeV.

Dose due to accelerator-produced induced activity can also be estimated with the use of "ω factors" [5]. These factors give the dose rate per unit star density (inelastic reaction for $E > 50$ MeV) after a 30-day irradiation and 1-day decay. The ω factor for steel or iron is $\simeq 3 \times 10^{-12}$ (Sv cm^3/star). This does not include possible contributions from thermal-neutron activation. Induced activity in concrete can vary widely depending on concrete composition, particularly with the concentration of trace quantities such as sodium. Additional information can be found in Barbier [14].

29.6. Photon sources

The dose rate from a gamma point source of C Curies emitting one photon of energy $0.07 < E < 4$ MeV per disintegration at a distance of 30 cm is 6CE (rem/hr), or 60CE (mSv/hr), ±20%.

The dose rate from a semi-infinite uniform photon source of specific activity C (μCi/g) and gamma energy E (MeV) is $1.07CE$ (rem/hr), or $10.7CE$ (mSv/hr).

Footnotes:

* The ICRP recomendation [2] is 20 mSv yr^{-1} averaged over 5 years, with the dose in any one year $\leq$ 50 mSv.

† Many laboratories in the U.S. and elsewhere set lower limits.

‡ *Dose* is the time integral of *dose rate*, and *fluence* is the time integral of *flux*.

References:

1. C. Birattari *et al.*, "Measurements and simulations in high energy neutron fields" Proceedings of the Second Shielding Aspects of Accelerators, Targets and Irradiation Facilities, in press (1995).
2. ICRP Publication 60, *1990 Recommendation of the International Commission on Radiological Protection* Pergamon Press (1991).
3. See E. Pochin, *Nuclear Radiation: Risks and Benefits* (Clarendon Press, Oxford, 1983).
4. W.P. Swanson, *Radiological Safety Aspects of the operation of Electron Linear Accelerators,* IAEA Technical Reports Series No. 188 (1979).
5. R.H. Thomas and G.R. Stevenson, *Radiological Safety Aspects of the Operation of Proton Accelerators,* IAEA Technical Report Series No. 283 (1988).
6. T.A. Gabriel *et al.*, "Energy Dependence of Hadronic Activity," Nucl. Instrum. Methods **A338**, 336 (1994).
7. A.V. Sannikov, "BON94 Code for Neutron Spectra Unfolding from Bonner Spectrometer Data," CERN/TIS-RP/IR/94-16 (1994).
8. Letaw, Silberberg, and Tsao, "Proton-nucleus Total Inelastic Cross Sections: An Empirical Formula for E > 10 MeV," *Astrophysical Journal Supplement Series,* **51**, 271 (1983);

   For improvements to this formula see Shen Qing-bang, "Systematics of intermediate energy proton nonelastic and neutron total cross section," International Nuclear Data Committee INDC(CPR)-020 (July 1991).
9. A. Ferrari and M. Pelliccioni, "On the Conversion Coefficients from Fluence to Ambient Dose Equivalent," Rad. Pro. Dosimetry 51, 251 (1994).
10. A.V. Sannikov and E.N. Savitskaya, "Ambient Dose and Ambient Dose Equivalent Conversion Factors for High-Energy neutrons," CERN/TIS-RP/93-14 (1993).
11. "Data for Use in Protection Against External Radiation," ICRP Publication 51 (1987).
12. G.R. Stevenson, "Dose Equivalent Per Star in Hadron Cascade Calculations," CERN TIS-RP/173 (1986).
13. A.H. Sullivan *A Guide To Radiation and Radioactivity Levels Near High Energy Particle Accelerators,* Nuclear Technology Publishing, Ashford, Kent, England (1992).
14. M. Barbier, *Induced Activity,* North-Holland, Amsterdam (1969).

30. COMMONLY USED RADIOACTIVE SOURCES

Table 30.1. Revised November 1993 by E. Browne (LBNL).

			Particle		Photon	
		Type of	Energy	Emission	Energy	Emission
Nuclide	Half-life	decay	(MeV)	prob.	(MeV)	prob.
$^{22}_{11}$Na	2.603 y	β^+, EC	0.545	90%	0.511	Annih.
					1.275	100%
$^{54}_{25}$Mn	0.855 y	EC			0.835	100%
					Cr K x rays 26%	
$^{55}_{26}$Fe	2.73 y	EC			Mn K x rays:	
					0.00590	24.4%
					0.00649	2.86%
$^{57}_{27}$Co	0.744 y	EC			0.014	9%
					0.122	86%
					0.136	11%
					Fe K x rays 58%	
$^{60}_{27}$Co	5.271 y	β^-	0.316	100%	1.173	100%
					1.333	100%
$^{68}_{32}$Ge	0.742 y	EC			Ga K x rays 44%	
$\rightarrow$ $^{68}_{31}$Ga		β^+, EC	1.899	90%	0.511	Annih.
					1.077	3%
$^{90}_{38}$Sr	28.5 y	β^-	0.546	100%		
$\rightarrow$ $^{90}_{39}$Y		β^-	2.283	100%		
$^{106}_{44}$Ru	1.020 y	β^-	0.039	100%		
$\rightarrow$ $^{106}_{45}$Rh		β^-	3.541	79%	0.512	21%
					0.622	10%
$^{109}_{48}$Cd	1.267 y	EC	0.063 e^-	41%	0.088	3.6%
			0.084 e^-	45%	Ag K x rays 100%	
			0.087 e^-	9%		
$^{113}_{50}$Sn	0.315 y	EC	0.364 e^-	29%	0.392	65%
			0.388 e^-	6%	In K x rays 97%	
$^{137}_{55}$Cs	30.2 y	β^-	0.514 e^-	94%	0.662	85%
			1.176 e^-	6%		
$^{133}_{56}$Ba	10.54 y	EC	0.045 e^-	50%	0.081	34%
			0.075 e^-	6%	0.356	62%
					Cs K x rays 121%	
$^{207}_{83}$Bi	31.8 y	EC	0.481 e^-	2%	0.569	98%
			0.975 e^-	7%	1.063	75%
			1.047 e^-	2%	1.770	7%
					Pb K x rays 78%	
$^{228}_{90}$Th	1.912 y	6α:	5.341 to 8.785		0.239	44%
		3β^-:	0.334 to 2.246		0.583	31%
					2.614	36%
($\rightarrow$ $^{224}_{88}$Ra	$\rightarrow$ $^{220}_{86}$Rn	$\rightarrow$ $^{216}_{84}$Po	$\rightarrow$ $^{212}_{82}$Pb	$\rightarrow$ $^{212}_{83}$Bi	$\rightarrow$ $^{212}_{84}$Po)	
$^{241}_{95}$Am	432.7 y	α	5.443	13%	0.060	36%
			5.486	85%	Np L x rays 38%	
$^{241}_{95}$Am/Be	432.2 y	6×10^{-5} neutrons (4–8 MeV) and				
		$4 \times 10^{-5}\gamma$'s (4.43 MeV) per Am decay				
$^{244}_{96}$Cm	18.11 y	α	5.763	24%	Pu L x rays $\sim$ 9%	
			5.805	76%		
$^{252}_{98}$Cf	2.645 y	α (97%)	6.076	15%		
			6.118	82%		
		Fission (3.1%)				
		$\approx$ 20 γ's/fission; 80% $<$ 1 MeV				
		$\approx$ 4 neutrons/fission; $\langle E_n \rangle$ = 2.14 MeV				

"Emission probability" is the probability per decay of a given emission; because of cascades these may total more than 100%. Only principal emissions are listed. EC means electron capture, and e^- means monoenergetic internal conversion (Auger) electron. The intensity of 0.511 MeV e^+e^- annihilation photons depends upon the number of stopped positrons. Endpoint $\beta^\pm$ energies are listed. In some cases when energies are closely spaced, the γ-ray values are approximate weighted averages. Radiation from short-lived daughter isotopes is included where relevant.

Half-lives, energies, and intensities are from E. Browne and R.B. Firestone, *Table of Radioactive Isotopes* (John Wiley & Sons, New York, 1986), recent *Nuclear Data Sheets*, and *X-ray and Gamma-ray Standards for Detector Calibration*, IAEA-TECDOC-619 (1991).

Neutron data are from *Neutron Sources for Basic Physics and Applications* (Pergamon Press, 1983).